MOLECULAR IMAGING OF $\alpha_v\beta_6$–POSITIVE TUMORS AND PANCREATIC β-CELL MASS BY RADIOLABELED PEPTIDES

APPROVED BY SUPERVISORY COMMITTEE

Xiankai Sun, Ph.D. (Mentor)

A. Dean Sherry (Co-Mentor)

Orhan K. Öz, MD., Ph.D.

Jung-Mo Ahn, Ph.D.

Pietro P. Antich, Ph.D. (Chairman)

MOLECULAR IMAGING OF $\alpha_v\beta_6$–POSITIVE TUMORS AND PANCREATIC β-CELL MASS BY RADIOLABELED PEPTIDES

by

MAI LIN

DISSERTATION

Presented to the Faculty of the Graduate School of Biomedical Sciences

The University of Texas Southwestern Medical Center at Dallas

In Partial Fulfillment of the Requirements

For the Degree of

DOCTOR OF PHILOSOPHY

The University of Texas Southwestern Medical Center at Dallas

Dallas, Texas

December, 2010

To my mother Yu-Jen Liao.

ACKNOWLEDGEMENT

This is a great journey, and I would like to thank all people who have supported and helped me. First, I want to thank my advisor Dr. Xiankai Sun. I have always been proud of my experimental skills, which I thought were everything for science and research. I am very fortunate that Xiankai always guides me with his sincere suggestions and advice. To date, I have realized the importance of other scientific fields to molecular imaging and have learned how to initiate and implement innovative research. I also want to thank my co-advisor Dr. Dean Sherry. His insightful advice and kind help will be beneficial to my whole life.

I want to thank my lab mates for their generosity, time, and efforts. I deeply appreciate Dr. Guyiang Hao for his helpful suggestions. I thank Michael Long for his help in microPET/CT imaging reconstruction and data analysis. I am grateful to Su-Tang Lo, who provided me great help in the development of the streptozotocin (STZ)-induced diabetic mouse model. I am thankful to former and current colleagues, including Yi Guo, Ming Xiao, Cynthia Rostollan, Anjali Gupta, Sonia Hill, Dr. You-Fu Zhou, Dr. Wei Liu, Dr. Lifen Xu, Dr. Guoquiang Shangguan, and Dr. Ajay Singh. They have made the lab a great place to work and always kindly helped me.

My research was greatly benefited from collaborations with other laboratories. I am indebted to Eunice Murage and Dr. Shunzi Li for providing peptides as well as sharing scientific data. I thank Dr. Angelo Lubag for showing me the techniques to isolate rat islets and anatomical location of the pancreas in mice and rats. I want to thank Dr. Kathlynn Brown and Dr. Michael McGuire for their great support in the lung cancer

imaging project (Chapter 3), and to Dr. Jung-Mo Ahn for his advice and help in the β-cell imaging project (Chapter 4).

I am also very thankful to Drs. Pietro Antich and Orhan Öz for being my committee members. They have provided me with critical insights and invaluable advice for career preparation. In addition, I want to thank Drs. Jer-Tsong Hsieh and Padmakar Kulkarni for their scientific and personal advice. I also like to thank Ms. Kay Emerson, Ms. Jocelyn Chafouleas, and Ms. Emily Mayer for their consistent and prompt help throughout my time at UT Southwestern. I also thank my classmates, Gang Ren, Lan Jiang, Peiying Wang, Ouyang Lou, Feng Xu and Long Huang for their help.

Finally, none of this work would have been possible without the support from my family and my M.S. advisor Dr. Hsin-Ell Wang. My mother Yu-Jen Liao is always the greatest supporter of my life. Her endless love makes me strong to face and overcome any difficulties. I can never express my appreciation enough to Dr. Hsin-Ell Wang for the value of team work and great help. He not only opened my scientific career, but also taught me the value of family and love, which are far more important than my personal success.

MOLECULAR IMAGING OF $\alpha_v\beta_6$–POSITIVE TUMORS AND PANCREATIC β-CELL MASS BY RADIOLABELED PEPTIDES

MAI LIN, Ph.D.

The University of Texas Southwestern Medical Center at Dallas, 2010

Mentor: XIANKAI SUN, Ph.D.

Co-Mentor: A. DEAN SHERRY, Ph.D.

Conventional diagnostic methodologies of lung cancer and diabetes are limited by sensitivity and specificity. In consequence, patients usually get diagnosed when the symptoms appear and the diseases are at the advanced stages. As the expressions of the $\alpha_v\beta_6$ integrin and glucagon-like peptide-1 receptor (GLP-1R) are highly related to aggressive tumor phenotypes and functional pancreatic β-cells, this work has been set to develop peptide-based radiotracers that can specifically bind to $\alpha_v\beta_6$ or GLP-1R for noninvasively monitoring the progression of lung cancer and diabetes.

By phage display, a peptide sequence that specific binds to $\alpha_v\beta_6$ was identified. In the evaluation of its truncated forms with similar binding affinity, a polyethylene glycol chain (PEG11) was inserted to the C-terminus and a bifunctional chelator (DOTA) was conjugated to either end of the peptides. The conjugates were labeled with ^{111}In ($t_{1/2}$: 2.8

d) under mild conditions with the highest achievable specific activity of 1.15×10^4 MBq/μmol. The *in vivo* evaluation was performed in a lung adenocarcinoma xenograft mouse model. Of the six conjugates, 10PD showed the best tissue contrast of the H2009 ($\alpha_v\beta_6^+$) tumor. However, it also yielded to have the highest renal accumulation. The high kidney uptake of 10PD was found to be alleviated by conjugating DOTA at the N-terminus or reducing the peptide net charges.

To evaluate GLP-1-based radiotracers for imaging pancreatic β-cell mass (BCM), GLP-1, [D-Ala^8]GLP-1, two bicyclic GLP-1 analogs (EM2196 and EM2198), and exendin-4 were synthesized and compared for their biological properties. All peptide constructs were tagged with an 6-aminohexanoic linker (Ahx) followed by DOTA conjugation at C-terminus and labeled with ^{64}Cu ($t_{1/2}$: 12.7 h). The specific activity of the labeled peptide conjugates was up to 1.0×10^6 MBq/μmol with radiochemical purity over 97%. Compared to GLP-1, [D-Ala^8]GLP-1 revealed strong resistance against DPP-IV. In addition, EM2198 demonstrated high stability against NEP 24.11 presumably by the shielding effects from the two lactam bridges. All peptide conjugates were highly selective to the GLP-1R with the IC_{50} values in 0.1-0.4 nM. However, only ^{64}Cu-EM2198 showed clear pancreas area on the microPET/CT studies. The signal of ^{64}Cu-EM2198 from the pancreas was confirmed by the *ex vivo* imaging scans. The potential of ^{64}Cu-EM2198 for imaging BCM was further supported by co-injecting a blocking dose of unlabeled exendin-4 and performing imaging studies in the STZ-treated diabetic mice.

TABLE OF CONTENTS

PRIOR PUBLICATIONS

Peer-reviewed Articles

Hsin-Ell Wang, Hung-Man Yu, Ren-Shyan Liu, **Mai Lin**, Juri G. Gelovani, Jeng-Jong Hwang, Hon-Jian Wei and Win-Ping Deng. Molecular Imaging with ^{123}I-FIAU, ^{18}F-FUdR, ^{18}F-FET, and ^{18}F-FDG for Monitoring Herpes Simplex Virus Type 1 Thymidine Kinase and Ganciclovir Prodrug Activation Gene Therapy of Cancer. *J. Nucl. Med.* 47 (7): 1161-1171, **2006**.

Hyun-Soon Chong, Santosh Mhaske, **Mai Lin**, Sankar Bhuniya, Hyun A. Song, Martin W. Brechbiel and Xiankai Sun. Novel synthetic ligands for targeted PET imaging and radiotherapy of copper. *Bioorg Med Chem Lett*. 17(22):6107-10, **2007**.

Mai Lin, Angelo Lubag, Michael J. McGuire, Serguei Y. Seliounine, Edward N. Tsyganov, Peter P. Antich, A. Dean Sherry, Kathlynn C. Brown, Xiankai Sun. Advances in molecular imaging of pancreatic beta cells. *Front Biosci*. 13, 4558-4575, **2008**.

Wei Liu, Asghar Hajibeigi, **Mai Lin**, Cynthia L. Rostollan, Zoltan Kovacs, Orhan K. Öz and Xiankai Sun. An osteoclast-targeting agent for imaging and therapy of bone metastasis. *Bioorg Med Chem Lett*. 18(17): 4789-4793, **2008**.

Mark Woods, Peter Caravan, Carlos F. G. C. Geraldes, Matthew T. Greenfield, Garry E. Kiefer, PhD, **Mai Lin**, Kenneth McMillan, M. Isabel M. Prata, Ana C. Santos, Xiankai Sun, Jufeng Wang, Shanrong Zhang, Piyu Zhao, and A. Dean Sherry. The Effect of the Amide Substituent on the Biodistribution and Tolerance of Lanthanide(III) DOTA-Tetraamide Derivatives. *Investigative Radiology*, 43 (12): 861-870, **2008**.

Azhar Pasha, **Mai Lin**, Gyula Tircso, Cynthia L. Rostollan, Mark Woods, Garry E. Kiefer, A. Dean Sherry, and Xiankai Sun. Synthesis and biological evaluation of lanthanide ion DOTA-tetraamide complexes bearing peripheral hydroxyl groups. *J. Biol. Inorg. Chem*,14: 421-438, **2009**.

Shunzi Li, Michael McGuire, **Mai Lin**, Ying-Horng Liu, Tsukasa Oyama, Xiankai Sun, and Kathlynn brown. Synthesis and characterization of a high-affinity $\alpha_v\beta_6$-specific ligand for *in vitro* and *in vivo* applications. *Mol Cancer Ther*, 8(5): 1239-1249, **2009**

Liu J, Hajibeigi A, Ren G, **Lin M**, Siyambalapitiyage W, Liu Z, Simpson E, Parkey RW, Sun X, and Öz OK. Retention of the radiotracers ^{64}Cu -ATSM and ^{64}Cu-PTSM in human and murine tumors is influenced by MDR1 protein expression. *J. Nucl. Med.* 50 (8): 1332-1339, **2009**

Mai Lin, Shunzi Li, Michael J. McGuire, Kathlynn C. Brown, and Xiankai Sun. Effects of PEGylation and DOTA conjugation sites on $\alpha_v\beta_6$ targeting peptide conjugates. (in preparation)

Mai Lin, Eunice Murage, Su-Tang Lo, Michael J. McGuire, Michael Long, Kathlynn C. Brown, Jung-Mo Ahn, and Xiankai Sun. A novel bicyclic peptide-based radiotracer targeting to GLP-1 receptors as the promising probe to image pancreatic β-cell mass. (in preparation)

Conference Abstracts

H.Y. Yu, **M. Lin**, W.P. Deng, C.W. Chang, R.S. Liu, G. Ting, and H.E. Wang. Evaluation of [^{18}F]FUdR as a Potential Imaging Probe in HSV-1-tk Suicide Gene Therapeutic Model. *51st Annual Society of Nuclear Medicine Meeting in Philadelphia,* PA, June 2004.

M. Lin, Z. Zhang, V.D. Kodibagkar, N. Slavine, E. Tsyganov, S. Seliounine, A. Harper, J. Stanfield, C. Chaney, O.K. Oz, R.P. Mason, P. Antich, J.T. Hsieh, and X. Sun. Multimodality Imaging Studies of Bone Metastasis in an Intraosseous CaP Xenograft Mouse Model. *Molecular Medicine Meeting in Houston*, TX, Feb 2005.

M. Lin, Z. Kovacs, A. Adams, and X. Sun. Evaluation of ^{177}Lu-DO3P as a Potential Bone Imaging Agent. *52nd Annual Society of Nuclear Medicine Meeting in Toronto*, Canada, June 2005.

Mai Lin, Michael McGuire, Serguei Seliounine, Edward Tsyganov, A. Dean Sherry, Kathlynn Brown and Xiankai Sun. Evaluation of Peptide-Mediating Targeting Phage as a Potential β-Cell Imaging Agent. *J. NUCL. Med.* MEETING ABSTRACTS, May 2006; 47: 519P.

Mai Lin, Azhar Pasha, Mark Woods, A. Dean Sherry, Garry E. Kiefer, Xiankai Sun. In Vivo Evaluation of Three ^{177}Lu-Labeled Novel Tetraazacyclododecane-Based Ligands Differing in the Numbers of Peripheral Hydroxymethyl Groups. *17th International Symposium on Radiopharmaceutical Chemistry,* German, May 2007.

Wei Liu, Asghar Hajibeigi, Chandima Siyambalapitiyage, **Mai Lin**, Cynthia Rostollan, Orhan Oz, Zoltan Kovacs, and Xiankai Sun. Novel osteoclast-targeting agents for bone metastases. *J. NUCL. Med.* MEETING ABSTRACTS, May 2008; 49: 297P.

Mai Lin, Shunzi Li, Michael McGuire, Kathlynhn C. Brown, Xiankai Sun. Effects of PEGylation and DOTA Conjugation Sites on $\alpha_v\beta_6$ Targeting Peptide Conjugates.*J. Nucl Med.* MEETING ABSTRACTS, May 2008; 49: 96P.

Su-Tang Lo, **Mai Lin**, Michael Long, Eunice Murage, A. Dean Sherry, Jung-Mo Ahn[2], and Xiankai Sun. Targeting GLP-1R for PET Imaging of Pancreatic β Cell Mass using ^{68}Ga-labeled GLP-1 Peptide Analogs. *World Molecular Imaging Congress,* Canada, Sep 2009.

LIST OF FIGURES

LIST OF SCHEMES

LIST OF TABLES

CHAPTER ONE

Overview

1.1 Molecular Imaging

Molecular imaging was first introduced literally in 2001 as a multidisciplinary field that combines imaging research, molecular biology, chemistry, and medical physics.[1, 2] Although molecular imaging is often described as revolutionary, its concept actually began with the first use of ^{131}I to image recurrent thyroid carcinoma.[3] In general, molecular imaging can broadly be defined as the visual representation, characterization, and quantification in biological processes at the cellular or molecular level of living organisms with negligible perturbation.[1, 2]

The emergence of molecular imaging largely resulted from the recent advances in biotechnologies and small animal imaging instrumentation. As the first map of human genome was completed in 2000,[4] unprecedented opportunities have been offered for scientists to study human disease at molecular level. Given the fact that different individuals have their unique gene/protein expression profiles of particular tissues as revealed by genomics/proteomics, molecular imaging creates the possibility to link these *in vitro* assays to imaging studies on living subjects. In fact, one of the ultimate goals of molecular imaging is to develop individualized approaches for disease diagnosis and treatment.[5]

Compared to traditional imaging techniques, molecular imaging reveals the target of interest in particular disease. Because molecular imaging is focused on identifying the underlying molecular events in disease initiation and progression, it can potentiate the

early detection of diseases. In addition, as the expression of specific biomarkers correlates with the aggressiveness of disease, molecular imaging may also be able to distinguish disease states. Take solid tumors as an example, the evaluation of their clinical treatments is majorly based on anatomic changes of the tumors.[6] However, changes in tumor size after therapy are not always an indication of a better clinical outcome.[7] In this regard, the development of molecular imaging can be aimed to measure tumor function and its molecular expression patterns.[8, 9]

Due to its noninvasive and quantitative features, molecular imaging has also been applied to assess drug discovery. In 1992, a new regulatory process known as "Accelerated approval" was approved by Food and Drug Administration (FDA).[10] In addition to traditional endpoints, this new regulation allows alternative endpoints to be assessed on the basis of biomarkers that are measurable as indicators of clinical and therapeutic efficiency, where molecular imaging can play an important role by providing the information on the presence, efficacy, tissue distribution profile, and pharmacokinetics of drug candidates.[11-14] Particular role of imaging technologies in drug discovery and development has been illustrated by Hsp90 inhibitor 17-AAG and the hypoxia probe SR-4554,[15] where molecular imaging was used to monitor their therapeutic efficacy.

In addition to its known applications in health care and drug discovery, molecular imaging is also important for basic biomedical research.[16, 17] To date, molecular imaging has been used to elucidate several enzymatic and cellular events in inflammation, angiogenesis, apoptosis, cell trafficking, and thrombosis.[18-21] Its role in the development

of animal model is another example, where functional analysis of the resultant phenotype is the most challenging part of the whole process.[16] In contrast to most traditional characterization methods of animal models, molecular imaging offers distinct advantages by eliminating the need of killing. Furthermore, molecular imaging is capable of providing quantitative measures of a biological event in the context of the nonpertubated living conditions, which is highly desirable and complementary to the *in vitro* and *ex vivo* assays in biomedical research.

1.2 Molecular Imaging Techniques (Table 1.1)

To some extent, molecular imaging is considered as an extension of nuclear medicine,[22, 23] in which radioactive compounds are used in the diagnosis and treatment of disease. To date, imaging modalities including ultrasound (US), magnetic resonance imaging (MRI), computed tomography (CT), PET, single photon emission computed tomography (SPECT), bioluminescence imaging (BLI), and fluorescence imaging (FI) have been commonly used in molecular imaging (Table 1.1).

Table 1.1. Overview of current imaging modalities [24]

Technique	Resolution	Depth	Quantitative	Clinical use
US	50 µm	cm	Yes	Yes
MRI	10-100 µm	No limit	Yes	Yes
CT	50 µm	No limit	Yes	Yes
PET	1-2 mm	No limit	Yes	Yes
SPECT	1-2 mm	No limit	Yes	Yes
BLI	Several mm	cm	No	No
FI	2-3 mm	< 1 cm	No	No

The resolution of each imaging modality is from common pre-clinical systems.

US Imaging

Medical US relies on the detection of emitted sound waves. The imaging technique involves exposing part of the living subjects to high-frequency sound waves to produce pictures. Because different tissue has different acoustic characteristics, sound waves are altered during traveling. Most clinical US is performed at frequencies of 2-15 MHz.[25] High-frequency US imaging (US biomicroscopy) that is operated in the 40-60 MHz range has been applied to study mouse embryonic development, tumor biology, and eye diseases.[26-28] The low cost, non-ionizing nature, and real time imaging are advantages for US. However, the role of US in the evaluation of lung, stomach, intestines, and bones is limited. Coupling US with microbobbles as a contrast agent may enable the quantification of blood flow in vasculature and targeted molecular imaging.[29]

MRI

The tissue characterization of MRI relies on the detection of water protons through the application of radiofrequency pulses to the sample in a magnetic field. Because the microenvironment of those protons is different in tissues, the appearance as well as the longitudinal (T1) and transverse (T2) relaxation times of the tissue are detected. Nuclei other than protons such as ^{23}Na and ^{31}P can also be studies by MRI. In addition, contrast agents, such as gadolinium chelates (e.g. Gd-DTPA) and superparamagnetic iron oxide nanoparticles (SPIO) may also be used to enhance signal differences around the target tissue.[30, 31]

Standard clinical MR imagers (1.5-T magnetic field strength) provide images with about 1-mm resolution. When special coils and/or probes are employed, the resolution of MRI can be improved to 10 μm.[24] As MRI has superior resolution and can obtain

functional and anatomical information at the same time, it has been widely used in molecular imaging.[32] However, the sensitivity of MRI is inherently low compared to nuclear medicine and optical imaging modalities. In order to overcome this problem, varieties of techniques such as high magnetic fields (4.7-14T), customized hardware and software, and prolonged acquisition times have been developed.[32, 33]

Variations based on standard MRI techniques that include diffusion MRI, perfusion MRI, and magnetic resonance spectroscopy (MRS), have been developed to acquire greater functional information. Diffusion and perfusion MRI are very useful for the detection of stroke, tumor characterization, and evaluation of neurodegenerative diseases.[34, 35] On the other hand, MRS is an analytical technique to study metabolic changes noninvasively. Hydrogen, phosphorus, and sodium are the nucleus frequently applied to MRS. The study of MRS has been focused on strokes, cancers, Alzheimer's disease, and other diseases affecting the brain.[33, 36, 37]

CT

CT is a medical imaging method employing tomography created by computer processing. Digital geometry processing is used to generate a three-dimensional image of an object from a large series of two-dimensional X-ray images taken around a single axis of rotation.[38] Because CT provides detailed, cross-sectional views of most types of tissue, CT has become an important tool in medical imaging since 1970s.[39] Over the past decades, microCT imaging has been rapidly advanced.[39] With its imaging resolution at the range of 50-100 μm, microCT is applied for screening transgenic animal phenotypes and monitoring therapeutic effects of new compounds.[40]

The major drawback of CT for molecular imaging is its low tissue contrast and sensitivity by using iodinated agents.[41] As such, new CT contrast agents based on gold nanoparticle are under development.[42] Currently, one important application of CT is to combine with other imaging modalities, especially nuclear imaging modalities. With the use of co-registration algorithms, it is possible to obtain precise anatomical localization of physiological/functional data.

Nuclear Imaging Modalities

PET

Table 1.2. Decay properties of common PET radioisotopes

Radionuclide	Half-Life ($t_{1/2}$)	$E_{\beta+max}$	Decay Mode (β^+ %)
C-11	20.4 min	0.94 MeV	99
N-13	9.96 min	1.20 MeV	100
O-15	2.04 min	1.74 MeV	100
F-18	109 min	0.64 MeV	97
Cu-64	12.7 h	0.65 MeV	17.4
Ga-68	68 min	1.90 MeV	89
Y-86	14.7 h	1.20 MeV	33
Zr-89	3.27 d	1.81 MeV	100
I-124	4.2 d	2.14 MeV	23

PET works by detecting 511 Kev gamma rays that are produced by the annihilation of positrons emitted by a radiotracer and nearby electrons. To perform a PET imaging study, a radiotracer with positron-emitter is required to be injected into a living subject. As the radioisotope undergoes positron decay, the emitted positron travels in tissues. When the positron loses its kinetic energy, it interacts with an electron and produces a pair of annihilated photons moving in approximately opposite directions. The technique depends on simultaneous or coincident detection of these photons.

PET is highly sensitive (10^{-11}-10^{-12} mole/L) without the limitation in tissue penetration as seen in optical imaging modalities.[43] To date, PET systems have the ability to obtain absolute imaging quantification (e.g. Bq/mL) after corrections for photon attenuation and scattering. In addition, because of the unique feature to image ^{11}C, ^{13}N, or ^{15}O labeled compounds, the role of PET has been well-established in the field of molecular imaging. Most clinical PET scanner has a spatial resolution of 6-8 mm, and the resolution for small animal scanners is approaching 1 mm.[43] As such, PET needs the aid of anatomical CT or MRI to localize its functional information. Conventional radioisotopes for PET chemistry are shown in Table 1.2.

SPECT

Table 1.3. Decay properties of common SPECT radioisotopes

Radionuclide	Half-Life ($t_{1/2}$)	E_γ	Decay Mode
Ga-67	78.1 h	93, 184, and 300 KeV	EC (100%)
Tc-99m	6.0 h	140 KeV	IT (100%)
In-111	67.9 h	172 and 242 KeV	EC (100%)
I-123	13.3 h	27 and 159 KeV	EC (87%), γ (85%)
I-131	8.0 d	364 and 723 KeV	β^- (89%), γ (81%)
Sm-153	1.9 d	103 KeV	β^- (100%), γ (28%)
Lu-177	6.7 d	113 and 208 KeV	β^- (100%), γ (27%)
Ir-192	74.2 d	317, 468, and 604 KeV	β^- (95%), γ (5%)
Tl-201	3.0 d	71, 135, 167 KeV	EC (100%)

SPECT is another nuclear imaging modality detecting gamma rays. However, in contrast with PET, the radiotracer used in SPECT emits gamma rays and collimators are required to define incident angles for imaging reconstruction.[44] To acquire SPECT images, the gamma camera is rotated around the subject. Projections are acquired at defined points during the rotation, typically every 3-6 degrees. In most cases, a full 360 degree rotation is used to obtain an optimal reconstruction.[44] To date, multi-headed

gamma cameras have been applied to provide accelerated imaging acquisition. Unlike PET, SPECT has the capability of performing multi-isotope imaging with different energy windows, which allows multiple biological events to be monitored at the same time.[45, 46] Conventional radioisotopes for SPECT chemistry are shown in Table 1.3.

PET vs. SPECT

One may think that the radioisotope tagged on a radiotracer is the determinant of choosing either PET or SPECT for the imaging studies. However, the capabilities of PET and SPECT in terms of sensitivity, spatial resolution, and imaging quantification are quite different. These physical considerations are discussed as follows.

a. Sensitivity

High sensitivity obtained from high photon detection efficiency is important for the development of nuclear imaging modalities. Sensitivity of PET and SPECT is strongly dependent on the material and the thickness of the scintillation crystal, as well as on the material and geometry of mechanical collimation. As collimators are needed for SPECT to reject photons that are not within a defined angular range, this characteristic exhibits low geometric efficiencies and limits the sensitivity of SPECT.[47] On the contrary, PET detects the coincidences of positron-electron annihilation, which requires no collimators. As such, PET has higher sensitivity than SPECT by approximately 2-3 orders of magnitude.[47]

b. Spatial Resolution

The spatial resolutions of PET and SPECT are determined by different factors. While the improvement in SPECT resolution is largely realized by collimator design, the

spatial resolution of PET is affected by the positron range and photon non-collinearity.[47] Positron range is defined by the distance traveled by the emitted positrons in a surrounding medium before annihilation. Because different positron-emitting radioisotopes have different positron energies, the spatial resolution of PET varies with the radioisotope used. In addition, the spatial resolution of PET can be affected by the non-collinearity of the two emitted photons resulted from the non-zero net momentum of positron annihilation. The resolution blurring caused by photon non-collinearity is largely due to the physical limit of the detector element size.[48]

c. Imaging Quantification

As PET detects 511KeV gamma rays, the absolute quantitative parameters including standardized uptake value (SUV), %ID/g, and Bq/mL have been established for imaging analysis. However, imaging quantification in SPECT systems is generally considered a challenge. To date, SPECT is still arguably considered as a semi-quantitative imaging technique. Due to the use of collimators, SPECT only receives ~0.01% of the emitted photons, which is significantly less than that of PET for imaging reconstruction and data quantification.[47] In addition, because of a wide range of photon energies, the correction of photon attenuation is more difficult for SPECT systems to have accurate imaging quantification.[47]

BLI and FI

BLI and FI are optical imaging modalities with comparable spatial resolution of PET and SPECT.[24] Because both modalities can monitor *in vivo* biological events in real-time,[49] BLI and FI are gaining increasing applications. BLI is based on the detection of

visible light produced during an enzyme (luciferase)-mediated substrate oxidation, where the enzyme is expressed *in viv*o by a transfected reporter gene in specific tissue or target. On the other hand, FI monitors the fluorescent emissions by molecules as a consequence of the direct excitation of the molecules by an external light of appropriate wavelength.

Both BLI and FI are uniquely suited for high-throughput *in vivo* imaging because of the ease of operation, short acquisition times (typically between 1 and 30 seconds), and simultaneous measurement of multiple anesthetized mice. These features together with the relatively low cost allow for rapid testing of biological hypotheses and proof-of-concept studies in living experimental models.[50] However, the optical techniques are not so quantitative as desired, and the image information is surface-weighted.[2]

Multimodal Imaging Techniques

Generally speaking, US, CT, and MRI can provide exquisite anatomical information but are relatively limited by their sensitivities to afford the desired functional information. On the other hand, biological events at the cellular or molecular level can be revealed by nuclear (e.g. PET, SPECT) and optical imaging (e.g. BLI, FI) techniques but lack of the precise location of the events. As each imaging technique has its inherent advantages and disadvantages, the idea of using multimodal imaging techniques has recently gained popularity since the introduction of fused PET/CT system in 1998 because the information obtained by different techniques is largely complementary.[51] Multimodality imaging is defined to involve the incorporation of two or more imaging modalities within the setting of a single examination. While hybrid imaging modalities are on the rise and will become the mainstay of molecular imaging, the excitement over

these new systems has triggered a tumult of activity in probe design and development. In this dissertation, the imaging studies were performed on a microPET/CT system.

1.3 Imaging Probes

Most imaging techniques rely on imaging probes to provide imaging signal/contrast. In nuclear imaging, an imaging probe is a molecule tagged with a radionuclide to interrogate a biological event or process. For MRI and optical imaging, the radionuclide is replaced by a paramagnetic atom or fluorescence dye, respectively, in the corresponding imaging agent.

The design of an imaging probe is specific to the expected application of the probe. Imaging probes can be nonspecific or specific molecules. Although nonspecific imaging probes do not have a distinct set of targets, they can be used to obtain physiological information such as the changes of blood flow. These probes include most of the CT and MRI contrast agents for conventional medical imaging, and some nuclear imaging tracers (e.g. [^{99m}Tc]sestamibi and [^{15}O]H_2O). The design of specific imaging probes is usually based on biomolecules that can interact with targets in particular cells. These probes include most of radiotracers for nuclear imaging (e.g. [^{18}F]FDG for hexokinase and [^{111}In]DTPA-Octreotide for somatostatin receptor). The design of specific imaging probes is evaluated by the target-to-background ratio in their *in vivo* applications, which may reflect receptor density and turn-over rates in the target cells, and nonspecific cellular uptake. In MRI or FI, the so called "smart" imaging probes that can be activated by a specific biological environment or event (e.g. ion concentration,

pH, and enzyme) have drawn considerable attention in the community of molecular imaging.[52, 53] However, such a "smart" design is not feasible in nuclear imaging because the radioactive decay cannot be manipulated chemically or biologically.

The focus of this dissertation is on the design, synthesis, and evaluation of peptide-based nuclear imaging probes for lung cancer and pancreatic β-cells. Unlike the imaging probe designed for other imaging techniques such as MRI and optical imaging, the selection of radionuclide is the first step toward developments of nuclear imaging probes. For PET imaging probes, radioisotopes with abundant positron branching ratio but low maximum positron energy (e.g. ^{18}F) are desirable. For SPECT, gamma-ray emissions from radioisotopes must be in the energy detection window of sodium iodide crystals. Because nuclear imaging methods monitor the decay of the chosen radioisotope rather than the probe as whole, the probe must be stable *in vivo* during imaging procedure.

It is important that the labeling strategy does not alter the biological properties of the molecule to be tagged. In contrast to the activable or smart imaging probes in MRI or optical imaging,[52, 53] nuclear imaging probes produce always-on signals. An ideal nuclear imaging probe must demonstrate high specificity of its signals, which results from its rapid localization in target tissues and fast clearance from non-target organs (e.g. liver and kidney).

The physical half-life of a radionuclide and the biological half-life of the molecule to be labeled should be compatible. If the half-life of the isotope is too short, it would be challenging to complete the biological evaluations of the radiotracer. If it is too long,

unnecessary radiation exposure would be expected. Defined as the radioactivity per mass unit of the labeled and unlabeled molecule, specific activity (SA) is especially important to "saturable" binding studies, such as specific receptor/ligand binding. Therefore, it is highly desirable to prepare nuclear imaging probes with the highest achievable SA.[54] Because cost and availability of radioisotopes may also affect developments of radiotracers, they need to be considered as well.

1.4 Current Status of Nuclear Imaging

To date, quite a few endogenous proteins (e.g. receptors, transporters, or enzymes) have been used as targets for nuclear imaging. Methods based on analyzing the specific expression of a reporter gene have also been exploited for nuclear imaging. In the following sections, a few applications of nuclear imaging that gained acceptance are presented.

Imaging Glucose Utilization by [^{18}F]FDG-PET

In contrast to normal differentiated cells, most cancer cells rely on aerobic glycolysis for energy as well as building block acquisition.[55] Targeting this glucose metabolism pathway, several glucose analogs have been developed for cancer diagnosis and treatment.[56] [^{18}F]FDG was introduced by Di Chiro et al. in 1987 [57] and showed the correlated uptake with the malignant brain tumors. In the 1990s, [^{18}F]FDG-PET was seen in the diagnosis of lung cancer [58] as well as whole-body scans.[59] To date, [^{18}F]FDG-PET has become the most successful radiophatmaceutical.

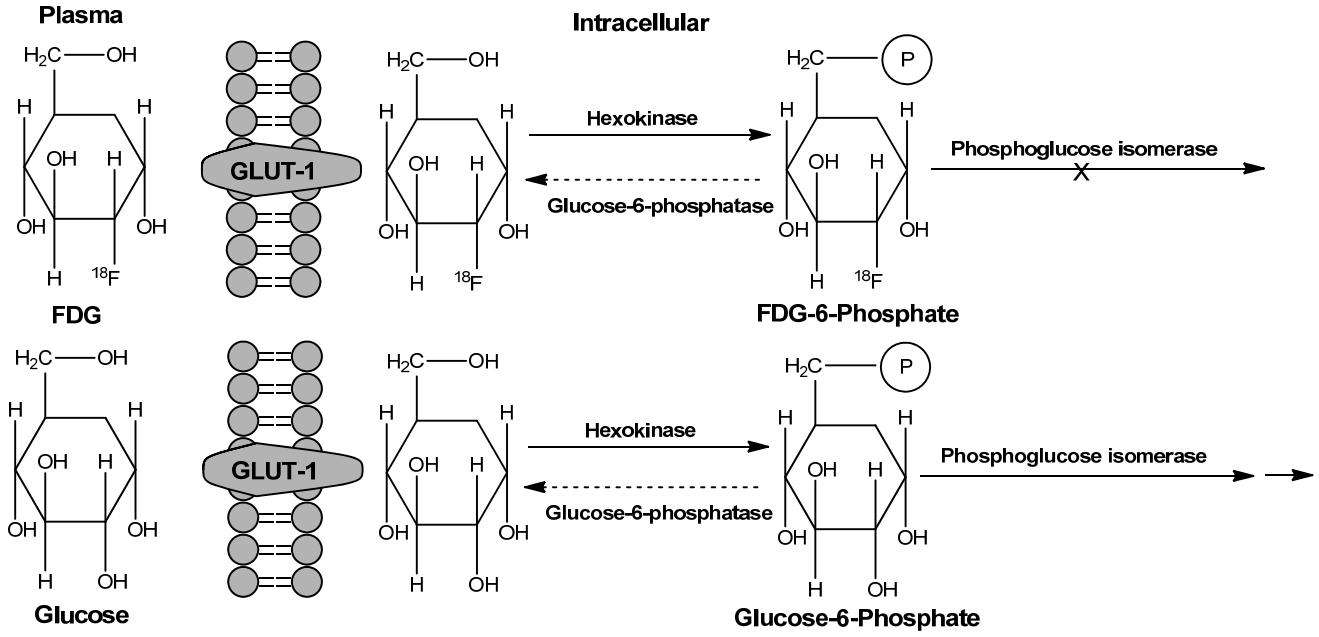

Figure 1.1 Physiological mechanism of [^{18}F]FDG and glucose. Both FDG and glucose are phosphorylated by hexokinase after the facilitated transport by GLUT-1. FDG-6-phosphate and glucose-6-phosphate can neither undergo further metabolism nor diffuse out of cells. As the dephosphorylation reaction occurs slowly and FDG-6-phosphate cannot advance to the next step of glycolysis, FDG-6-phosphate is trapped intracellularly and accumulates.

The molecular targets of [^{18}F]FDG are glucose transporters and hexokinase.[60, 61] [^{18}F]FDG enters cells through glucose transporters and is subsequently phosphorylated by hexokinase to become FDG-6-phosphate. Because FDG-6-phosphate lacks a hydroxyl group in the 2-position, it is not further metabolized. As FDG-6-phosphate is negatively charged, it remains trapped within cells (Figure 1.1).

As all cells utilize glucose, [^{18}F]FDG is not a specific PET probe. Physiological conditions like inflammation and infection may cause high [^{18}F]FDG uptake in affected tissues, which results in false positive diagnoses.[62, 63]

Imaging Rapid Cell Proliferation by Thymidine Analogs

Rapid cell proliferation is a characteristic of cancer cells, which leads to an elevated rate of DNA replication. Imaging cell proliferation has long been a goal of nuclear imaging research with most of the effort focused on radiotracers that can incorporated into DNA synthesis. *Ex vivo* assessments of cell proliferation in human tissues were first reported in 1960 with [^{3}H-methyl]thymidine ([^{3}H-methyl]TdR) [64] based on the fact that thymidine is the only nucleotide specific for DNA synthesis.

[^{11}C-methyl]thymidine ([^{11}C-methyl]TdR) was developed to image tumor proliferation.[65] Due to the short half-life of ^{11}C and the rapid catabolism of thymidine, analogs that are resistant to *in vivo* degradation have been developed and labeled with longer half-lived isotopes. Currently, 3'-deoxy-3'-[^{18}F]fluorothymidine ([^{18}F]FLT) and 1-(2'-deoxy-2'-[^{18}F]fluoro-1-β-D-arabinofuranosyl)-thymine ([^{18}F]FMAU) have been successfully used to image cell proliferation. Although [^{18}F]FLT is not incorporated into the DNA after phosphorylation, its uptake is correlated with tumor cell proliferation because its phosphorylation and trapping by thymidine kinase 1 reflects the rate of DNA replication.[66] To date, it has been accepted that [^{18}F]FLT is more specific than [^{18}F]FDG at identifying malignant cells, since the selective uptake of [^{18}F]FLT was observed in the tumor cells rather than inflammatory tissues.[67]

Imaging Protein Metabolism by Amino Acid Analogs

Proteins synthesis is a fundamental process for all cellular functions. As the rate of protein synthesis is increased to match the accelerated growth of cancer, the demand for amino acids as the building blocks of proteins is elevated. Therefore, it is expected that imaging of radiolabeled amino acid analogs could provide information with regard to

protein metabolism of malignant cells. Nearly all amino acids and slightly modified variants have been radiolabeled and evaluated for imaging protein synthesis. Among them, [^{11}C]methionine ([^{11}C]MET), [^{11}C]tyrosine ([^{11}C]TYR), [^{18}F]fluorethyl-tyrosine ([^{18}F]FET), and [^{123}I]iodomethyl-tyrosine ([^{123}I]IMT) have advanced to clinical trial.[68]

Protein metabolism can be observed by either the transport of amino acids from plasma into the cells or the rate of protein synthesis. It has been reported that the uptake of [^{123}I]IMT represents the increased transport of amino acids into tumor cells, while the uptake of [^{11}C]TYR is related to both amino acid transport and increased rate of protein synthesis.[68] The uptake of [^{11}C]MET is mainly determined by amino acid transport, although the effect of enhanced protein synthesis rate or other cellular processes cannot be excluded.[68] Imaging based on protein metabolism is less influenced by inflammation than [^{18}F]FDG-PET imaging. However, similar to [^{18}F]FDG, radiolabeled amino acid analogs are not specific to malignant cells

Imaging Cell Membrane Metabolism by [^{11}C]choline and [^{18}F]fluoromethylcholine

Choline is an important precursor in the synthesis of cell membranes. The uptake of choline appears to be driven by the activity of choline kinase.[69] As cancer cells require more building blocks for membranes, the enzyme activity is up-regulated. High levels of choline and its metabolites have long been known from MRS.[69] Because the virtual absence of bladder activity of [^{11}C]choline and [^{18}F]fluoromethylcholine compared to [^{18}F]FDG, this property has led to increasing applications of these imaging probes in prostate cancer diagnosis.[70]

Imaging Hypoxia by [^{18}F]FMISO and [^{64}Cu]ATSM

Tumor oxygenation is an important factor for cancer treatment, as hypoxia is related to poor prognosis.[71] To date, [^{18}F]Fluoromisinidazole ([^{18}F]FMISO) and ^{64}Cu labeled diacetylbis(*N*4-methylthiosemicarabaone) ([^{64}Cu]ATSM) have been developed to image tumor hypoxia. [^{18}F]FMISO diffuses into normal and cancer cells. Although reduction of [^{18}F]FMISO happens in both cell types, it can be reoxidized in normal cells and diffuse back, while in hypoxic cells, it gets further reduced and trapped.[72]

Compared to [^{18}F]FMISO, [^{64}Cu]ATSM could be a better choice for hypoxia imaging.[73, 74] The mechanisms underlying [^{64}Cu]ATSM retention are not well understood. Fujibayashi et al. first suggested that Cu(II)-ATSM reduction occurred only in hypoxic cells and was then irreversibly trapped.[75] Obata et al. observed that reduction of [^{64}Cu]ATSM in normal brain cells occurred in mitochondria, whereas it occurred mainly in the microsome or cytosol fraction in tumors. The retention involves the enzymatic reduction enhanced by hypoxia.[76] According to Dearling et al.[77] and Maurer et al.,[78] the reduction of Cu(II)-ATSM takes place in both normoxic and hypoxic cells. The resulting Cu(I) slowly dissociates from ATSM. Once the dissociation occurs, it is irreversible and Cu(I) is trapped. In normoxic conditions, Cu(I)-ATSM could be reoxidized by electron transport chain on the mitochondria and diffuse back out of the cell. However, reoxidation is much less likely in hypoxic cells and therefore the retention of [^{64}Cu]ATSM would be higher.

In addition to oxygen status, several studies have shown the tumor specific accumulation of [^{64}Cu]ATSM.[74, 79, 80] Recently, the expression of multidrug resistance

type1 (MDR 1) protein was reported to be one of the factors that affects the retention of [^{64}Cu]ATSM.[81]

Radiotracers to Image Exogenous Gene Expression

Reporter genes are widely used in molecular biology to monitor expression and/or repression of a gene of interest. To detect gene expression and regulation *in vivo* by nuclear imaging modalities, several reporter systems have been developed. Methods using either heterologous enzymes such as herpes simplex virus-1 thymidine kinase (HSV1-TK) or receptors/transporters such as dopamine D2 receptor (D2R), somatostatin receptor type 2 (SSTR2), sodium/iodine symporter (NIS), and norepinefrine transporter (NET) have been reported.[82] These imaging approaches have the potential to provide signal amplification and therefore increase sensitivity for detecting and localizing gene expression.

HSV-1 TK has been used extensively as a reporter gene for exogenous gene expression. The primary advantage of using HSV-1 TK in both therapeutic and imaging applications is its loose substrate specificity compared to endogenous TK in mammalian cells.[83] The use of radiolabeled nucleoside analogs to localize the expression of HSV-1 TK in living animals was first introduced by Saito et al.[84, 85] Since the initial reports, studies have been performed to improve the imaging of HSV-1 TK activity *in vivo*. To date, imaging the expression of HSV-1 TK has been well-established by using radiolabeled nucleoside analogs including derivates from ganciclovir, penciclovir, and 5-iodo-2'-fluoro-2'-deoxy-1-β-D-arabinofuranosyl-5-iodouracil (FIAU).[82]

The expression of D2R is primarily observed in the brain striatum and pituitary gland. Radiotracers including 3-3-(2'-[^{18}F]fluorethyl)spiperone ([^{18}F]FESP) and [^{123}I]iodobenzamine have been applied for imaging of D2R.[86, 87] However, dopamine binding to the D2R can perturb the underlying biological processes of the cell or tissue of interest.[88] To optimize D2R as a reporter gene, Liang et al. have generated a mutant D2R by point mutation.[88]

NIS is a membrane glycoprotein to transport both sodium and iodine into cells by sodium/potassium ATPase pump, which can be imaged by using an iodine radioisotope. However, the iodine radioactivity cannot be trapped in the transduced tissues, it is impossible to quantify the gene expression only based on the NIS imaging results.[89] As iodine is actively transported by NIS in the thyroid gland, breast epithelium, salivary glands, and gastric mucosa,[90] limited imaging sensitivity and specificity are expected in these and adjacent tissues.

Peptide-Based Radiotracers for Somatostatin and Other Peptide Receptors

Because of potential specific targeting, peptide-based radiotracers have attracted enormous attention for molecular imaging.[91, 92] The development of peptide-based imaging probes usually starts with a lead peptide sequence. An ideal peptide probe needs to exhibit high binding affinity, specific uptake, long retention in the target tissue, and *in vivo* stability against enzymatic degradation. When analyzing a native peptide with known targeting capability, the critical regions that contribute to peptide binding are often defined by studies of structure-activity relationships.[93, 94] These include truncation, alanine scans, D-amino acid scans, net charge changes, and hydrophobic characterization

of peptide sequence.[95] Once the regions are defined, replacement by unnatural amino acids and suitable restrictions (e.g. cyclization of the lead peptide sequence) may be further applied to improve its *in vivo* stability, binding affinity, and selectivity.[95]

To date, peptide-based radiopharmaceuticals are commonly seen in nuclear medicine. Structurally modified peptides can withstand harsh chemical conditions and their biological half-lives are compatible with the physical half-lives of most commonly used diagnostic radioisotopes.[91, 92] To develop peptide-based radiotracers, a targeting peptide must be radiolabeled efficiently with high specific activity. Various techniques of peptide labeling have been developed. Because most peptide-based radiotracers are less than 50 amino acids, the conjugations with chelating agents or prosthetic groups may influence their biological activities. As such, site-specific radiolabeling is usually required and a spacer is often incorporated to separate the radiolabel moiety from the peptide sequence. A few selected peptide-based radiotracers are discussed below.

Targeting Somatostatin Receptors (SSTR)

Somatostatin (SST) was first described in 1973 as a hypothalamic hormone that inhibits secretion of growth hormones.[96] The physiological action of SST-14 and SST-28 is mediated by five different SSTR that have been identified as SSTR-1 to SSTR-5.[97] SSTR-1, SSTR-2, and SSTR-3 have been reported to induce apoptosis, while SSTR-5 is related to inhibit cell proliferation. Because many cancer types including lung, pancreatic, and breast cancers [98-104] express an elevated level of SSTR, the SSTR system and the corresponding radiolabeled ligands have been extensively studied and evaluated.

^{111}In-DTPA-octreotide (^{111}In-OctreoScan) [105] and ^{99m}Tc-depreotide (Neotect) [106] are the first peptide-based radiotracers approved for clinical use in the US and Europe. However, because of their short biological half-lives (1.7-1.9 h) and inability to bind all SSTR, other analogs derived from octreotide and lanreotide have been developed to improve tracer pharmacokinetics and targeting specificity.[107, 108] To date, ^{68}Ga, ^{90}Y, and ^{177}Lu labeled DOTA-Tyr^3-octreotide have gained significant clinical relevance for PET imaging and peptide receptor radiotherapy.[109-111] In addition, ^{18}F labeled compounds with excellent properties for *in vivo* imaging and quantification were developed and evaluated in animal models and patients.[112-114]

Targeting Gastrin-Releasing Peptide Receptors (GRPR)

GRPR are G protein-coupled receptors overexpressed in human tumors including lung, colon, gastric, pancreatic, breast, and prostate cancers.[115, 116] Four mammalian GRPR subtypes have been characterized.[116] Bombesin (BBN), a 14-amino-acid peptide purified from amphibian skin,[117] was found to have high affinity and specificity for GRPRs. Because amino acids in the positions of 7-14 are important for BBN to bind GRPRs, radiotracers based on BBN (7-14) have been developed.[118-122] Currently, a ^{111}In labeled DTPA-bombesin analog appeared to be a promising radiotracer to image GRPR expressing tumors.[123] Phase I studies in patients with prostate cancer have been performed. However, the loss of GRPR receptors upon dedifferentiation of prostate cancer cells from androgen-dependent to androgen-independent growth may hamper its clinical applications.[124]

Targeting $\alpha_v\beta_3$ Integrin

The integrins are adhesion receptors for extracellular proteins. The $\alpha_v\beta_3$ is the most abundant integrin expressed on the surface of proliferating endothelial cells that recognizes the proteins exposing a three amino-acid sequence of arginine, glycine, and aspartate (RGD). The expression of $\alpha_v\beta_3$ is limited in most normal tissues,[125] but highly up-regulated in tumor vessels and some cancer cells.[126, 127] Noninvasive visualization of $\alpha_v\beta_3$ expression might provide information about the angiogenic process and the responsiveness of a tumor for antiangiogenic drugs. Radiotracers based on cyclic RGD analogs have been developed for nuclear imaging and peptide receptor radionuclide therapy in breast and prostate cancers,[128-130] where [^{18}F]galacto-RGD could effectively demonstrate the level of $\alpha_v\beta_3$ expression in human beings. To improve tumor-targeting efficiency and obtain better imaging properties, multimeric RGD peptide constructs have been developed to enhance the binding affinity toward the $\alpha_v\beta_3$ integrin. It has been reported that the ^{18}F labeled tetrameric RGD peptide {[c(RGDfE)HEG$_2$]K}$_2$-K-Dpr-[^{18}F]FBOA can strongly enhance the binding affinity toward the $\alpha_v\beta_3$ integrin compared with its monomeric and dimeric counterpart.[131]

Targeting Glucagon-like Peptide-1Receptors (GLP-1R)

GLP-1 is an intestinal peptide hormone that is secreted from L-cells of the gastrointestinal (GI) tract in response to the digestion of nutrients.[132] GLP-1 stimulates insulin secretion through GLP-1R. The expression of GLP-1R has been observed in the pancreas, brain, heart, kidney, stomach, and duodenum.[132, 133] Within the pancreas, GLP-1R is exclusively expressed on β-cells.[133] As GLP-1R is also highly expressed in insulinomas, radiolabeled GLP-1 and its metabolically more stable analogs, exendin-3

and exendin-4, have been reported for imaging of insulinomas.[134, 135] Recently, a clinical pilot study demonstrated that ^{111}In labeled exendin-4 could be used to localize human insulinomas and noninvasively confirm a precise and complete surgical tumor resection by SPECT/CT.[136]

1.5 Summary

As the genomic and proteomic signatures of different cell or tissue types emerge, an increasing number of promising targets are being identified. The goal of molecular imaging is to translate the knowledge obtained from molecular biology and genomic/proteomic research into *in vivo* visualization of biological events or processes. Nuclear imaging plays an important role in this transition due to its superior sensitivity, specificity, and quantitative features. To develop nuclear imaging probes, a multidisciplinary effort is always required. Once a biological target and its targeting molecules are selected, the imaging probe design must take a lot of factors into consideration including the radioisotope selection, the availability of the radioisotope, the precursor design, the highest achievable specific activity, and the *in vivo* kinetics and targeting properties of the designed probes. The overall research presented in this dissertation is to design, synthesize, and evaluate the peptide-based imaging probes for lung cancer and pancreatic β-cells. By acquiring the lead tracers for probe development, the knowledge obtained herein may provide further insights for the development of imaging probe. The imaging techniques developed in this work may help move the current diagnostic capability toward the goal of early diagnosis and disease-stratification

for better therapeutic interventions, which has been long pursued for individualized treatment as stated by the NIH roadmap.[5]

CHAPTER TWO

SPECIFIC AIMS, SIGNIFICANCE, AND GENERAL RESEARCH STRATEGY

2.1 Specific Aims

Conventional diagnostic methodologies of cancer and diabetes are limited by sensitivity and specificity. As a result, patients usually get diagnosed when the symptoms appear and the diseases are at the advanced stages. Because malignant tumors contain both normal and cancer cells in a particular organ/tissue [137-139] and the symptoms of diabetes only appear when more than 50% of pancreatic β-cell mass (BCM) is destroyed,[140-143] early detection of these diseases is highly desirable to have a cure or better clinical outcome. The ultimate goal of this work has been set to develop peptide-based radiotracers for imaging lung cancer and BCM. *The central hypothesis is that our peptide-based imaging probes can specifically bind to the molecular target for noninvasively monitoring the progression of lung cancer or diabetes.* To achieve this goal, three specific aims were arranged:

Aim 1: To design and synthesize novel imaging probes

The lead peptide sequences that have been used in this work were selected or synthesized in the laboratories of our collaborators. The precursors of our imaging probes were strategically designed based on the lead sequences and available radioisotopes. The radiochemical procedures were optimized to label the precursors with the choice of radioisotope. For the labeling with ^{18}F, an ^{18}F prosthetic group ([^{18}F]FBEM) was applied; while for the labeling with radiometal (^{64}Cu, ^{68}Ga, and ^{111}In), a macrocyclic-based

chelating agent (DOTA) was utilized. MALDI-MS and HPLC were applied for characterization and quality assurance.

Aim 2: To perform *in vitro* validation of the peptide-based radiotracers

The *in vitro* assays include phage blocking and receptor binding studies. The purpose of competitive displacement assays is to validate the binding specificity of the developed radiotracers. The studies are aimed to determine the ligand concentrations that inhibit 50% of the maximum specific binding (IC_{50}). The peptide conjugates with the measured IC_{50} values less than 10 nM were used for *in vivo* evaluations.

Aim 3 To perform *in vivo* validation of the peptide-based radiotracers. Two distinct subaims were arranged:

Aim 3a: To evaluate the biodistribution profiles and *in vivo* stability of our radiolabeled peptide conjugates

The biodistribution studies were conducted to evaluate the accumulation of our radiolabeled peptide conjugates in the tissue of interest. The blood and kidney homogenates were analyzed by HPLC for *in vivo* peptide stability.

Aim 3b: To validate the usefulness of our radiolabeled peptide conjugates for imaging of lung cancer or diabetes in designed or normal mouse models using a preclinical PET-CT dual-modality system

The imaging studies were performed on a Siemens Inveon small animal PET-CT system. Mice bearing H2009 ($\alpha_v\beta_6^+$) and H460 ($\alpha_v\beta_6^-$) tumors were used to validate our radiotracers for imaging the lung xenografts. The normal and STZ-induced diabetic mice were applied to identify the targeting properties of the radiolabeled peptide conjugates in

determining mouse BCM. Post imaging biodistribution studies, *ex vivo* imaging evaluations, and histology analysis were performed to verify our *in vivo* imaging findings.

2.2 Background and Significance

2.2.1 Targeted Imaging of Lung Cancer

In the United States, 170,000 new cases of lung cancer are diagnosed per year with an average five-year survival rate of 15%.[144] Based on the size and appearance of the malignant cells observed by microscopy, lung cancer can be categorized into small cell lung carcinoma (SCLC) and non-small cell lung carcinoma (NSCLC). The latter can be further classified into adenocarcinoma, squamous cell carcinoma, and large cell carcinoma.[145] The most common cause of lung cancer is long-term exposure of cigarette.[146, 147] Other factors include genetic background, and chronic exposure to radon gas, asbestos, and air pollution.[148-150]

A lung cancer diagnosis starts with a chest x-ray when patients have nonspecific shoulder pain or cough. However, this technique can only detect tumors with the size of centimeters in diameter. A variety of techniques have been developed to assist physicians in obtaining an accurate tissue diagnosis. Sputum cytology, bronchoscopy, and/or transthoracic needle aspiration are usually preferred when the type and stage of the cancer are less clear. Sputum cytology examines a sample of sputum under a microscope with 36-66% of identification rate.[151-154] Bronchoscopy together with biopsies is the test of choice in patients with central tumors.[155] It is a procedure that allows physicians to

view airways and obtain biopsy samples at the same time. Transthoracic needle aspiration is performed when bronchoscopy is not conclusive. This procedure has been shown to be more sensitive than bronchoscopy in patients with peripheral lung tumors.[155] However, 25-30% of the patients may develop complications such as internal bleeding and infections in pheumothorax after transthoracic needle aspiration.[156]

With excellent spatial resolution and hard tissue contrasts, CT has an established role in diagnosis of lung cancer. According to the American College of Radiology and the American College of Chest Physicians, a CT of the chest should be performed in patients with known or suspected lung carcinoma who are eligible for treatment.[157, 158] The Mayo Clinic experience showed that when high risk individuals (heavy smokers at the age of ≥ 50) are screened for lung cancer with CT, the possibility that they undergo a thoracic resection for lung cancer is increased by tenfold.[159] However, in another Mayo Clinic trial, there was a 70% rate of false-positive findings among all participants in the study.[160] The problem of CT in the prevalence of false-positive results from its diagnostic nature, which requires morphological changes of the tissue and availability of the reliable software.[161, 162]

With superior soft tissue contrasts and no ionizing radiation, MRI provides another useful technique for diagnosis of lung cancer. Although MRI is not a major modality for lung cancer diagnosis, it has been used for patients with superior sulcus tumors and extrathoracic metastases.[163, 164] However, as the tissue characterization of MRI relies on the detection of water protons, low proton density of the lung parenchyma and interfaces between alveoli and lung tissues creates unique challenges.[165]

Recently, the European Society for Medical Oncology (ESMO) has recommended FDG-PET for a better staging of NSCLC and suspected tumor recurrence.[166] However, because [^{18}F]FDG is known to have high nonspecific uptake in the gastrointestinal tract, brown fat, and arteriosclerotic plaques, it may result in incorrect tumor staging and diagnosis. In addition, artifacts caused by inflammatory tissues and benign tumors have also been reported.[167, 168] Although clinical reports suggest that the combination of FDG-PET with CT can play a better role in the diagnosis and management of lung cancer,[169-171] the development of new imaging probes that target tumor-specific biomarkers is warranted.

The $\alpha_v\beta_6$ Integrin Expression in Lung Cancer

The $\alpha_v\beta_6$ integrin has emerged as a new cell surface biomarker for several epithelial cancers types.[172-184] This integrin is over-expressed in many epithelial derived carcinomas but is not found in normal tissues.[184] It has been found that the $\alpha_v\beta_6$ expression is associated with poor patient survival in several cancer types.[176, 177, 185] Because the expression of the $\alpha_v\beta_6$ integrin is correlated with aggressive tumor phenotypes,[178-183] all of these findings indicate that $\alpha_v\beta_6$ can be used as a biomarker for the diagnosis and prognosis of lung cancer.

In 2003, an $\alpha_v\beta_6$-specific peptide (sequence: NH_2-RGDLATLRQLAQEDGVVGVR-$CONH_2$) was selected by biopanning a phage-displayed peptide library on the lung adenocarcinoma cell line H2009.[186] The evaluation of several truncated forms of this sequence afforded a 7-mer (NH_2-RGDLATL-$CONH_2$) and a 10-mer (NH_2-RGDLATLRQL-$CONH_2$) with non-compromised $\alpha_v\beta_6$ binding

affinity.[187] These $\alpha_v\beta_6$-binding peptides bind to $\alpha_v\beta_6$-expressing cells with half maximal binding affinities in the range of 6-10 nM, indicating their potential for *in vivo* applications. Therefore, it is possible to explore these peptides as molecularly guided imaging agents for the detection of $\alpha_v\beta_6$-positive tumors.

2.2.2 Imaging the Pancreatic β-Cells

β-Cells and Types of Diabetes

Pancreatic β-cells are located within the islets of Langerhans. In the islets, 65-80% of the cells are β-cells.[188] The major function of the β-cells is to secret insulin upon the glucose stimulation.

Diabetes is a disease characterized by high blood glucose levels that result from defects in the body's ability to produce and/or use insulin. There are two major forms of diabetes – Type 1 and type 2 diabetes. Type 1 diabetes (T1D) is usually found in children and young adults. It was previously known as juvenile diabetes. It is estimated that 5-10% of Americans who are diagnosed with diabetes are T1D patients.[189, 190] It has been shown that islet cell autoantibdies are strongly associated with the development of T1D, and insulitis is co-localized with an inflammatory infiltration of mononuclear cells.[191, 192] The appearance of autoantibody to one or several autoantigens triggers an autoimmune pathogenesis of β-cell destruction. Given a strong association between susceptibility to T1D and specific alleles of MHC class II genes, genetic factors are thought to be a major factor in the development of autoantibdies.[193-196] Although genetic susceptibility appears to be a prerequisite, studies on the risk of developing T1D using identical twins have shown that the concordance rate for the disease approaches only 40%,[197] suggesting that

environmental factors may be involved in the initiation and/or progression of β-cell destruction leading to T1D.

Viruses are one of the environmental factors that have long been suspected to cause the onset of T1D. To date, 14 different viruses have been reported to have a role in the development of T1D in humans and animal models.[198] It is now believed that viruses may either trigger β-cell specific autoimmunity leading to diabetes without direct infection of β-cells, or directly infect and destroy insulin-producing β-cells. It is believed that viral etiology of T1D in humans will be better understood by large prospective studies in pre-diabetic or genetically susceptible individuals and diabetic patients.

Type 2 diabetes (T2D) is the most common form of diabetes accounting for 90-95% of all diagnosed cases. While the onset of T1D directly reflects the loss of the pancreatic beta cells, T2D consists of multiple metabolic abnormalities leading to hyperglycemia. T2D begins with insulin resistance in peripheral tissues. As insulin sensitivity falls, insulin secretion increases substantially to maintain the normal blood glucose level.[199] When β-cells can no longer compensate for the insulin resistance, impaired glucose tolerance arises as the symptom of clinical diabetes.

To date, it is believed that obesity plays a major role in the pathogenesis of T2D. Previous reports indicated that the chances of impaired glucose tolerance and T2D increase as the increment of body mass index.[200-202] Other factors at molecular level, such as reduced expression of insulin receptors, alterations in the signal-transduction pathways, and mutations in the insulin-receptor gene, are associated with T2D.[203-206]

β-Cell Dysfunction and Diabetes Diagnosis

Diabetes progression can be characterized by five stages,[207] each of which is marked by important changes in the phenotype and function of the pancreatic β-cells. Stage 1 is defined as the increased insulin secretion to maintain normal glucose levels and compensate for the insulin resistance caused by obesity or genetic predisposition. Stage 2 occurs when a stable state of β-cell adaptation is reached to the glucose levels of 89-116 mg/dl. Stage 3 is a transient period of early β-cell decompensation. The glucose levels rise relatively rapidly to the stage 4, which is characterized by stable decompensation state with more severe β-cell dedifferentiation. The clinically apparent symptoms of diabetes start to appear in this stage. Finally, stage 5 represents profound β-cell failure with progression to ketosis. Although the progression of diabetes may be inevitable, several studies support the concept that movement across stages 1-4 can be reversible.[208, 209] According to the American Diabetes Association (ADA), people with blood glucose levels between 100-125 mg/dl can prevent or delay the development of T2D by up to 58% by simply changing their lifestyle, including modest weight loss and regular exercise.[208, 209] For patients with T1D, the regression from stage 4 to stage 2 can be observed as remission develops.[207]

Undiagnosed diabetes, especially T2D, has become a health problem in the United States. Based on National Diabetes Statistics from National Institute of Diabetes and Digestive and Kidney Diseases (NIDDK) in 2007, 5.7 million people with diabetes were undiagnosed,[210] which is one-third of all cases of the disease. In the United States, many patients at the time of diagnosis of diabetes already have diabetic complications.

Although people with undiagnosed diabetes may not be as hyperglycemic as are patients with established diabetes, they are still prone to have diabetic complications.

Early diagnosis of diabetes is critical to manage and treat the disease. According to U.K. Prospective Diabetes Study Group (UKPDS) in 1998,[211] the improvement of β-cell function is highly related to the concentration of blood glucose. In addition, the studies that were performed in the Diabetes Control and Complications Trial (DCCT) revealed the importance of maintaining blood glucose level in the normal range.[212, 213]

Fasting plasma glucose test (FPGT) and oral glucose tolerance test (OGTT) are currently the two major methods for diabetes diagnosis. Patients with positive results of either test are considered diabetic. These criteria were recently defined by the ADA.[210]

The hemoglobin A1c (HbA1c) is performed as an alternative approach for glycemic control in diabetes. The Japan Diabetes Association (JDS), the Diabetes Control and Complications Trial (DCCT), and UKPDS have achieved the standardized measurement of HbA1c. As HbA1c is an indirect marker that reflects current treatment instead of pancreatic function, HbA1c cannot be applied to assess the changes of functional β-cells in the diabetic progression.

Recently, measurement of c-peptide under standardized conditions has been proven as a well accepted and clinically validated assessment. Since c-peptide does not undergo hepatic clearance, and is not part of the human recombinant insulin used by diabetic patients, c-peptide level is the most appropriate parameter of reflecting β-cell function in human clinical trials to date.[214] However, because reduced insulin stimulation is compensated by remaining healthy β-cells, abnormalities are not normally observed by

these tests until pancreatic β-cell mass (BCM) is diminished by more than 50%.[215] As noninvasive *in vivo* assessment of BCM may provide useful information to monitor diabetes progression and effectiveness of any therapeutic interventions, such technology would be of great value to prevent or delay the onset of diabetes and help the management of diabetes.[208, 209]

The GLP-1R for BCM Imaging

Due to the small size (50-300 μm in diameter), scarce (1-2% of pancreatic mass) and scattered distribution,[216] it is a challenge to monitor BCM directly. To date, ^{11}C and ^{18}F labeled tetrabenzine derivatives, which specifically bind to vesicular monoamine transporter 2 (VMAT2), have shown the most promising potential of imaging BCM.[215, 217-221] However, because the expression of VMAT2 is not restricted to β-cells,[222, 223] non-specific binding of [^{11}C]DTBZ in other pancreatic cells or organs was also observed.[224] New strategies are needed for imaging pancreatic β-cells.

Glucagon-like peptide-1 receptor (GLP-1R) has been proposed as a potential target to image the β-cells but yet to be demonstrated.[225] GLP-1 is an incretin produced by intestinal L-cells and plays an important role in glucose homeostasis by sensitizing the pancreatic β-cells to produce insulin.[226] Therefore, GLP-1R can be used as a valid target to develop imaging probes for the assessment of BCM.

2.3 Research Design and Approach

2.3.1 Strategies for Peptide Radiolabeling

In general, the methods of labeling peptides are divided into three main categories: radiofluorination, radioiodination, and radiometal labeling.

Radiofluorination

Due to its ideal decay properties and availability, ^{18}F (97% β^+; $T_{1/2}$: 110 min) is the most widely used radionuclide for PET. Because peptides are highly protonated, labeling peptides with ^{18}F directly is not an option.[227] As such, use of a prosthetic group is essential. A prosthetic group is a radiolabeled small molecule that can be conjugated to peptides. Among the prosthetic groups developed to tag peptides via a free amine group, N-succinimidyl-4-[^{18}F]fluorobenzoate ([^{18}F]SFB) is the most widely used because it can provide relatively high radiochemical yield.[228]

Toward the synthesis of [^{18}F]SFB (Scheme 2.1), the formation of 4-[^{18}F]fluorobenzoic acid ([^{18}F]FBA) from an appropriate aromatic precursor is the first step. Conjugation of [^{18}F]FBA with succinimidyl group readily forms [^{18}F]SFB in the presence of *O*-(*N*-Succinimidyl)-*N*,*N*,*N*′,*N*′-tetramethyluronium tetrafluoroborate (TSTU) as a coupling agent in aceonitrile.[229-231] The average radiochemical yields of [^{18}F]FBA and [^{18}F]SFB are around 40% (decay-corrected) and 10% (decay-corrected). The total synthetic time to label peptides with ^{18}F via the prosthetic method is between 1.5-3 h with the overall radiochemical yield around 5% (decay-corrected).

Scheme 2.1 Radiosynthesis of [^{18}F]SFB

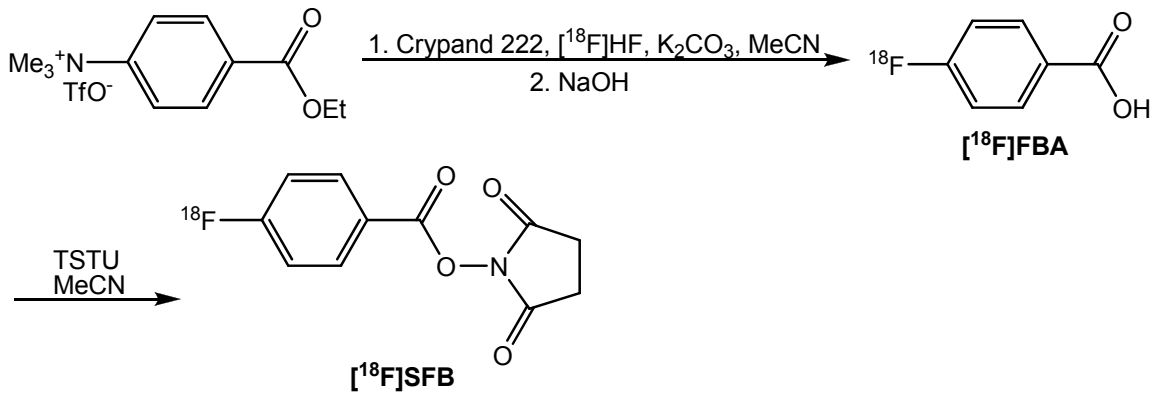

Because most of the peptide labeling procedures through the route of [^{18}F]SFB suffer from lengthy multistep synthesis, low radiochemical yields for the overall preparation are inevitable. In 2001, "click" chemistry was introduced (Figure 2.1) to label peptides with ^{18}F.[232, 233]

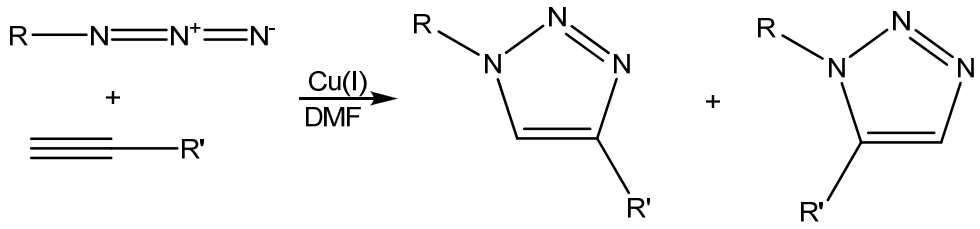

Figure 2.1 Schematic "click" chemistry : The azide-alkyne Huisgen cycloaddition

The "click" chemistry uses Cu(I) to catalyze azide-alkyne Huisgen cycloaddition, which has potential to couple ^{18}F precursor and peptides under a mild condition. By the approach of "click" chemistry, the total synthetic time can be reduced to 30-65 min with the radiochemical yield in the range of 50-80% (decay-corrected).

Recently, McBride et al. reported a methodology of radiofluorination of peptides by using a metal chelating moiety to complex an aluminum fluoride complex ion. The

total synthetic time was under 20 min with various radiochemical yields (5.8-87%, decay-corrected).[234]

In addition to using a free amine group for a peptide or protein labeling, thiol-reactive agents have also been widely used for modifications at specific sites through a reduced cysteine.[235, 236] The thiol-reactive agents include maleimides, acetyl halides, or pyridyl disulfides as a functional group (Scheme 2.2).[235, 236]

Scheme 2.2 Functional groups for peptide conjugation with thiol-containers

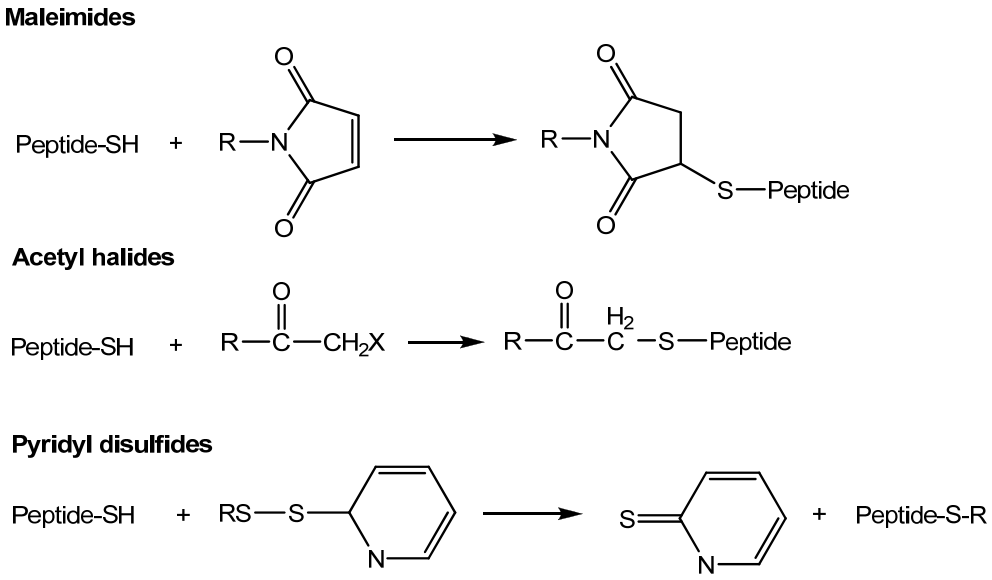

Among these functional groups, maleimides are usually preferred for peptide conjugation.[235, 236] Compared to acetyl halides and pyridyl disulfides, the standard maleimide reaction can be performed in the aqueous solution with pH around 7.5. This serves as the fundamental rationale to design ^{18}F labeled maleimide derivatives. Currently, N-[2-(4-[^{18}F]fluorobenzamido)ethyl]maleimide ([^{18}F]FBEM), N-[6-(4-[^{18}F]fluorobenzylidene)aminooxyhexyl]maleimide ([^{18}F]FBAM), 1-[3-(2-[^{18}F]fluoropyridin-3-yloxy)propyl]pyrrole-2,5-dione ([^{18}F]FPyME), and N-[4-[(4-

[^{18}F]fluorobenzylidene)aminooxy]butyl]maleimide ([^{18}F]FBAMB) have been reported for radiofluorination of peptides with a thiol group.[237-240]

Radioiodination

Radioiodination of peptides and proteins by $^{125/131}$I is widely used for biomedical research. Direct radioiodination is performed by an electrophilic substitution at a reactive aromatic amino acid within the peptide (Scheme 2.3).

Scheme 2.3 The general procedure of direct radioiodination

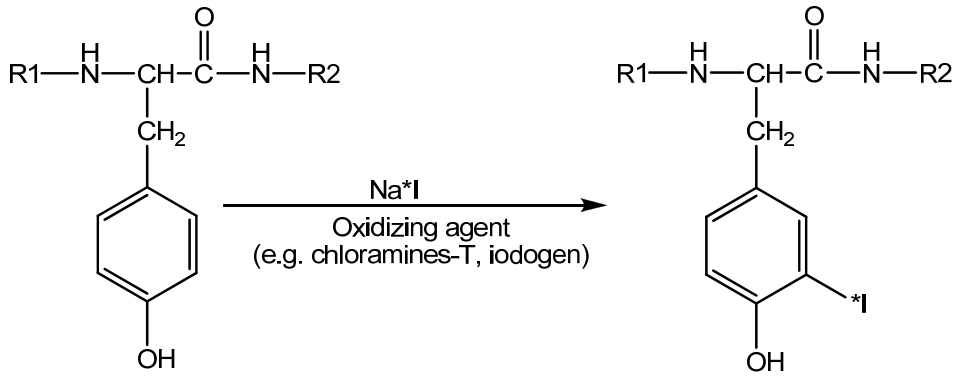

The reaction involves the covalent binding of radioiodine to the phenolic ring of tyrosine residues in the presence of an oxidizing agent (e.g. chloramine-T, iodogen).[241] Peptides with potential clinical applications could be prepared by replacing phenylalanine with tyrosine to allow direct radioiodination.[242, 243]

As some peptides are sensitive to oxidizing agents and/or may lose their function by replacing phenylalanine residues, indirect radioiodination was developed as an alternative approach (Scheme 2.4).[236, 244] In this method, the prosthetic group N-succinimidyl-3-(4-hydroxyphenyl) propionate (Bolton-Hunter reagent) is labeled with radioiodine followed by coupling with peptides via a free amine group without exposure of the peptide to harsh oxidation condition.[236, 244]

Scheme 2.4 The general procedure of indirect radioiodination

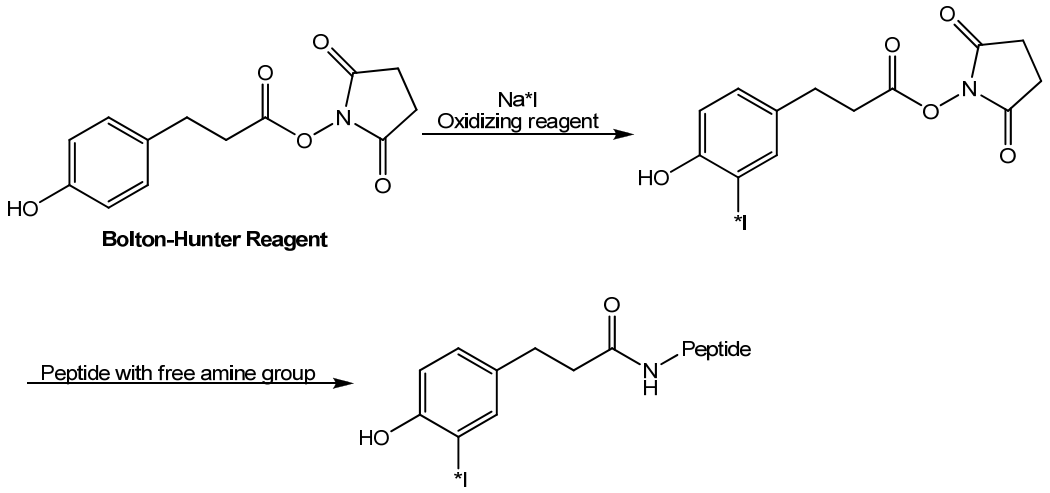

To date, N-succinimidyl-3-iodobenzoate (SIB) is currently the most widely used compound for indirect radioiodination (Figure 2.2).[244]

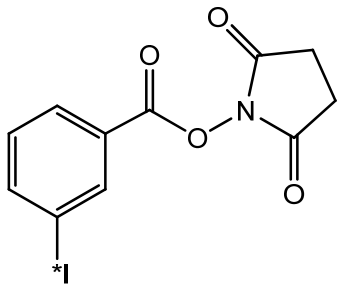

N-succinimidyl-3-iodobenzoate (SIB)

Figure 2.2 The chemical structure of SIB

Radiometal labeling

The procedures to label biomolecule conjugates with radiometals are well established. They can be categorized into three approaches: 1) direct labeling, 2) pre-labeling, and 3) post-labeling. Direct peptide labeling is easy to perform and has been applied to radiometals such as ^{99m}Tc and ^{188}Re.[245-247] This method involves the covalent binding of a radionuclide to thiol-containing side chains in the targeting molecules. However, the reaction is difficult to control and the radionuclide tends to be released

from the labeled peptides. In addition, direct binding of the radiometal to an amino acid side chain can greatly influence the peptide conformation, and further alters the targeting properties of the conjugate.

Peptide radiolabeling using pre- and post-labeling approaches is characterized by the use of bifunctional chelators (BFCs).[248] BFCs are multidentate ligands with two distinct functionalities, one for the covalent bonding with a biomolecule to be labeled, the other for radiometal complexation. An important selection criterion for BFCs is the *in vivo* stability of radiometal-BFC complex.

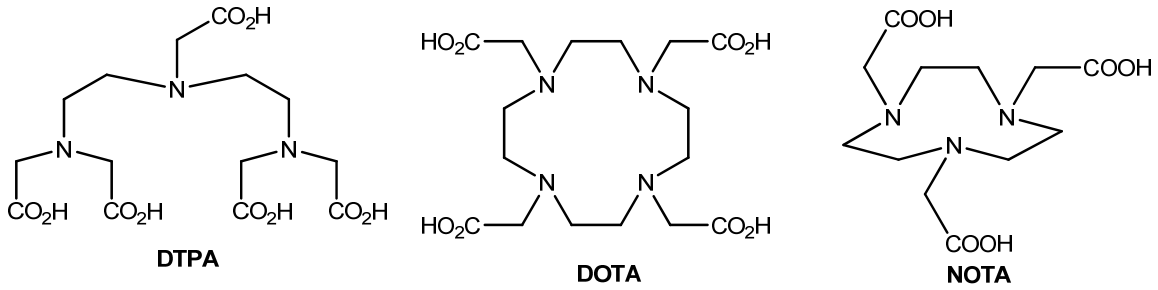

Figure 2.3 Chemical structures of DTPA, DOTA, and NOTA. (DTPA: diethylene triamine pentaacetic acid; DOTA: 1,4,7, 10-tetraazacyclododenane-1,4,7,10-tetraacetic acid; NOTA: 1,4,7-triazacyclononane-1,4,7-triacetic acid)

Gallium and indium belong the group in the periodic table IIIB. Interest in using ^{68}Ga for clinical PET comes from its readily availability from a generator, in which the parent isotope (^{68}Ge) has a physical half-life of 270.8 days. Indium-111 is a widely used gamma emitter for gamma scintigraphy and SPECT. The oxidation state of both metals in aqueous solution is +3. Despite their similarities, Ga(III) and In(III) are different in ionic radius and charge density. Ga(III) has an ionic radius of 0.65 Å with 6 as the coordination number in its complexes,[249] while the ionic radius of In(III) is 0.92 Å and its coordination number is either 7 or 8.[249] DTPA and DOTA (Figure 2.3) derivatives can be used as

BFCs to label biomolecules with ^{68}Ga and ^{111}In. However, because of smaller ionic radius, NOTA derivatives are more suitable for ^{68}Ga labeling.[250]

Copper has several radioisotopes that include ^{60}Cu, ^{61}Cu, ^{62}Cu, ^{64}Cu, and ^{67}Cu. The oxidation state of copper ion in aqueous solution is +2. Its coordination number could be 4, 5, or 6. Meares et al. first introduced cyclam and cyclen (Figure 2.4) for ^{67}Cu labeling of monocolonal antibodies.[251] Since then, DOTA and TETA (Figure 2.4) derivatives have been used for $^{64/67}$Cu labeling of biomolecules.[252]

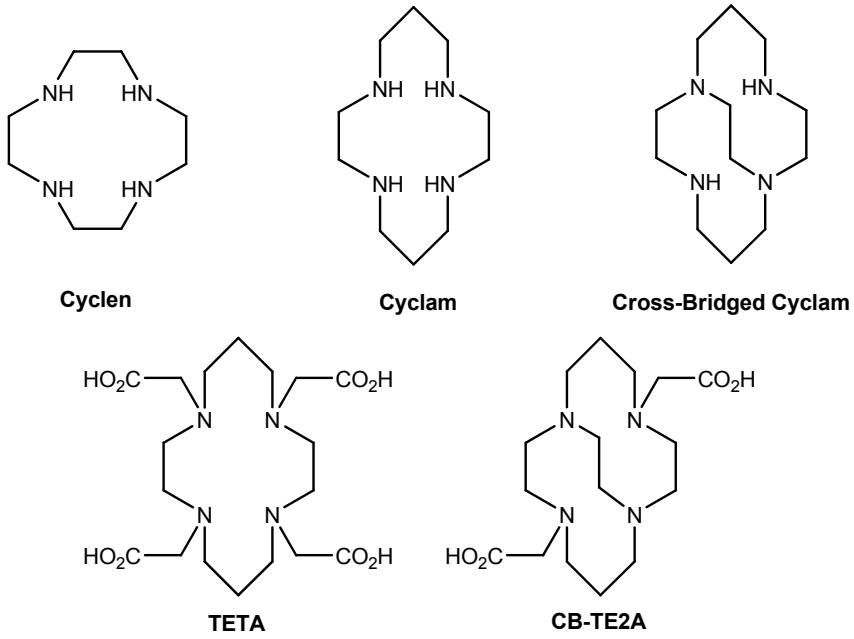

Figure 2.4 Chemical structures of cyclen, cyclam, cross-bridged cyclam, TETA, and CB-TE2A (TETA: 1,4,8, 11-tetraazacyclododenane-1,4,7,10-tetraacetic acid).

In order to enhance the chelating stability of $^{64/67}$Cu, the derivatives based on cross-bridged cyclam (Figure 2.4) have been developed. It has been reported that ^{64}Cu labeled CB-TE2A-bombesin conjugates have better *in vivo* stability compared to their DOTA counterparts.[253]

To conjugate chelators with biomolecules in either pre- or post-labeling approach, the chelators must be functionalized to have N-hydroxysuccinimide (NHS) ester, isothiocyanate, or maleimide (Figure 2.5). All of these functional groups are electrophiles. The selection of which electrophile to be used depends on the availability of the nucleophiles (e.g. primary amine or thiol group) on the biomolecule of interest as shown in Figure 2.5.

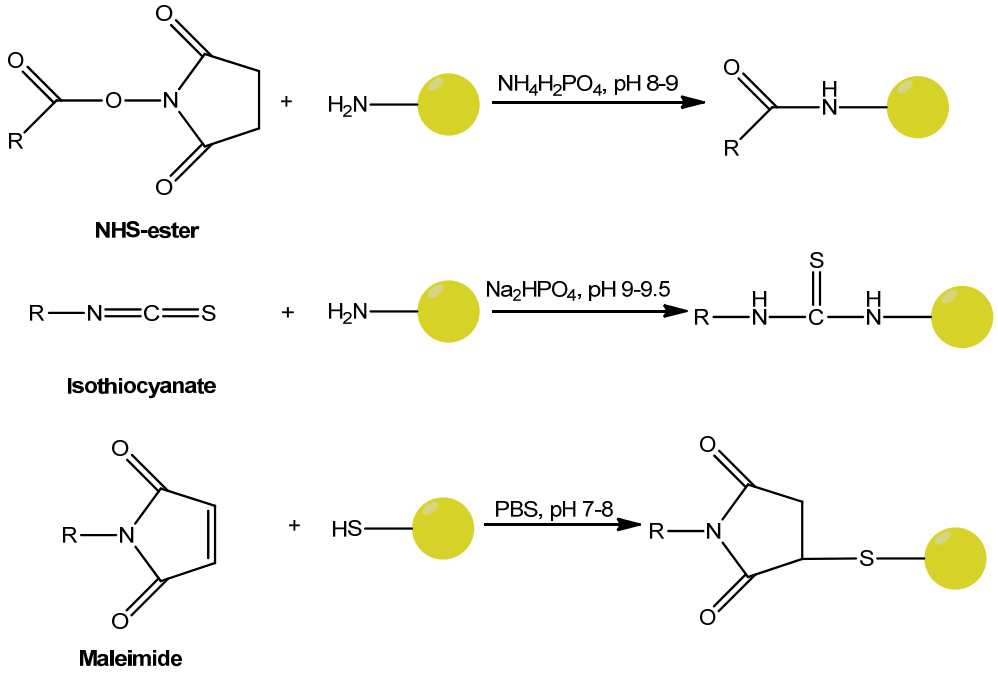

Figure 2.5 Conjugation reactions of BFCs with biomolecules.

The pre-labeling method in peptide labeling with radiometals is a two-step process, in which the radiometal-BFC complex is first formed and then conjugated to a peptide. As the labeling and conjugation steps are separated, this approach ensures that the radionuclide is attached directly to the BFC.[254] However, because this approach involves the radiometal into biomolecules in two steps, it could difficult be applied to radiometals with short half-lives.

In the post-labeling approach, a BFC is attached to the peptide and then the radionuclide is complexed. Because this approach has been used to label any peptide of interest and the BFC can be introduced at the N-, C-terminus, or amino acid side chain, it is currently the most popular method for labeling biomolecules.

Given the fact that nuclear imaging probes produce always-on signals, general considerations for the development of radiometal-based tracers include thermodynamic stability of the BFC-radiometal complexes and kinetically inert of the labeled biomolecules. As the complexes formed by acyclic chelators usually have lower thermodynamic stability than that of macrocyclic chelators, they are more prone to release radiometals *in vivo*.[255]

Kinetically inert of radiotracers is defined by their *in vivo* stability. The stability of a radiolabeled peptide not only has significant impact on its bioactivity, but also on clearance kinetics. Most peptide-based radiotracers that are successfully used for *in vivo* evaluations have plasma half-lives of more than 1 h.[256-258] Improved resistance to *in vivo* proteolysis has been achieved by truncation of the native peptide sequences, introduction of D-amino acids or unnatural amino acids at known cleavage sites, and peptide cyclization or modification.

2.3.2 General Strategies for *In Vitro* Evaluations

The *in vitro* evaluations of peptide-based radiotracers often include competitive displacement assays and stability tests. The purpose of competitive displacement assays is to validate the binding specificity of the developed radiotracers. The studies are aimed

to determine the ligand concentrations that inhibit 50% of the maximum specific binding (IC_{50}), and usually done with the radiotracer mixed with its unlabeled counterpart.

The stability of radiolabeled peptides can be evaluated in particular enzyme solution or serum at 37 ^{o}C for various time points. After protein precipitation and centrifugation, aliquots of the supernatant are analyzed by HPLC for monitoring the peptide degradation. In order to move into *in vivo* evaluations, the measured IC_{50} values of radiotracers are desired to be less than 10 nM. In addition, it is desirable to have high stability (> 80%) monitored at designed time points based on physical half-lives of tagged radioisotopes.

2.3.3 General Strategies for *In Vivo* Evaluations

Biodistribution and imaging studies are the most frequently performed assays for *in vivo* evaluations. For biodistribution studies, the animals receive certain amount of the radiotracer intravenously and sacrificed at various time points. Organs of interest are weighed and counted by a gamma-counter. On the other hand, imaging experiments are performed on anesthetized animals, where their biological events can be understood in the most relevant milieu. Both studies are aimed to track radiotracers of interest in experimental animals. The information generated from these studies provides clues for further radiotracer development.

2.4 Research Summary

Lung cancer and diabetes are the leading killers of both men and women in the United States. As nuclear imaging techniques have become a routine clinical practice and

a main powerhouse of molecular imaging, the goal of my work was to design, synthesize, and evaluate peptide-based imaging probes for lung cancer and pancreatic β-cell imaging. In Chapter 3 of the present work, we evaluated the peptides isolated from the phage displayed library for the detection of $\alpha_v\beta_6$-positive tumors. We analyzed the biodistribution profiles and tumor-targeting properties of the ^{111}In labeled peptides in a lung cancer xenograft mouse model. We systematically evaluated the effects of the addition of a PEG chain and site-specific labeling on the overall biodistribution of the peptides. We found PEGylation can enhance the tumor uptake of the peptide constructs, and the high kidney uptake problem can be reduced by altering the peptide modification sites.

In Chapter 4, we explored the use of GLP-1 analogs (Table 2.1) to image BCM. We found that the enzymatic degradation by DPP-IV can be prevented by the replacement of Ala^8 with D-Ala. The two lactam bridges of EM2198 were found to be effective in blocking the degradation by NEP 24.11. We demonstrated that GLP-1R is a potential biomarker for functional pancreatic β-cell imaging. Based on the *in vivo* imaging results of the ^{64}Cu labeled GLP-1 conjugates, EM2198 showed the pancreas region with the highest contrast.

Based on the evaluations that have been made, 10PD and EM2198 can be the lead compounds for future probe design and development. I further explored the dimeric form of 10PD for lung cancer imaging and established the procedure to label EM2198 with ^{18}F in Chapter 5.

Table 2.1 Sequences of the GLP-1 analogs and exendin-4

GLP-1 analog	Sequence
GLP-1	HAEGTFTSDVSSYLEGQAAKEFIAWLVKGR-Ahx-C
[D-Ala^{8}]GLP-1	HaEGTFTSDVSSYLEGQAAKEFIAWLVKGR-Ahx-C
EM2196	HaEGTFTSDVSSYLEEQAAKEFIEWLVKGR-Ahx-C
EM2198	HaEGTFTSDVSEYLEKQAAKEFIEWLVKGR-Ahx-C
Exendin-4	HGEGTFTSDLSKQMEEEAVRLFIEWLKNGGPSSGAPPP S-Ahx-C

*L-Ala^{8} of GLP-1 was replaced with D-Ala (denoted as a) to prevent the degradation by DPP4 enzyme and aminohexanoic acid (Ahx) was served as a spacer between the peptide and DOTA chelator.

CHAPTER THREE

TARGETING THE INTEGRIN $\alpha_v\beta_6$ FOR LUNG CANCER DETECTION

3.1 Introduction

A correct histopathological diagnosis of cancer is critical for an appropriate treatment. However, a precise classification of tumors remains a significant biomedical challenge. Studies show that pathologists frequently come to different conclusions with the same diseases.[259, 260] Historically, diagnosis of cancer has relied on histology and morphology of the tumor including immunohistochemical staining for individual proteins. Tumors with similar histology can have different clinical outcomes, stressing the need for more detailed molecular classifications. Generation of ligands specific for tumor markers has been suggested as a way to further classify tumors for treatment, assuming that identification of specific tumor biomarkers could be correlated with treatment regimes and outcomes.[261] Most efforts towards this goal have been focused on identification of tumor biomarkers and isolation of their corresponding antibody ligands. For example, tumors are often assessed for expression of certain tumor antigens such as EGFR and HER-2/neu.[262] It was reported that neuroendocrine markers could aid in the diagnosis of SCLC.[259] Furthermore, these data can be then used in combination with pathological classification and tumor staging to provide a better prognosis and direct a course of therapy.

Involved in cell-to-cell and cell-to-extracellular adhesion, integrins play an important role in tumor growth and metastasis. In mammals, there are 18 α and 8 β

subunits to generate 24 known integrins [263] allowing cells to recognize and respond to a variety of different extracellular molecules.

Although the regulation of cellular proliferation requires the participations of growth factors, kinases, cyclins, transcription factors, and other signal molecules, the expression of particular types of integrins are critical in the progression of solid tumors. For instance, the $\alpha_5\beta_1$ integrin plays a role in the regulation of proliferation of cancer cells.[264, 265] Cells overexpressing $\alpha_5\beta_1$ display an anchorage-independent growth, and this averts quiescence by skipping the check points of cell cycle. Expression of other integrins, in particular the $\alpha_2\beta_1$ and $\alpha_v\beta_3$ integrins, also influences cellular proliferation and differentiation.[266] It has been shown that the expression of $\alpha_2\beta_1$ suppresses the growth of breast carcinoma cells and induces the cell differentiation.[267] Loss of the $\alpha_2\beta_1$ integrin expression in breast epithelial cells plays a role in their transformation to cancer cells.[267] In contrast, the expression of $\alpha_v\beta_3$ leads to proliferation and has been found in various metastatic cancer types.[268-271]

Angiogenesis is a prerequisite for tumor growth by securing the nutrient supply to cancer cells. Studies have shown that the $\alpha_v\beta_3$ integrin is minimally expressed on normal blood vessels, but significantly up-regulated on vascular cells in human tumors.[125] This is because the $\alpha_v\beta_3$ integrin is involved in the interactions with vascular epithelial growth factor (VEGF) and vascular epithelial growth factor receptor 2 (VEGFR2).[272] Accumulating evidence indicates that other integrins (e.g. $\alpha_1\beta_1$, $\alpha_2\beta_1$, and $\alpha_5\beta_1$) may be also needed for tumor angiogenesis.[273-275]

The $\alpha_v\beta_6$ integrin has emerged as a new cell surface biomarker for several epithelial cancer types.[177-179, 276, 277] It is highly expressed in fetal tissues and a number of epithelial carcinoma and cancer cell lines.[184] On the contrary, the expression of $\alpha_v\beta_6$ in adult tissue is restricted to inflammation and wound healing, in which epithelial cells migrate to traumatized area to establish an intact epithelium at injured locations.[278] De novo expression of the $\alpha_v\beta_6$ integrin by transfection has been reported to promote proliferation of colon cancer cells *in vitro* and increases tumor growth in nude mice.[279] In addition, the $\alpha_v\beta_6$ integrin is found in premalignant oral epithelial dysplasias,[280] indicating its involvement in malignant transformation.

By examing human specimens, the $\alpha_v\beta_6$ integrin was observed in a significant number of patients with NSCLC.[176] The expression of $\alpha_v\beta_6$ was also found in both early and late stages of the disease.[176] Recently, $\alpha_v\beta_6$ has been reported as an independent prognostic factor for the survival of patients with NSCLC, in which patients with $\alpha_v\beta_6$-positive tumors are associated with reduced survival times.[176] All of these findings indicate that $\alpha_v\beta_6$ integrin has promising potential as a biomarker for the diagnosis and prognosis of lung cancer.

In search of $\alpha_v\beta_6$ specific peptide ligands, screening based on phage display technology has been proved as a plausible approach. The principle underlying this screening technique is that the proteins or peptides to be displayed are usually expressed as fusions with the phage coat protein pIII or pVIII.[281] Such fusion proteins are directed to the bacterial periplasm or inner cell membrane. The enrichment of phages that present a binding peptide/protein is achieved by the affinity selection of a page library on the

immobilized target. In this 'panning' process, binding phages are captured while nonbinding ones are washed off. The bound phages are eluted and amplified by re-infection of E. coli cells. The amplified phage population is subjected in turn to the next round of panning. In general, phage display requires three or more consecutive rounds of panning before a lead peptide/protein identified.

By *in vitro* panning approach using a series of lung cancer cell lines, Dr. Kathlyn Brown's Laboratory (Department of Internal Medicine, UT Southwestern) isolated several $\alpha_v\beta_6$ binding peptides.[186] One of the isolated peptides was identified with the sequence of RGDLATLRQLAQEDGVVGVR. Later it was found that this peptide sequence specifically binds to the $\alpha_v\beta_6$ integrin with high affinity (IC_{50} ~6 nM).[176] Further evaluations revealed that two truncated forms of this sequence (7-mer: NH_2-RGDLATL-$CONH_2$ and 10-mer: NH_2-RGDLATLRQL-$CONH_2$) have non-compromised $\alpha_v\beta_6$ binding affinity.[187] In collaboration with the Brown group, we set off to explore the potential of these sequences for lung cancer imaging.

The main objective of this part of work is to design, synthesize, and evaluate the conjugates of the 7-mer and 10-mer peptides. To optimize the conjugate design for the development of imaging probe, the effects of a PEG chain incorporation and site-specific DOTA conjugation have been evaluated in diseased models when labeled with ^{111}In ($t_{1/2}$: 2.8 d, 100 % EC).

3.2 Materials and Methods

General

All reagents and solvents were purchased from Sigma-Aldrich (St. Louis, MO) and used as received unless otherwise noted. Milli-Q water (18 MΩ-cm) was obtained from a Millipore Gradient Milli-Q water system (Billerica, MA). The 1.5 mL low adhesion vials and C_{18} Sep-Pak cartridge were purchased from USA Scientific (Ocala, FL) and Millipore (Billerica, MA), respectively. Fmoc-protected amino acids, 2-(1H-benzotriazole-l-yl)-1,1,3,3-tetramethyluronium hexafluorophosphate (HBTU) were purchased from EMD Biosciences Inc (San Diego, CA), anhydrous 1-Hydroxybenzotriazole (HOBt) from SynBioSci (Livermore, CA), N-Methylmorpholine (NMM) from Acros Organics (Geel, Belgium). The C_{18} Sep-Pak cartridge was conditioned with ethanol and water before use. Nitric acid (10 – 20%) used for acid wash was prepared by diluting 70% nitric acid with Milli-Q water. The ammonium acetate buffer (0.1 M, pH 6.5) was pretreated with Chelex 100 resin (Bio-Rad, Hercules, CA) before use. Indium-111 ($^{111}InCl_3$ in 0.05N HCl) was purchased from Trace Life Sciences (Denton TX) with radionuclidic purity ≥ 99.90%. Reverse-phase high performance liquid chromatography (RP-HPLC) was performed on a Waters 600E chromatography system with a Waters 2996 photodiode array detector and a Shell Jr. 1000/2000 single-channel radiation detector. H2009 ($\alpha_v\beta_6^+$) and H460 ($\alpha_v\beta_6^-$) cells were a kind gift from Dr. John D. Minna's laboratory (Hamon Center for Therapeutic Oncology Research, UTSW). Cell lines were maintained according to established protocols in DMEM and RPMI 1640 medium (Mediatech, Herndon, VA) supplemented with 5% Fetal Bovine Serum (FBS, Gemini Bio-products, Woodland, CA). Matrix-assisted laser desorption/ionization time-

of-flight (MALDI-TOF) mass spectra (MALDI-MS) were collected on a Voyager-DE™ PRO Biospectrometry Workstation (Applied Biosystems, Foster City, CA).

3.2.1 Peptide Synthesis

Peptide synthesis was performed in the Brown Laboratory on a Symphony™ Synthesizer (Rainin Instruments, Protein Technologies, Inc. Woburn, MA) by Fmoc solid-phase peptide synthesis on a Rink Amide AM resin (substitution level 0.71 mmol/g) using standard protocols. Fmoc-protected amino acids were coupled at a 5-fold excess using HBTU, HOBt and NMM coupling (45 min). Piperidine in DMF (20%) was employed to remove N-terminal Fmoc protecting groups. Fmoc-NH-$(PEG)_{11}$-COOH ($C_{42}H_{65}NO_{16}$, Polypure, Oslo, Norway) was coupled overnight in a single coupling step. Upon completion of the synthesis, peptides were cleaved from the resin using a TFA: triisopropylsilane: H_2O cocktail (95%:2.5%:2.5%) and precipitated in cold diethyl ether.

Table 3.1. Characterization of the derivatives of the 7-mer and 10-mer peptides by MALDI-MS

Peptide	Molecular Formula	M.W. (Calculated)	M.W. (Determined)
10-mer-PEG-Cys	$C_{78}H_{146}N_{20}O_{28}S$	1843.02	1844.18
10-mer	$C_{48}H_{88}N_{18}O_{14}$	1140.67	1141.35
10-mer-PEG	$C_{75}H_{141}N_{19}O_{27}$	1740.02	1740.88
7-mer-PEG-Cys	$C_{61}H_{115}N_{13}O_{24}S$	1445.78	1446.76
7-mer	$C_{31}H_{57}N_{11}O_{10}$	743.43	745.02
7-mer-PEG	$C_{58}H_{110}N_{12}O_{23}$	1342.78	1343.86

Crude peptides were purified by reverse phase HPLC using a Vydac PR-C18 column (250 mm × 22 mm, 10 μm) on a Breeze™ HPLC (Water Inc.). The flow rate was set at 10 mL/min using a gradient system with solvents of H_2O/0.1% TFA (solvent A) and acetonitrile/0.1%TFA (solvent B) starting from 90% solvent A by a linear ramp to 40% solvent B at 60 min. Elution of the peptides was monitored by UV absorbance at

220 mm. The purity of the peptides was determined to be greater than 95% by HPLC (Varian, PR-C18 column, 250 mm × 4.6 mm, 5 μm). The peptides were characterized by MALDI-MS with α-cyano-4-hydroxycinnamic acid as matrix (Table 3.1).

3.2.2 Peptide Conjugation with DOTA

To evaluate the effects of pegylation and N- or C-terminal DOTA conjugation on an imaging probe, six peptide derivatives from the 7-mer and 10-mer peptides have been synthesized and full characterized. To conjugate DOTA with the peptide at the C-terminus, a cysteine was introduced to the end of the PEG chain. For N-terminal DOTA conjugation, the coupling was a direct reaction with the terminal amine.

Peptide Conjugation via Thiol-Maleimide Coupling (Scheme 3.1)

The peptide conjugation with DOTA was achieved by reacting the peptide with a C-terminal Cys (0.5 μmol) with maleimidomono-amide-DOTA (Macrocyclics, TX) (2.5 μmol; molar ratio: 5:1) in 10 mM PBS (pH 6.4, containing 10 mM EDTA) for 2 h at room temperature (RT). The DOTA-peptide conjugates were purified by HPLC with a Waters XTerra C_{18} column (5 μm, 4.6 mm × 150 mm). The flow rate was set at 1 mL/min using a gradient system starting from 100% solvent A by a linear ramp to 100% solvent B at 50 min. Solvent A: 0.1% trifluoroacetic acid (TFA) in water (v/v); solvent B: 0.1% TFA in acetonitrile (v/v). The purified fractions were characterized by MALDI mass spectra with α-cyano-4-hydroxycinnamic acid.

Scheme 3.1 Preparation of DOTA-peptide conjugates via thiol-maleimide coupling

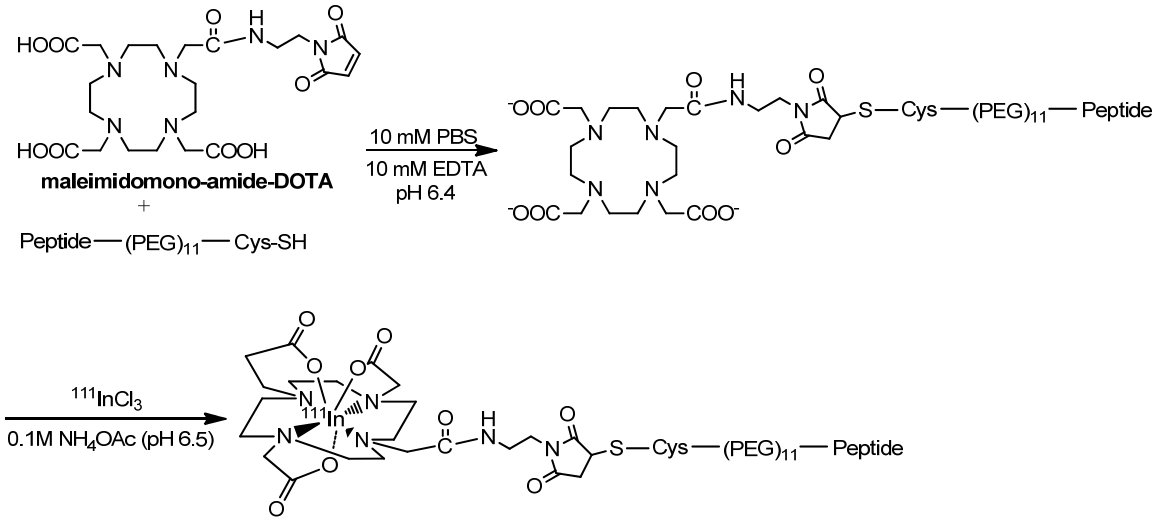

Peptide Conjugation via a Primary Amine (Scheme 3.2)

Conjugation of DOTA to N-terminus of the peptides was performed via a published procedure [282]. The carboxylate of DOTA tris(t-Bu ester) (Macrocyclics, TX) (2.5 μmol) was first activated by (7-Azabenzotriazol-1-yloxy)tripyrrolidinophosphonium hexafluorophosphate (PyAOP) (2.5 μmol) and then reacted with the peptides (0.5 μmol; molar ratio: 5:1) for 3 h at room temperature in DMSO. The crude product was purified by HPLC with a Waters XTerra C_{18} column (5 μm, 4.6 mm × 150 mm). The flow rate was set at 1 mL/min using a gradient system starting from 100% solvent A by a linear ramp to 100% solvent B at 50 min. Solvent A: 0.1% trifluoroacetic acid (TFA) in water (v/v); solvent B: 0.1% TFA in acetonitrile (v/v). The purified fractions were lyophilized followed by deprotection via 95% TFA. Purification of DOTA-peptide conjugates were carried out again by HPLC. The conjugates were characterized by MALDI-MS with α-cyano-4-hydroxycinnamic acid.

Scheme 3.2 Preparation of DOTA-peptide conjugates via a primary amine group

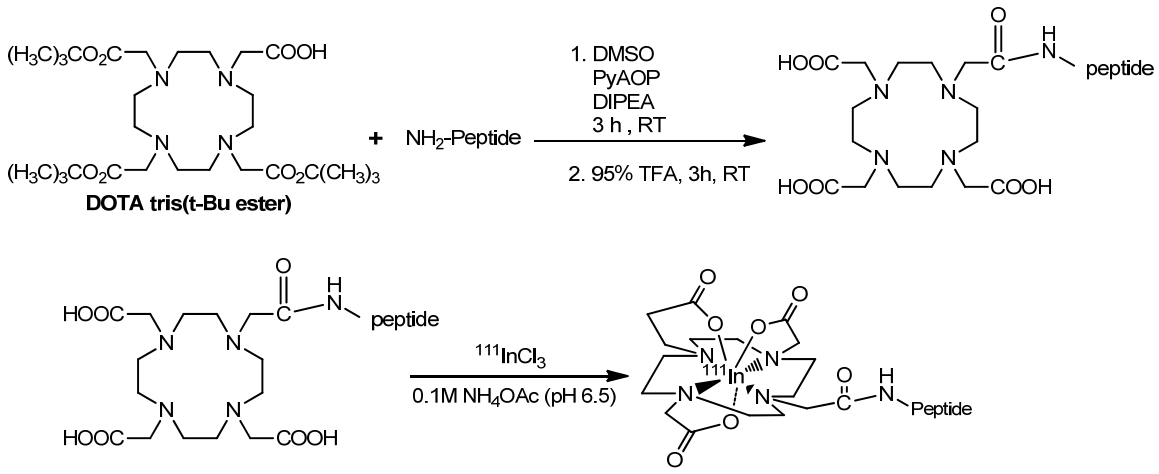

3.2.3 Radiochemistry

Aliquots of a peptide conjugate was dissolved with 50 μL of 0.4 M ammonium acetate (pH 6.5) followed by addition of $^{111}InCl_3$ (1 μL, 0.5-2.3 mCi). The reaction mixture was incubated at 37°C for 1 h in an Eppendorf thermomixer at a constant shaking rate of 600 rpm. After adding diethylenetriamine pentaacetic acid (DTPA, 5 mM, 5 μL) to challenge the nonspecifically bound ^{111}In, the labeled peptide was purified by a pre-activated C_{18} Sep-Pak cartridge. The HPLC analysis was performed to determine the radiochemical purity of each ^{111}In labeled peptide conjugate. The specific activity was calculated as the ratio of [(amount of the added radioactivity) × (radiolabeling efficiency determined by radio-TLC)] / (amount of the added peptide conjugate).

3.2.4 *In Vitro* Phage Blocking Assays

The purpose of this assay is to determine the effects of PEGylation/DOTA conjugation on the binding affinities of peptides. The abilities of the peptides and peptide conjugates to bind to H2009 cells ($\alpha_v\beta_6^+$) were performed according to the established

protocols.[187, 283] The H2009 cells were grown to 80-90% confluency in 12-well plates, and incubated with serum free RPMI 1640 medium for 2 h at 37 ^{o}C prior to the studies. A stock solution containing 1 × 10^{8} phage particles/mL, protease inhibitor (BoehringerMannheim), 100μM chloroquine, and serial dilutions (0 – 10,000 nM) of peptide conjugates were freshly prepared and added into the plates (1 mL/well). Recovery of the cell-associated phage was accomplished by incubation with K91 cells in the log phase of growth. The recovered phage number was further compared to the one without any addition of peptide conjugates. The readout obtained from this assay is defined as [(Number of phage plaques recovered with the presence of peptide conjugate)/ (Number of phage plaques recovered without the presence of peptide conjugate)] × 100%. The 50% inhibitory concentration (IC_{50}) values of the peptides and peptide conjugates were determined when 50% of the phage particles were recovered from K91 cells.

3.2.5 Cell Culture and Animal Model

The $\alpha_v\beta_6$-positive H2009 and $\alpha_v\beta_6$-negative H460 human lung cancer cell lines were cultured in DMEM and RPMI medium, respectively, with 5% fetal bovine serum (FBS) at 37 °C in 5% CO_2 atmosphere.

All animal studies were performed in compliance with guidelines set by the UT Southwestern Institutional Animal Care and Use Committee. The animal model was established by subcutaneous injection of a cell suspension (1 × 10^{6} H2009 or H460 cells) into the right flank of female severe combined immunodeficiency (SCID) mice. When

the xenografts reached the size of 50 – 200 mm^3 (measured by caliper; size = ½ × L × W × H [284]), the tumor-bearing mice were randomly grouped for the biodistribution studies.

3.2.6 Biodistribution and Urine Metabolism Studies

Each mouse was weighed and received 5 μCi of an ^{111}In labeled peptide conjugate intravenously. The mice were anesthetized and sacrificed at 20 min, 1 h, and 4 h p.i. (n = 4). Blood, lung, liver, spleen, kidney, muscle, fat, heart, and tumor were collected, weighed, and counted by a gamma-counter. The percentage of injected dose per gram (%ID/g) for each sample and the standard deviation (SD) for each group of the organ were determined by comparing the standards (n = 3) prepared along with the injection doses. For urine metabolism studies, mouse urine was collected along with biodistribution. Aliquots (20 μL) of urine were analyzed by HPLC.

3.2.7 *Ex Vivo* Immunohistochemical Staining

The H2009 tumor and kidney were excised from a sacrificed and perfused mouse. The tumor and kidney samples were frozen and cut into slices of 8 mm thickness. In a similar fashion, the kidney tissue slices were prepared for immunocytochemistry. To prevent nonspecific binding, sample sections were blocked with PBS containing 2% BSA and 2% goat serum. The tissue slices were treated with a 1:50 dilution rabbit anti-β_6 (H-110, Santa Cruz #15329) that recognizes the peptide region 621-730 of the β_6 subunit, which is conserved in both the mouse and human. After removal of the primary antibody and substantial washing, a 1:100 dilution of goat anti-rabbit IgG-FITC in blocking buffer was placed on the samples. Nuclei were counterstained with Hoechst 33258. Control

samples with sequential tissue slices were treated with secondary antibody (goat anti-rabbit IgG-FITC) alone.

3.2.8 Statistic Analysis

Quantitative data were processed by Prism 5 (GraphPad Software, La Jolla, CA) and expressed as Mean ± SD. All analyses were performed by one-way analysis of variance and Student's t test. P values < 0.05 were considered statistic significant.

3.3 Results

3.3.1 Preparation of DOTA-Peptide Conjugates and Radiochemistry

To evaluate the effects of pegylation and N- or C-terminal DOTA conjugation on the imaging probe, DOTA-Peptide conjugates were successfully prepared by coupling a thiol group with maleimidomono-amide-DOTA (average chemical yield: 60%) or an primary amine with DOTA tris(t-Bu ester) (average chemical yield: 40%) (Table 3.2).

Table 3.2. Sequences and MALDI-MS characterization of the DOTA-peptide conjugates

Peptide Name	Peptide Sequence	Molecular Formula	M.W. (Cacl'd)	M.W. (Det'd)
10PD	NH_2-RGDLATLRQL-$(PEG)_{11}$-C(DOTA)-$CONH_2$	$C_{100}H_{182}N_{26}O_{37}S$	2372.73	2370.20
D10P	DOTA-NH- RGDLATLRQL-$(PEG)_{11}$-$CONH_2$	$C_{91}H_{169}N_{23}O_{34}$	2329.45	2134.40
D10C	DOTA-NH- RGDLATLRQL-$CONH_2$	$C_{65}H_{117}N_{22}O_{20}$	1526.76	1530.50
7PD	NH_2-RGDLATL-$(PEG)_{11}$-C(DOTA)-$CONH_2$	$C_{83}H_{151}N_{19}O_{33}S$	1975.26	1977.20
D7P	DOTA-NH- RGDLATL-$(PEG)_{11}$-$CONH_2$	$C_{74}H_{138}N_{16}O_{30}$	1732.98	1733.10
D7C	DOTA-NH- RGDLATL-$CONH_2$	$C_{48}H_{86}N_{15}O_{16}$	1129.29	1133.00

At the non-carrier-added (n.c.a.) level, all peptide conjugates were successfully labeled with ^{111}In in 0.4 M ammonium acetate (pH 6.5). By reacting 10 μg of the peptide conjugate with 0.5-2.3 mCi of ^{111}In, more than 50% radiochemical yield was obtained.

The recovery rate after purification by a pre-activated C_{18} Sep-Pak cartridge was > 75%. The radiochemical purity of the labeled peptide conjugates was > 99% as determined by HPLC. The retention time of ^{111}In labeled 7PD, D7P, D7C, 10PD, D10P, and D10C on the HPLC was 19.07 min, 19.65 min, 15.95 min, 20.02 min, 21.62 min, and 20.45 min, respectively. The highest achievable specific activity acquired for each conjugate was 1.15×10^4 MBq/μmol. The reaction conditions that were used to acquire the highest specific activity are shown in Table 3.3.

Table 3.3 Reaction conditions for the ^{111}In labeled peptide conjugate

^{111}In (μCi)	10PD (μg)	NH_4OAc (pH 6.5)	Labeling efficiency	Radochemical yield*
167	0.2	50 μL	2.90%	0%
173	0.4	50 μL	26.42%	11.79%
166	0.8	50 μL	63.45%	37.35%
188	1.6	50 μL	65.89%	55.32%

*The labeled peptide was eluted by a pre-activated C_{18} Sep-Pak cartridge with 70% EtOH.

3.3.2 *In Vitro* Phage Blocking Assays

Given the reported role of the RGD motif in the specific $\alpha_v\beta_6$ binding affinities of the 7-mer and 10-mer, DOTA conjugation at the N-terminus may severely affect the specific binding of the corresponding conjugates.[176] As the peptide was initially selected as a bacteriophage clone through biopanning on the human lung adenocarcinoma cell line H2009, we examined the ability of D10P to block the binding of its cognate phage on H2009 cells by a phage blocking study. Interestingly the result indicates no negative effect of the N-terminus DOTA capping on the specific $\alpha_v\beta_6$ binding affinity as shown in Figure 3.1. The IC_{50} value of D10P is 5.98 ± 1.56 nM, which is even slightly improved as compared to its uncapped counterpart (10P: 7.19 ± 1.25 nM)

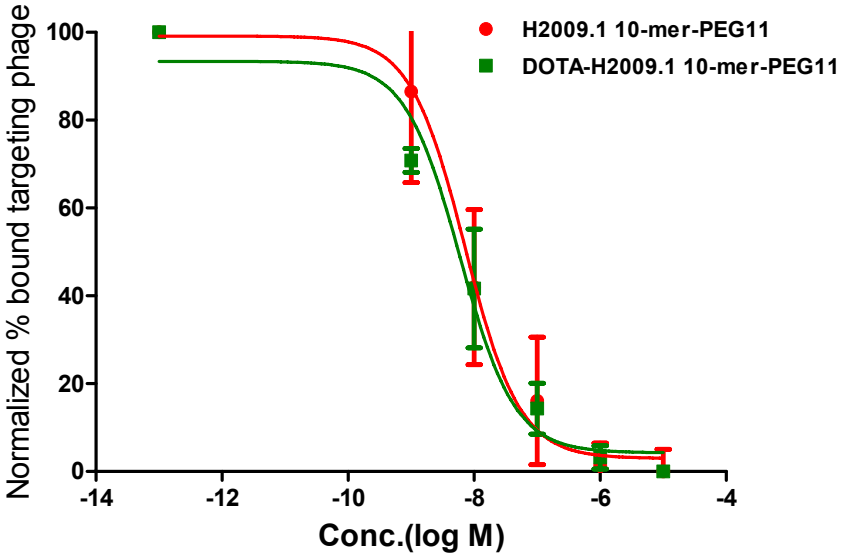

Figure 3.1 Inhibition of bacteriophage uptake by the 10-mer peptide and D10P to target $\alpha_v\beta_6$. The ratio of output phage to input phage in the presence of peptide normalized to the output/input ratio with no peptide added. The number of input phage particles was held constant. The IC_{50} values for H2009.1 10-mer-PEG11 and DOTA-H2009.1 10-mer-PEG11 (D10P) are 7.19 ± 1.25 and 5.98 ± 1.56 nM, respectively

3.3.3 *In Vivo* Evaluations

To prove of the principle, the biodistribution studies based on ^{111}In labeled 10PD in the mice bearing H2009 ($\alpha_v\beta_6^+$) or H460 ($\alpha_v\beta_6^-$) tumor were first performed (Table 3.4). The data from the mice bearing tumor sizes less than 225 mg were selected for comparison. At 1 h p.i., no significant difference was observed between the uptake in the $\alpha_v\beta_6$-negative tumor (H460: 1.29 ± 0.61 %ID/g) and $\alpha_v\beta_6$-positive tumor (H2009: 1.99 ± 0.57 %ID/g; p = 0.1011). However, the uptake of 10PD in the H2009 tumor became significantly higher than that in the H460 tumor (H2009: 1.37 ± 0.31 %ID/g; H460: 0.39 ± 0.07 %ID/g; p = 0.0003) at 4 h p.i., which suggests the preferential binding of the peptide conjugate in the $\alpha_v\beta_6$-positive tumor. The uptake of 10PD in both animal models

was comparable in the blood, lung, liver, spleen, kidneys, muscle, fat, and heart at 1 h and 4 h p.i., which indicates the consistency of 10PD in the non-target tissues.

Table 3.4 Biodistribution of ^{111}In labeled 10PD in mice bearing H460 and H2009 tumor xenografts at 1 and 4 h p.i. (H460 tumor: n = 4; H2009 tumor: n = 6). Data are presented as %ID/g ± standard deviation (s.d.).

	H460 tumor-bearing mice		H2009 tumor-bearing mice	
Tissue	1 h	4 h	1 h	4 h
blood	0.92 ± 0.04	0.34 ± 0.22	0.84 ± 0.47	0.28 ± 0.10
lung	0.94 ± 0.06	0.34 ± 0.04	0.88 ± 0.34	0.31 ± 0.08
liver	0.56 ± 0.07	0.47 ± 0.04	0.42 ± 0.15	0.36 ± 0.06
spleen	0.38 ± 0.07	0.36 ± 0.04	0.35 ± 0.15	0.26 ± 0.04
kidney	44.69 ± 5.97	54.81 ± 17.60	45.89 ± 10.28	50.69 ± 17.00
Muscle	1.41 ± 1.12	0.24 ± 0.07	0.24 ± 0.09	0.15 ± 0.10
fat	0.38 ± 0.24	0.12 ± 0.03	0.18 ± 0.21	0.11 ± 0.03
heart	0.42 ± 0.04	0.22 ± 0.04	0.35 ± 0.18	0.16 ± 0.04
tumor	1.29 ± 0.61	0.39 ± 0.07	1.99 ± 0.57	1.37 ± 0.31
tumor/muscle	0.94 ± 0.92	1.35 ± 0.91	8.85 ± 2.07	10.49 ± 3.62
tumor/lung	1.37 ± 0.60	1.15 ± 0.16	2.42 ± 0.60	4.58 ± 1.19

In order to verify the targeting specificity of 10PD, we further compared the biodistribution profiles of the scrambled version of 10P (S10PD) (sequence: NH_2-DALRLQGTLR-$CONH_2$) and 10PD in the mice bearing the H2009 tumor. S10PD has the same amino acid composition as 10PD but with different sequence. As shown in Table 3.5, the H2009 tumor uptake of S10PD at both 1 and 4 h p.i. was significantly less than that of 10PD (1 h: S10DP: 0.71 ± 0.11 %ID/g; 10PD: 1.99 ± 0.57 %ID/g; p = 0.0024; 4 h: S10PD: 0.54 ± 0.05 %ID/g; 10PD: 1.37 ± 0.31 %ID/g; p = 0.008). Its accumulation in the blood, lung, liver, spleen, muscle, fat, and heart was comparable to 10PD. Compared to the H460 tumor uptake of 10PD (Table 3.4), the H2009 tumor uptake of S10PD was comparable at 1 h p.i. (p = 0.1105) but slightly higher at 4 h p.i. (p = 0.0130), which confirms the non-specific accumulation of 10PD in the H460 tumors.

As 10PD provided fast clearance from non-target tissues (e.g. blood, lung, liver, spleen, muscle, fat, and heart) and excellent contrasts on the H2009 tumors compared to the muscle and lung, 10PD has the potential to be developed as an imaging probe for the $\alpha_v\beta_6$-positive tumors. However, the significantly less kidney uptake of S10PD compared to 10PD (1 h: S10PD: 18.92 ± 7.25 %ID/g; 10PD: 45.98 ± 10.28 %ID/g; p = 0.0001; 4 h: S10PD: 14.48 ± 0.92 %ID/g; 10PD: 50.69 ± 17.00 %ID/g) led to the possibility that the kidney may highly express $\alpha_v\beta_6$. In order to answer this question, we sacrificed the mice and performed immunohistochemical staining.

Table 3.5 Biodistribution of ^{111}In labeled scrambled 10-mer and 10PD in the mice bearing H2009 xenograft at 1 and 4 h p.i. (S10PD: n = 4; 10PD: n = 6). Data are presented as %ID/g ± s.d.

	S10PD		10PD	
Tissue	1 h	4 h	1 h	4 h
blood	1.24 ± 0.22	0.52 ± 0.02	0.84 ± 0.47	0.28 ± 0.10
lung	1.08 ± 0.17	0.42 ± 0.03	0.88 ± 0.34	0.31 ± 0.08
liver	0.82 ± 0.20	0.69 ± 0.15	0.42 ± 0.15	0.36 ± 0.06
spleen	0.40 ± 0.03	0.36 ± 0.06	0.35 ± 0.15	0.26 ± 0.04
kidney**	18.92 ± 7.25	14.48 ± 0.92	45.89 ± 10.28	50.69 ± 17.00
muscle	0.12 ± 0.02	0.11 ± 0.06	0.24 ± 0.09	0.15 ± 0.10
fat	0.11 ± 0.08	0.12 ± 0.03	0.18 ± 0.21	0.11 ± 0.03
heart	0.41 ± 0.10	0.19 ± 0.01	0.35 ± 0.18	0.16 ± 0.04
tumor*	0.71 ± 0.11	0.54 ± 0.05	1.99 ± 0.57	1.37 ± 0.31
tumor/muscle	4.96 ± 2.19	5.56 ± 1.87	8.85 ± 2.07	10.49 ± 3.62
tumor/lung	0.71 ± 0.21	1.29 ± 0.07	2.42 ± 0.60	4.58 ± 1.19

* indicates $p < 0.01$ between both groups at 1 and 4 h p.i.
* *indicates $p < 0.001$ between both groups at 1 and 4 h p.i.

On the basis of immunostaining (Figure 3.2), the H2009 tumor was positively stained by the anti-β_6 antibody. No staining was observed in the kidneys, which suggests that the high renal accumulation of 10PD may be contributed by other mechanisms.

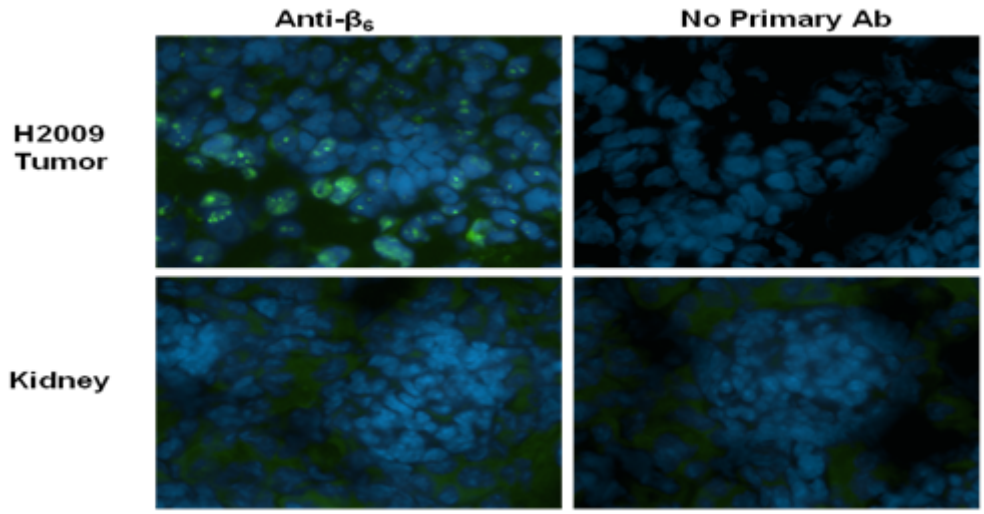

Figure 3.2 Immunohistological analyses of the H2009 tumor and kidney sections. Optimum cutting temperature (OCT)-embedded sections from the mouse kidneys and tumors were processed and stained. The sections are at 100× magnification.

Because the signal of a nuclear imaging probe is from the radioactive decay, the stability of an imaging probe against the enzymatic degradation is actually important since the metabolites of the radioisotope have their own tissue distribution profiles. In this regard, we further analyzed the urine metabolites of 10PD. As shown in Figure 3.3, the peptide conjugate was completely degraded after 1 h injection, in which the retention time of the major metabolites was 16 min. Based on this observation, we proposed to change the labeling site from C-terminus to N-terminus of the peptide construct in hope to alleviate the problem of high kidney uptake. In addition, by capping the peptide sequences at both N- and C-terminus with DOTA and PEG chain, we expected to render the peptide conjugates with desired *in vivo* stability.

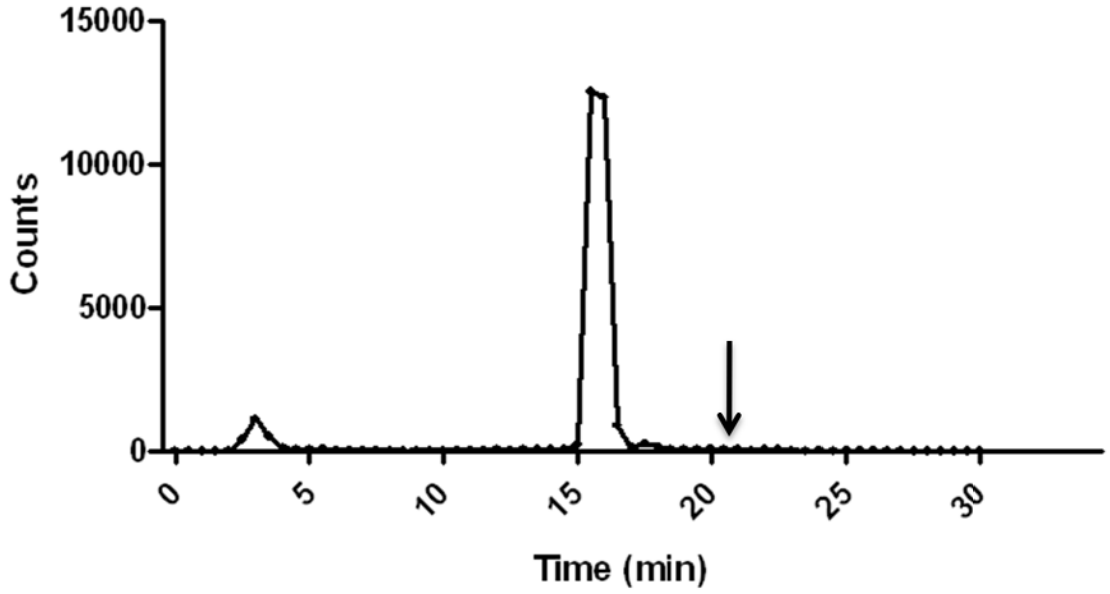

Figure 3.3 The HPLC analysis of metabolites of ^{111}In labeled 10PD in mouse urine. The arrow indicates the retention time of the intact peptide conjugate, which differs from its metabolites.

The kidney uptake was significantly reduced (1 h: D10P: 7.30 ± 1.12 %ID/g; 10PD: 45.98 ± 10.28 %ID/g; p = 0.0001; 4 h: D10P: 6.40 ± 0.99 %ID/g; 10PD: 50.69 ± 17.00 %ID/g) by comparing the biodistribution profiles (Table 3.6).

Table 3.5 Biodistribution of ^{111}In labeled D10P and 10PD in the mice bearing H2009 xenograft at 1 and 4 h p.i. (D10P: n = 4; 10PD: n = 6). Data are presented as %ID/g ± s.d.

	D10P		10PD	
Tissue	1 h	4 h	1 h	4 h
blood	1.10 ± 0.20	0.49 ± 0.05	0.84 ± 0.47	0.28 ± 0.10
lung	0.85 ± 0.21	0.46 ± 0.07	0.88 ± 0.34	0.31 ± 0.08
liver*	0.85 ± 0.15	0.99 ± 0.04	0.42 ± 0.15	0.36 ± 0.06
spleen*	0.69 ± 0.13	0.91 ± 0.21	0.35 ± 0.15	0.26 ± 0.04
kidney**	7.30 ± 1.12	6.40 ± 0.99	45.89 ± 10.28	50.69 ± 17.00
muscle	0.26 ± 0.07	0.18 ± 0.02	0.24 ± 0.09	0.15 ± 0.10
fat	0.31 ± 0.13	0.25 ± 0.06	0.18 ± 0.21	0.11 ± 0.03
heart	0.48 ± 0.13	0.28 ± 0.05	0.35 ± 0.18	0.16 ± 0.04
tumor*	1.04 ± 0.08	0.68 ± 0.07	1.99 ± 0.57	1.37 ± 0.31
tumor/muscle	3.99 ± 1.09	3.75 ± 0.67	8.85 ± 2.07	10.49 ± 3.62
tumor/lung	1.27 ± 0.22	1.52 ± 0.20	2.42 ± 0.60	4.58 ± 1.19

* indicates p < 0.01 between both groups at 1 and 4 h p.i.
** indicates p < 0.001 between both groups at 1 and 4 h p.i.

While the uptake of D10P in the liver and spleen was slightly elevated, its accumulation in the blood, lung, muscle, fat, and heart was comparable. However, as demonstrated in Figure 3.4, the desired *in vivo* stability was not achieved by this approach. Based on the HPLC analysis, the retention time of D10P metabolites were 3 and 11 min. Due to the lower uptake in the H2009 tumor, D10P showed significantly less tumor-to-muscle and tumor-to-lung ratios compared to 10PD.

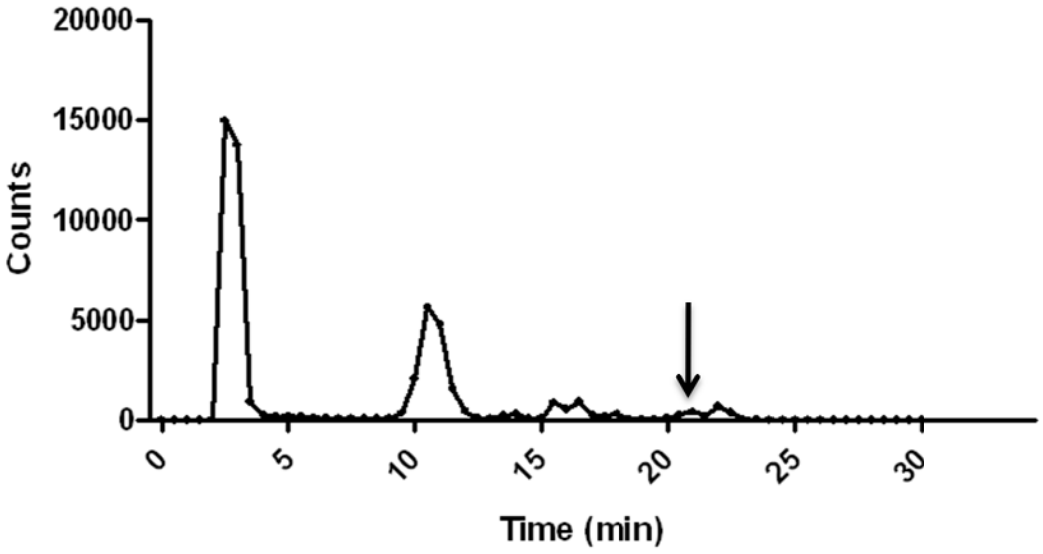

Figure 3.4 The HPLC analysis of metabolites of ^{111}In labeled D10P in mouse urine. The arrow indicates the retention time of the intact peptide conjugate, which differs from its metabolites.

The reduced renal accumulation of ^{111}In-DTPA-D-Phe^{1}-octreotide has been reported by blocking the cationic binding sites on renal proximal tubular cells with D- or L-lysine.[285, 286] This suggests that the electrostatic interaction between positively charged peptides and negatively charged surface of renal proximal tubular cells may be critical in the reabsorption of peptides into renal cells. Studies with radiolabeled antibody fragments

demonstrated that the kidney uptake can be reduced by lowering their isoelectric points through chemical modification.[287-289] As the 7-mer (RGDLATL) was resulted from the 10-mer (RGDLATLRQL) by removal of the three C-terminal amino acids, it is less positively charged. Given the fact that the 7-mer was found with similar $\alpha_v\beta_6$ binding affinity,[187] we proceeded with same biological evaluations as we did with 10PD in hope for a similar tumor uptake and much less renal accumulation. Indeed, dramatically reduced kidney uptake was observed for 7PD (1 h: 7PD: 6.83 ± 1.15 %ID/g; 10PD: 45.98 ± 10.28 %ID/g; p = 0.0001; 4 h: 7PD: 6.77 ± 1.28 %ID/g; 10PD: 50.69 ± 17.00 %ID/g; Table 3.7). However, the reduced tumor uptake of 7PD leads to less favorable tumor-to-background ratios compared to 10PD.

Table 3.7 Biodistribution of ^{111}In labeled 7PD and 10PD in the mice bearing H2009 xenograft at 1 and 4 h p.i. (7PD: n = 4; 10PD: n = 6). Data are presented as %ID/g ± s.d.

	7PD		10PD	
Tissue	1 h	4 h	1 h	4 h
blood	0.85 ± 0.18	0.23 ± 0.05	0.84 ± 0.47	0.28 ± 0.10
lung	0.83 ± 0.20	0.21 ± 0.03	0.88 ± 0.34	0.31 ± 0.08
liver	0.42 ± 0.09	0.29 ± 0.06	0.42 ± 0.15	0.36 ± 0.06
spleen	0.37 ± 0.07	0.22 ± 0.05	0.35 ± 0.15	0.26 ± 0.04
kidney**	6.83 ± 1.15	6.77 ± 1.28	45.89 ± 10.28	50.69 ± 17.00
muscle	0.17 ± 0.05	0.07 ± 0.03	0.24 ± 0.09	0.15 ± 0.10
fat	0.15 ± 0.05	0.05 ± 0.02	0.18 ± 0.21	0.11 ± 0.03
heart	0.55 ± 0.24	0.12 ± 0.02	0.35 ± 0.18	0.16 ± 0.04
tumor*	1.06 ±0.38	0.31 ± 0.06	1.99 ± 0.57	1.37 ± 0.31
tumor/muscle	5.61 ± 1.86	4.68 ± 1.53	8.85 ± 2.07	10.49 ± 3.62
tumor/lung	1.28 ± 0.30	1.51 ± 0.09	2.42 ± 0.60	4.58 ± 1.19

* indicates $p < 0.01$ between both groups at 1 and 4 h p.i.
** indicates $p < 0.001$ between both groups at 1 and 4 h p.i.

PEGylation has been reported as a valid method to prolong the blood circulation of the short peptides for drug delivery.[290] In general, it is believed that the tissue distribution of radiotracers can be improved by PEGylation. In order to verify this

hypothesis, the effects of PEGylation on biodistribution of our imaging probes were compared by D10P, D10C, D7P, and D7C in the H2009 tumor-bearing mice. Taken the tissue distribution profiles of D10P and D10C together (Table 3.8), the introduction of PEG chain significantly enhanced the uptake of all tissues throughout the studies.

Table 3.8 Biodistribution of ^{111}In labeled D10P and D10C in the mice bearing H2009 xenograft at 1 and 4 h p.i. (n = 4). Data are presented as %ID/g ± s.d.

	D10P		D10C	
Tissue	1 h	4 h	1 h	4 h
blood	1.10 ± 0.20	0.49 ± 0.05	0.37 ± 0.04	0.22 ± 0.02
lung	0.85 ± 0.21	0.46 ± 0.07	0.38 ± 0.05	0.23 ± 0.04
liver	0.85 ± 0.15	0.99 ± 0.04	0.33 ± 0.04	0.30 ± 0.02
spleen	0.69 ± 0.13	0.91 ± 0.21	0.26 ± 0.03	0.27 ± 0.03
kidney	7.30 ± 1.12	6.40 ± 0.99	4.98 ± 0.65	4.86 ± 0.61
muscle	0.26 ± 0.07	0.18 ± 0.02	0.09 ± 0.01	0.12 ± 0.02
fat	0.31 ± 0.13	0.25 ± 0.06	0.07 ± 0.02	0.10 ± 0.04
heart	0.48 ± 0.13	0.28 ± 0.05	0.23 ± 0.05	0.14 ± 0.03
tumor	1.04 ± 0.08	0.68 ± 0.07	0.63 ± 0.07	0.54 ± 0.02
tumor/muscle	3.99 ± 1.09	3.75 ± 0.67	7.26 ± 1.64	4.52 ± 0.76
tumor/lung	1.27 ± 0.22	1.52 ± 0.20	1.66 ± 0.27	2.26 ± 0.33

Table 3.9 Biodistribution of ^{111}In labeled D7P and D7C in the mice bearing H2009 xenograft at 1 and 4 h p.i. (n = 4). Data are presented as %ID/g ± s.d.

	D7P		D7C	
Tissue	1 h	4 h	1 h	4 h
blood	0.58 ± 0.08	0.51 ± 0.04	0.33 ± 0.11	0.34 ± 0.19
lung	0.60 ± 0.05	0.38 ± 0.03	0.51 ± 0.06	0.35 ± 0.04
liver	0.32 ± 0.03	1.38 ± 0.17	0.30 ± 0.06	0.32 ± 0.05
spleen	0.33 ± 0.05	0.79 ± 0.01	0.27 ± 0.08	0.37 ± 0.09
kidney	5.30 ± 0.44	4.42 ± 0.21	4.91 ± 1.19	3.95 ± 0.93
muscle	0.23 ± 0.09	0.13 ± 0.01	0.13 ± 0.04	0.12 ± 0.02
fat	0.15 ± 0.03	0.21 ± 0.11	0.08 ± 0.03	0.09 ± 0.04
heart	0.24 ± 0.04	0.27 ± 0.05	0.21 ± 0.03	0.17 ± 0.08
tumor	0.84 ± 0.12	0.86 ± 0.07	0.56 ± 0.13	0.50 ± 0.12
tumor/muscle	3.51 ± 1.09	6.69 ± 1.14	4.63 ± 1.11	5.00 ± 0.86
tumor/lung	1.30 ± 0.27	2.24 ± 0.24	1.08 ± 0.19	1.55 ± 0.29

On the other hand, while addition of the PEG chain increased the tumor uptake for D7P, only slightly elevated uptake were observed in the blood, liver, and spleen at 4 h p.i. (Table 3.9). Based on our biodistribution results, the significant enhancement of tumor-to-background ratios by PEGylation was not observed.

3.4 Discussion

Integrins are cell surface glycoproteins involved in cell-cell and cell- extracellular matrix interactions. The over expression of several types of integrins has been associated with many diseases including cancer. In particular, the expression of $\alpha_v\beta_6$ integrin is at low or undetectable levels on normal tissue but is up-regulated on many cancers including oral squamous cell carcinoma, breast cancer, and pancreatic cancer. Recently, the $\alpha_v\beta_6$ integrin has been identified as a biomarker of prognosis in colon and lung cancer.[176, 177, 179, 265, 291] The development of imaging probes that can target this receptor could therefore have a significant impact on patient diagnosis, care and management. Based on two truncated forms (7-mer and 10-mer) of a 20-mer peptide sequence selected by phage display, we designed, synthesized, and evaluated the peptide conjugates. Two major approaches have been ultilized to optimize our imaging probe design: PEGylation and site-specific DOTA conjugation.

The choice of ^{111}In as the radioisotope in this work was based on three reasons: i) ^{111}In has been used in many clinical procedures of SPECT and gamma scintigraphy in the forms of FDA-approved imaging agents, such as OctreoScan and ProstaScint; ii) ^{111}In is commercially available at a reasonable price. This is especially important because there is

no cyclotron facility on any of academic institutes in the Dallas-Fort Worth region; iii) in the early stage of this work, we were informed that a preclinical SPECT-CT system would be made available by the well-known Gulf-War Syndrome Project, although the effort was aborted due to unforeseeable reasons. To label the peptide constructs of choice with ^{111}In, we selected DOTA as a bifunctional chelator (BFC). To be used for *in vivo* imaging, the BFC-metal complex must be resistant to the *in vivo* metal transchelation and enzymatic degradation. This requires that the metal complex be stable not only thermodynamically but also kinetically. Recent reports have proven that the kinetic stability is more important for the *in vivo* imaging applications.[255] Therefore, DOTA was chosen instead of DTPA because of the thermodynamic and kinetic stability considerations. For DOTA conjugation, the conjugation step was undertaken in the solution phase after the peptide synthesis and purification. In order to conjugate peptides at C-terminus, a Cys was introduced to the end of PEG in order to use the well-established thiol-maleimide coupling reaction. To attach DOTA to the peptide constructs at N-terminus, we used DOTA-tris(t-Bu ester) as a starting material. Although the low aqueous solubility and the need of deprotection after conjugation make it unsuitable for protein modifications,[282] DOTA-tris(t-Bu ester) is ideal for conjugating peptides with DOTA in non-aqueous solvents.

It has been reported that PEGylation of peptide constructs can prolong their circulation and decrease proteolysis.[290, 292-295] To apply the well-established PEGylation methodology to our imaging probe design, we first prepared 10PD and compared its biological behavior and targeting properties in tumor-bearing mice. As we expected, the

H2009 ($\alpha_v\beta_6^+$) tumor uptake of ^{111}In-10PD was significantly ($p = 0.0003$) higher than that of H460 ($\alpha_v\beta_6^-$) tumor at 4 h p.i. In order to verify our findings, we performed the biodistribution studies of S10PD, where the peptide conjugate has the same amino acid composition as 10PD but with different peptide sequence. Compared to 10PD, the H2009 tumor uptake of S10PD was significantly ($p < 0.05$) reduced throughout the study. Interestingly, the accumulation of 10PD in the H460 tumor and S10PD in the H2009 tumor was comparable, which further validate the potential of 10PD as specific $\alpha_v\beta_6$ imaging probe. However, high kidney uptake was observed throughout the study, which may due to the fact that our peptides are below the renal filtration limit and reabsorbed in the proximal tubular cells.[296, 297] As there was no $\alpha_v\beta_6$ integrin in the kidney detected by immunohistological staining, we believe the high kidney uptake is due in part to the peptide degradation products or polar nature of the peptide.

Because the stability of an imaging probe against the enzymatic degradation may correlate to its biodistribution profile, we capped the peptide constructs with DOTA and PEG chain at both ends in hope to obtain a desired *in vivo* stability and overall tissue distribution results. Although the biodistribution results indicate that the kidney uptake can be dramatically reduced by using this approach, the improved *in vivo* stability was not achieved as revealed from the urine metabolism profiles of D10P and 10PD. Since each peptide metabolite may reveal different biodistribution profile, this finding reflects that the ^{111}In-chelated peptide metabolites of D10P have less tendency in renal accumulation.

Previous research indicates that positively charged peptide metabolites are tend to be trapped in the lysosomes and cause high renal accumulation.[298, 299] The peptides with more positive net charges (e.g. ^{111}In labeled DTPA-octreotide) have been reported highly accumulated in the kidneys. Previous studies identified the megalin/cubilin system as an essential component in the renal reabsorption of radiolabeled peptides. [285, 286] Megalin is a scavenger receptor for the endocytosis of acidic proteins and peptides in the proximal tubules of the kidney. Therefore, a reduced peptide net charge is likely to have reduced kidney accumulation. Indeed, our biodistribution of 7PD showed a significant (p = 0.0001) reduction in kidney uptake. However, it should be noted that the H2009 tumor uptake was also greatly reduced with the removal of the last 3 amino acids at 4 h p.i. By phage blocking assays, the 10-mer and 7-mer peptides have the same binding affinity to H2009 cells.[187] This result suggests that there are parameters that affect the specific tumor uptake of 7PD. Taken together, the high kidney uptake of 10PD can be alleviated by changing the labeling position and reduce the peptide net charge. However, 10PD was still evaluated as the best peptide conjugate to image the $\alpha_v\beta_6$ integrin due to its higher tumor uptake.

3.5 Conclusion

The peptide constructs derived from phage display library have been evaluated to image the $\alpha_v\beta_6$-positive tumors. In this work, six ^{111}In labeled peptide conjugates were used for *in vivo* evaluation of the effects of PEGylation and site-specific DOTA conjugation. As expected, the preferential uptake in the H2009 ($\alpha_v\beta_6^+$) tumor was

observed in all peptide conjugates and PEGylation can enhance the tumor uptake by prolonging blood retention time of the peptides. Despite 10PD showed the best tumor-to-background ratios, its unexpected high and persistent levels of radioactivity in the kidneys was also observed. This phenomenon can be alleviated by conjugating DOTA at the N-terminus or using the peptide constructs with less net positive charges.

CHAPTER FOUR

TARGETING THE GLP-1R FOR IMAGING THE PANCREATIC BETA CELL

4.1 Introduction

Noninvasive assessment of pancreatic β-cell mass (BCM) is a challenge for any imaging modality due to scarce and scattered distribution of β-cells within the pancreas. The islets of Langerhans contributes 1-2% of the pancreas mass, in which 65-80% of the cells are β-cells.[188] To date, it has been well-accepted that the BCM changes reflect the progression of diabetes in both T1D and T2D.[188] Therefore, developing an accurate and reproducible imaging technique to longitudinally measure BCM is of great importance clinically and scientifically.[300]

Strategies based on monoclonal antibodies,[301-304] glucose derivates,[305-313] ligands for sulfonylurea receptor 1,[314-318] neurofunctional imaging agents,[217, 219, 221, 319-325] and peptides isolated from phage display [216, 326] have been used to develop nuclear imaging probes for BCM monitoring. Among them, ^{11}C or ^{18}F labeled dihydrotetrabenazine (DTBZ) derivatives that target the vesicular monoamine transporter type 2 (VMAT-2) are currently the most successful ones for visualizing the BCM *in vivo*. However, because VMAT2 is not exclusively expressed on β-cells [222, 223] and recent clinical studies based on (+)-[^{11}C]-DTBZ are relatively disappointing,[224] radiotracer development based on the other approach is warranted.

In this part of my work, the glucagon-like peptide 1 (GLP-1) analogs were used to target GLP-1 receptors (GLP-1R). GLP-1 is an insulinotropic peptide hormone secreted

by intestinal L-cells in response to nutrient ingestion.[132] While GLP-1 is synthesized in the forms of GLP-1(7-36)-NH_2 and GLP-1(7-37), GLP-1(7-36)-NH_2 is the major bioactive form and considered as an endogenous ligand to GLP-1R.[132] One of its most important biological functions is to enhance insulin biosynthesis and secretion.[132] However, it is important to note that insulin secretion is directly triggered by glucose instead of GLP-1.[132, 327]

The GLP-1R belongs to family B of G protein-coupled receptors [132] and was originally isolated from the cDNA library of rat pancreatic islets.[328] The expression of GLP-1R has been majorly observed on the pancreatic β-cells and to less extent on the stomach, lung, brain, kidney, pituitary gland, and small intestine. No GLP-1R on the liver, adipose, and skeletal muscle has been reported.[132] Although previous studies indicated that the presence of GLP-1R mRNA is on α, β, and δ cells in pancreatic islets,[329, 330] the expression of GLP-1R was found exclusively on β-cells and pancreatic ducts in a recent report.[133] The internalization of GLP-1R occurs when it binds with GLP-1, and the rate depends on phosphorylation of particular residues at the C-terminus of GLP-1R.[331, 332] Given the fact that the kinetic of the internalized GLP-1R cycles back to the membrane rapidly ($t_{1/2}$ ~15 min), the internalization process does not lead to the desensitization of the receptor.[331, 332] As such, it would be feasible to image GLP-1R by GLP-1 analogs.

Because GLP-1R is directly involved in the functional β-cells, it appears to be a suitable target for BCM imaging. Indeed, exendin-4, a GLP-1 analog found in the venom of Gilamonsters and shares 53% homology with GLP-1,[333] has been labeled with ^{111}In

and applied for pancreas as well as insulinoma imaging.[134, 225, 334, 335] Gotthardt et al. performed biodistribution studies in normal mice and rats that consisted of injecting ^{111}In-DTPA-Ahx-Lys^{40}-exendin-4.[225] An experiment that consisted of co-injection of exendin-4 was also performed. Although the uptake was observed in the pancreas, stomach, lung, and spleen, the SPECT imaging confirmed high uptake of ^{111}In-DTPA-Ahx-Lys^{40}-exendin-4 in the mouse pancreas. Wild et al. extended the studies by using Rip1Tag2 mice with spontaneous insulinoma development.[134] The highest uptake was found in the tumor at 4 h after injection of ^{111}In-DTPA-Ahx-Lys^{40}-exendin-4, and these tumors (1-3.2 mm) were further revealed by the SPECT imaging.

Other than exendin-4, there are considerable interests in developing GLP-1 analogs for BCM imaging. Because GLP-1 is highly susceptible to dipeptidyl peptidase-IV (DPP-IV) and neutral endopeptidase (NEP) 24.11, there are several challenges to rational design GLP-1 analogs.[336] DPP-IV is a serine protease that cleaves a single site in GLP-1 (Ala^8-Glu^9). It is found in numerous tissues and also exists as a soluble circulating form in plasma.[337] The degradation of GLP-1 by DPP-IV results in GLP-1 (9-36)-NH_2. Compared to GLP-1, the binding affinity of the metabolite GLP-1(9-36)-NH_2 is 60-fold reduced to GLP-1R.[338] On the other hand, NEP 24.11 is a widespread membrane-bound zinc metallopeptidase. NEP 24.11 cleaves multiple bonds between Asp^{15}-Val^{16}, Ser^{18}-Tyr^{19}, Tyr^{19}-Leu^{20}, Glu^{27}-Phe^{28}, Phe^{28}-Ile^{29}, and Trp^{31}-Leu^{32}.[339] Although the degradation of GLP-1 by DPP-IV can be prevented by using DPP-IV inhibitors or replacing Ala^8 with other Ala analogs, fewer studies have been carried out for NEP 24.11. To explore GLP-1

analog for noninvasive imaging of BCM, it is desired to have high enzyme stability without sacrificing the binding affinity to GLP-1R.

Dr. Jung-Mo Ahn's Laboratory (Department of Chemistry, University of Texas at Dallas) has synthesized a series of GLP-1 analogs containing lactam bridges between Lys^{i} and Glu^{i+4} to elucidate the receptor-bound conformation of GLP-1.[340] The presence and location of the two **α**-helices between residues 13-20 and 24-35 that were shown by 2D-NMR studies of GLP-1 [341] was recently confirmed by cyclization scan.[340] Based on these findings, two highly potent GLP-1 analogs ([D-Ala^{8}]-c[Glu^{22},Lys^{26}]-c[Lys^{30},Glu^{34}]GLP-1(7-36)-NH_2, EM2196; [D-Ala^{8}]-c[Glu^{18},Lys^{22}]-c[Lys^{30},Glu^{34}]GLP-1(7-36)-NH_2, EM2198) with two lactam bridges introduced at the N- and C-terminal regions were designed. The two lactam bridges were aimed to simultaneously stabilize the two α-helical regions of GLP-1 and increase receptor binding affinity. Furthermore, L-Ala at their 8^{th} position was replaced with D-Ala to prevent the degradation by DPP-IV.

The main objective of this part of my work was to synthesize and evaluate the conjugates of the rationally designed GLP-1 analogs for BCM imaging when labeled with ^{64}Cu ($t_{1/2}$: 12.7 h, 19% β^{+}). All peptide constructs were synthesized with C-terminal modification of Cys to facilitate the DOTA conjugation by standard thiol-maleimide reactions. A 6-aminohexanoic acid (Ahx) was used as a spacer between a peptide and DOTA. As exendin-4 is a well recognized agonist of GLP-1R, its biological evaluations were also performed for comparison.

4.2 Materials and Methods

General

All reagents and solvents were purchased from Sigma-Aldrich (St. Louis, MO) and used as received unless otherwise noted. N^{α}-Fmoc protected amino acids, aminomethylated polystyrene resin and Rink amide linker were purchased from EMD Chemicals (Gibbstown, NJ) and Senn Chemicals (Dielsdorf, Switzerland). All amino acids used were of *L*-configuration unless otherwise stated. Recombinant human dipeptidyl peptidase-IV, recombinant human neprilysin (neutral endopeptidase 24.11, EC 3.4.24.11) were purchased from R&D Systems (Minneapolis, MN). Milli-Q water (18 MΩ-cm) was obtained from a Millipore Gradient Milli-Q water system (Billerica, MA). Low adhesion vials and C_{18} Sep-Pak cartridges were purchased from USA Scientific (Ocala, FL) and Millipore (Billerica, MA), respectively. The C_{18} Sep-Pak cartridge was activated with ethanol and water before use. Nitric acid (10 – 20%) used for the acid wash was prepared by diluting 70% nitric acid with Milli-Q water. The ammonium acetate buffer (0.1 M, pH 6.5) was pretreated with Chelex 100 resin (Bio-Rad, Hercules, CA) before use. ^{64}Cu ($^{64}CuCl_2$ in 0.05N HCl) was purchased from University of Wisconsin–Madison (Madison, WI) with radionuclidic purity ≥ 99.90%. Reverse-phase high performance liquid chromatography (RP-HPLC) was performed on either an Agilent 1100 series with a diode-array UV detector or a Waters 600E chromatography system with a Waters 2996 photodiode array detector and a Shell Jr. 1000/2000 single-channel radiation detector.

The molecular mass of the peptides and their DOTA-conjugates were confirmed by either ESI-MS (LCQ Deca XP Plus ESI-ion trap mass spectrometer, Thermo Electron Corporation, West Palm Beach FL) or MALDI-TOF (Voyager-DE™ PRO Biospectrometry Workstation, Applied Biosystems, Foster City, CA). Small animal PET-CT imaging studies were performed on a Siemens Inveon PET-CT Multimodality System (Siemens Medical Solutions Inc., Knoxville, TN)

4.2.1 Peptide Synthesis (Scheme 4.1)

Scheme 4.1 Chemical synthesis of the GLP-1 analogs (courtesy of Dr. Ahn)

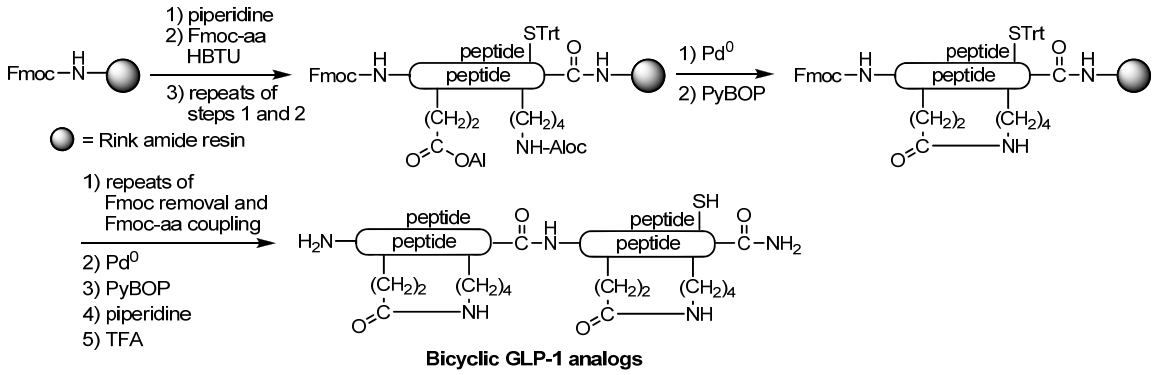

All of the GLP-1 analogs were synthesized manually using standard *N*-Fmoc/^{t}Bu solid-phase peptide synthesis protocol as described previously.[340, 342] Aminomethylated polystyrene resin (0.25 mmol, 0.4 mmol/g) was swollen in DMF for 10 min and washed with DMF (3 × 1 min). Fmoc-Rink amide linker (203 mg, 1.5 equiv),[343] HBTU (379 mg, 4 equiv), HOBt (135 mg, 4 equiv) and DIEA (0.35 mL, 8 equiv) were dissolved in DMF (3 mL). Then, the solution was added to the resin and shaken for 2 h. The coupling reaction was followed by Kaiser ninhydrin and TNBS tests,[344, 345] and unreacted amines were capped by using acetic anhydride (0.5 mL, 20 equiv) in DMF (3 mL) for 30 min. The Fmoc protecting group of the Rink amide linker was removed by treating with

piperidine (20% in DMF, 1 × 5 min and 1 × 30 min), and washed with DMF (3 × 1 min). The first amino acid was introduced by using a preactivated Fmoc-amino acid that was prepared by mixing a Fmoc-amino acid (4 equiv), HBTU (4 equiv), HOBt (4 equiv), and DIEA (8 equiv) in DMF (3 mL) for 30 min. The coupling reaction was carried out for 2-4 h or until Kaiser ninhydrin and TNBS tests became negative. When a coupling reaction was found to be incomplete, the resin was washed with DMF (3 × 1 min) and the amino acid was coupled again with a freshly prepared preactivated Fmoc-amino acid. When the second coupling reaction did not result in negative Kaiser ninhydrin and TNBS tests, the resin was washed with DMF (3 × 1 min) and the unreacted amines were capped by treating with acetic anhydride (20 equiv) in DMF for 5-10 min. These steps (removal of a Fmoc group and coupling of a Fmoc-amino acid) were repeated until all amino acids in the sequence of a peptide were coupled. Then, the resin was washed with DCM (5 × 1 min) and dried under vacuum. A growing peptide was frequently characterized by cleaving a small amount of resin and analyzing the released peptide with RP-HPLC and ESI-MS.

For the selective removal of allyl protecting groups of Lys and Glu, a fully protected peptide still bound on resin (0.25 mmol), was placed in a 12 mL-polypropylene reaction vessel. The reaction vessel was then sealed with a rubber septum and flushed with nitrogen for 10 min. To the vessel, $Pd(PPh_3)_4$ (30 mg, 0.1 equiv), and *N*,*N'*-dimethylbarbituric acid (390 mg, 10 equiv) dissolved in degassed DCM/DMF (4 mL, 3:1) was delivered by a syringe and the reaction mixture was kept under nitrogen for 30 min with occasional shaking. The resin was washed with LiCl/DMF (0.8 M, 3 × 1 min) and

the reaction was repeated again. Then, the resin was treated with PyBOP/HOBt/DIEA (6, 6, and 12 equiv) or BOP/HOBt/DIEA (6, 6, and 12 equiv) dissolved in DCM/DMF/NMP (1:1:1, 1% Triton X100) for 6-8 h until the reaction was complete. The resin was washed with DMF (3 × 1 min).

For the synthesis of a GLP-1 analogue containing two lactam bridges, a partially completed GLP-1 analogue (residues 30-36) was first constructed on Rink amide resin by following the synthetic procedures described above. After the selective removal of the allyl protecting groups on Lys(Aloc)^{30} and Glu(OAl)^{35}, the *C*-terminal lactam bridge was created with PyBOP. Then, the peptide was grown up to the position of the *N*-terminal lactam bridge, and another selective removal of the allyl groups on Lys(Aloc) and Glu(OAl) was carried out followed by the formation of the *N*-terminal lactam bridge (Scheme 1A). Then, the remaining amino acids were coupled to complete the synthesis of a bicyclic GLP-1 analogue.

A cleavage mixture of trifluoroacetic acid (TFA), dimethylsulfide, 1,2-ethanedithiol, and anisole (20 mL, 36:1:1:2) was added to a peptide on dried resin (0.25 mmol) in a disposable 50 mL-polypropylene tube, and the mixture was stirred for 90 min at room temperature in the dark. Then, the TFA solution was filtered, and the resin was washed with TFA (2 mL) and DCM (2 mL). The combined TFA solution was concentrated to a volume of approximately 3 mL with a gentle stream of nitrogen, and the peptide was precipitated with cold diethyl ether (40 mL). The precipitated peptide was centrifuged and the ether solution was decanted to remove the scavengers. Washing with

cold diethyl ether was repeated and the precipitated peptide was centrifuged, decanted and dried under vacuum.

To monitor the progress of peptide synthesis, a small amount of resin (approximately 20 mg) was collected and treated with the cleavage mixture (2 mL) for 90 min at room temperature in the dark. The TFA solution was filtered and concentrated to a volume of approximately 0.5 mL with a gentle stream of nitrogen. The peptide was precipitated with cold ether (10 mL) and the centrifuged peptide was washed with ether again. The peptide was dried under vacuum followed by HPLC and ESI-MS analysis.

A crude peptide was dissolved in 50% aqueous acetic acid and the insoluble was removed by centrifugation. The acetic acid solution containing peptide was purified with HPLC by using a reverse-phase semi-preparative Vydac column (C_4-bonded, 214TP1010, 10 × 250 mm, 10 μm) with gradient elution at a flow rate of 3.0 mL/min. A fraction containing the peptide was collected and lyophilized. The purity of all of the synthesized peptides was checked by analytical HPLC and found to be higher than 95%. The molecular mass of the purified peptides was confirmed by ESI-MS.

4.2.2 Determination of Enzyme Stability

A GLP-1 analogue (100 μM) was incubated with recombinant human DPP-IV enzyme (0.2 ng/mL) in Tris buffer (25 mM, pH 8.0) at 37°C.[346] At 0, 2, 4, 6, 9, and 24 h after the incubation, an aliquot of the solution (100 μL) was quenched with aqueous TFA (10%, 20 μL) and analyzed with RP-HPLC (elution gradient, 10-90% ACN in aqueous trifluoroacetic acid (0.1%) over 40 min, C_{18}-bonded column, Zorbax C-18, 4.6 × 250 mm). Similarly, these GLP-1 analogs (100 μM) were incubated with recombinant human

NEP 24.11 enzyme (1.0 μg/mL) in HEPES buffer (50 mM, pH 7.4, 50 mM NaCl) at 37°C.[347] At 0, 2, 4, 6, 9, 24, and 96 h after the incubation, an aliquot of the solution (100 μL) was quenched with aqueous TFA (10%, 20 μL) and analyzed with RP-HPLC.

4.2.3 DOTA-Peptide Conjugation (Scheme 4.2)

Scheme 4.2 Preparation of the DOTA-peptide conjugates (Ahx: 6-aminohexanoic acid)

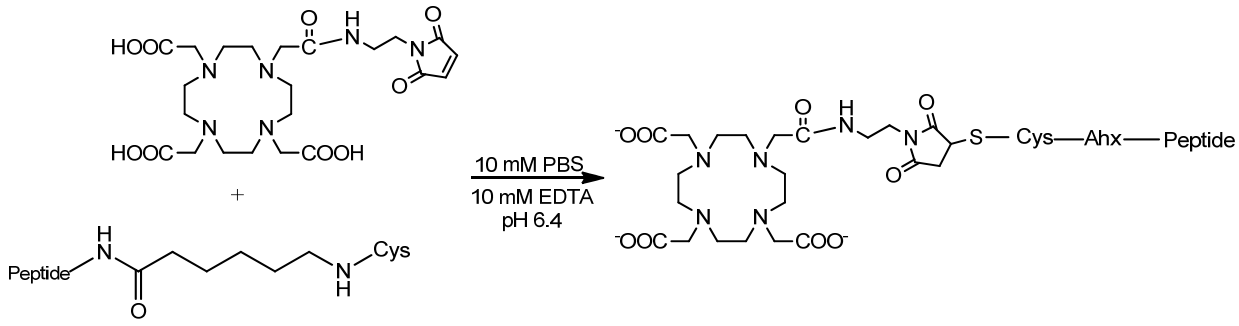

The peptide conjugation with DOTA was achieved by reacting the peptide construct with a C-terminal Cys (0.5 μmol) with maleimidomono-amide-DOTA (Macrocyclics, TX) (2.5 μmol; molar ratio: 5:1) in 10 mM PBS (pH 6.4, containing 10 mM EDTA) for 2 h at room temperature (RT). The DOTA-peptide conjugates were purified by HPLC with a Waters XTerra C_{18} column (5 μm, 4.6 mm × 150 mm). The flow rate was set at 1 mL/min using a gradient system starting from 80% solvent A by a linear ramp to 100% solvent B at 40 min. Solvent A: 0.1% trifluoroacetic acid (TFA) in water (v/v); solvent B: 0.1% TFA in acetonitrile (v/v). The purified fractions were characterized by MALDI-MS with α-cyano-4-hydroxycinnamic acid (Table 4.1).

Table 4.1. MALDI-MS characterization of the DOTA conjugates of GLP-1 analogs

Peptide Conjugate	Molecular Formula	M.W. (Calculated)	M.W. (Determined)
GLP-1-DOTA	$C_{180}H_{276}N_{48}O_{56}S$	4040.55	4040.60
[D-Ala^8]GLP-1-DOTA	$C_{180}H_{276}N_{48}O_{56}S$	4040.55	4039.80
EM2196-DOTA	$C_{185}H_{278}N_{48}O_{58}S$	4134.62	4135.50
EM2198-DOTA	$C_{188}H_{285}N_{49}O_{57}S$	4175.72	4175.70
Exendin-4-DOTA	$C_{215}H_{332}N_{58}O_{71}S_2$	4929.51	4929.30

4.2.4 Radiochemistry

Aliquots of the peptide conjugate was dissolved with 50 μL of 0.4 M ammonium acetate (pH 6.5) followed by addition of $^{64}CuCl_2$ (10 μL, 1.5-2.3 mCi). The reaction mixtures were incubated at 37°C for 1 h in an Eppendorf thermomixer at a constant shaking rate of 600 rpm. After adding 5 μL of DTPA (5 mM) to challenge the nonspecifically bound ^{64}Cu, the labeled peptide was purified by a pre-activated C_{18} Sep-Pak cartridge. The HPLC analysis (gradient elution, 20-80% ACN in aqueous trifluoroacetic acid (0.1%) over 30 min, Protein & Peptide C_{18} column, VyDac, 4.6 × 250 mm) was performed to determine radiochemical the purity of each ^{64}Cu labeled peptide conjugate. The specific activity was calculated as the ratio of [(amount of the added radioactivity) × (radiolabeling efficiency determined by radio-TLC)] / (amount of the added peptide conjugate).

4.2.5 Receptor Binding Assays

GLP-1R binding affinities of the five DOTA-peptide conjugates were determined by competitive binding assays with ^{125}I-exendin-4(9-39) as a radioligand (Perkin Elmer, Waltham, MA). Experiments were performed on 24-well plates seeded with INS-1 832/13 rat insulinoma cells (5×10^5 cells/well). The cells were rinsed with 10 mM phosphate buffered saline (PBS) containing 0.1% of bovine serum albumin (BSA), followed by the addition of ^{125}I-exendin-4(9-39) solutions (~15,000 cpm/well) mixed with the peptide conjugates at 0-1000 nM. After incubation at 37°C for 1 h, the cells were rinsed 3 times with 10 mM PBS and lysed with 1N NaOH. The cell lysate was collected

and counted by a γ-counter. The cell uptake of ^{125}I-exendin-4(9-39) was normalized in terms of added radioactivity and seeded cell number. The IC_{50} values were calculated by fitting the quadruplicate data with nonlinear regression using Graph-Pad Prism (GraphPad Software, La Jolla, CA).

4.2.6 Preparation of Albumin Fragments

The albumin fragments was prepared by using a published procedure.[299] Intact bovine serum albumin (4.5 g) was trypsinized by a solution containing 500 mg of trypsin in 15 mL of ammonium carbonate buffer (50 mM, pH 7.8) at 37°C for 24 h. The solution of trypsinized albumin was further purified by Centricon YM-50 (M.W. cut off: 50 KDa). The filtrate was collected and stored at 4^{o}C.

4.2.7 Streptozotocin-induced Diabetic Mouse Model

All animal studies were performed in compliance with guidelines set by the UT Southwestern Institutional Animal Care and Use Committee. The protocol to develop a STZ-induced diabetic mouse model was performed according to a published report.[348] The streptozotocin (STZ) solution was freshly prepared by dissolving STZ powder in 10 mM sodium citrate buffer (pH 9.5) to produce a final concentration of 10mg/mL. Normal male BALB/c mice at the age of 6-8 weeks (n = 6; body weight: 20-25 g) were fasted overnight followed by intraperitoneal injection of the STZ solution at 60 mg/kg. The treatment was continued in five consecutive days with mouse chow provided. After one week of the STZ treatment, all the mice appeared diabetic and the mice with a non-fasting blood glucose level above 280 mg/dl (monitored by ACCU-CHECK Aviva meter) were selected for the *in vivo* studies.

4.2.8 Imaging Scans

In Vivo Imaging Studies

Both normal and STZ-induced diabetic male BALB/c mice were used for the imaging studies. All animals were fasted overnight prior to imaging. Each BALB/c mouse was anesthetized initially using 3% isoflurane in 3.0 L/min oxygen in an acrylic induction chamber. When fully sedated, the animal was placed on the scanner bed with a nose cone to maintain anesthesia at 2% isoflurane in 3.0 L/min oxygen. The CT data was acquired at 80kV and 500 μA with a focal spot of 58 μm. The total rotation of the gantry was 360^{o} with 360 rotation steps obtained at an exposure time of approximately 200 ms/frame. The images were attained using a CCD readout of 4096 × 3098 with a bin factor of 4 and an average frame of 1. Under low magnification the effective pixel size was 103.03 μm. The total CT acquisition time was approximately 6 min. The PET acquisition was performed directly following the CT after injecting 90-110 μCi of a ^{64}Cu labeled GLP-1 conjugate (volume ~ 0.1 mL) into the tail vein. Dynamic PET scans were acquired for 1 h immediately after the tracer injection, followed by static scans at 2 and 4 h p.i. CT images were reconstructed using Cobra reconstruction software at a downsample of two. Dynamic PET images were histogramed into 12 frames (1 frame/300 s) and the resulting sinogram was reconstructed using OSEM3D (3-Dimensional Ordered Subsets Expectation Maximization). Regions of interest (ROIs) were drawn, guided by a detailed mouse atlas.[349] Visual analysis was performed using coronal, transverse, and sagittal planes, where ROIs were drawn over the pancreas as well

as other organs or tissues. The tissues examined include the liver, kidneys, and pancreas. The resulting quantitative data were expressed as percent injected dose per gram of tissue (%ID/g) and specific binding index (SBI). The SBI is defined as SBI = $(C_P - C_L)/C_L$, where C_P represents the signal intensity from the pancreas, and C_L represents the signal intensity from non-specific uptake. Because there is no expression of GLP-1R in the liver [132, 133], we selected the liver uptake as C_L.

Ex Vivo Imaging Studies

The *ex vivo* microPET/CT scans were performed by using normal and STZ-induced diabetic mice. Each mouse received 100 μCi of ^{64}Cu-EM2198 intravenously and sacrificed without perfusion at 1 h p.i. The liver, spleen, stomach, intestines, and pancreas were excised and imaged with 6 min of CT acquisition followed by 15 min of PET imaging. The imaging reconstruction and quantification methods were the same as above.

4.2.9 *In Vivo* Blood and Kidney Metabolism Studies

Normal mice were injected with 50-100 μCi of a ^{64}Cu labeled GLP-1 conjugate via the tail vein. At 1 h and 4 h p.i., the mice were sacrificed under anesthesia. The blood and kidneys were ice bathed and homogenized in 80% ethanol (2 mL) by homogenizer. The samples were centrifuged at 2,000g for 5 min. The supernatants were collected, filtered, and analyzed by radio-HPLC as described in Radiochemistry section.

4.2.10 Histology Examination

The pancreas tissue sections (5 μm) used for routine hematoxylin and eosin (H&E) and immunohistological staining were prepared by the Histology Core at UT Southwestern Medical Center. Images of H&E staining were acquired by Olympus

confocal microscope (Center Valley, PA). For immunohistological staining, methods were as follows: Sections were deparaffinized using EZ DeWax solution (Biogenex, San Ramon, CA) twice for 5 min and washed by milliQ water. The sections were then covered by sodium dodecylsulphate solution (SDS, 1%, w/v) for 5 min. Blocking was done for 1 h at room temperature with Tris buffered saline (TBS) containing 2% BSA. Primary (1:100 rabbit polyclonal anti-GLP-1R (Abcam, Cambridge, MA); 1:50 rabbit polyclonal anti-insulin and anti-glucagon antibodies (Abcam, Cambridge, MA)) and secondary antibodies (1:100 fluorescein isothiocyanate-conjugated goat anti-rabbit immunoglobulin antibody (Jackson ImmunoResearch Laboratories)) were diluted in TBS with 2% BSA. Both antibodies were separately incubated for 1 h at room temperature. Excess antibody was removed with serial washing with TBS. A 1:5,000 dilution of Hoechst Dye #33342 (Molecular Probes, Eugene, OR) was used to stain the nuclei. Tissue samples were covered with Vectashield (Vector Laboratories, Burlingame, CA). Tissue slides were evaluated and photographed via fluorescent microscopy on an Eclipse TE2000 fluorescent microscope (Nikon, Melville, NY) equipped with a CoolSNAP$_{fx}$ camera (Roper Scientific, Tuscon, AZ). Images were captured using MetaVue v4.6r9 (Universal Imaging, Downington, PA) acquisition and analysis software.

4.2.11 Statistic Analysis

Quantitative data were processed by Prism 5 (GraphPad Software, La Jolla, CA) and expressed as Mean ± SD. All analyses were performed by one-way analysis of variance and Student's t test. P values < 0.05 were considered statistic significant.

4.3 Results

4.3.1 Peptide Synthesis and Enzyme Stability

All of the GLP-1 analogs used in this study were prepared by following a standard solid-phase peptide synthesis protocol with N^{α}-Fmoc/^{t}Bu protecting group strategy. The bicyclic peptides, EM2196 and EM2198, were designed to have two lactam bridges in different regions of GLP-1. The installation of the lactam bridges was carried out on the resin for synthetic convenience. The side chains of the glutamic acids and lysines that were employed to form the lactam bridges were orthogonally protected with allyl protecting groups. After construction of a partial sequence on the resin, the allyl protecting groups of Glu and Lys were removed with Pd^{0} and a lactam bridge was formed with a coupling reagent. The syntheses of EM2196 and EM2198 were completed by repeating these steps. Completely synthesized peptides were cleaved and fully deprotected by treating TFA, followed by purification with RP-HPLC. The purified peptides showed > 95% purity and confirmed by ESI-MS.

Enzymatic resistance to DPP-IV and NEP 24.11 of the GLP-1 analogs was evaluated by incubating with recombinant human DPP-IV and NEP 24.11. GLP-1 was found to be degraded by DPP-IV after 3 h incubation. In contrast, [D-Ala^{8}]GLP-1 was completely stable against DPP-IV, showing no cleavage up to 24 h (Figure 4.1).

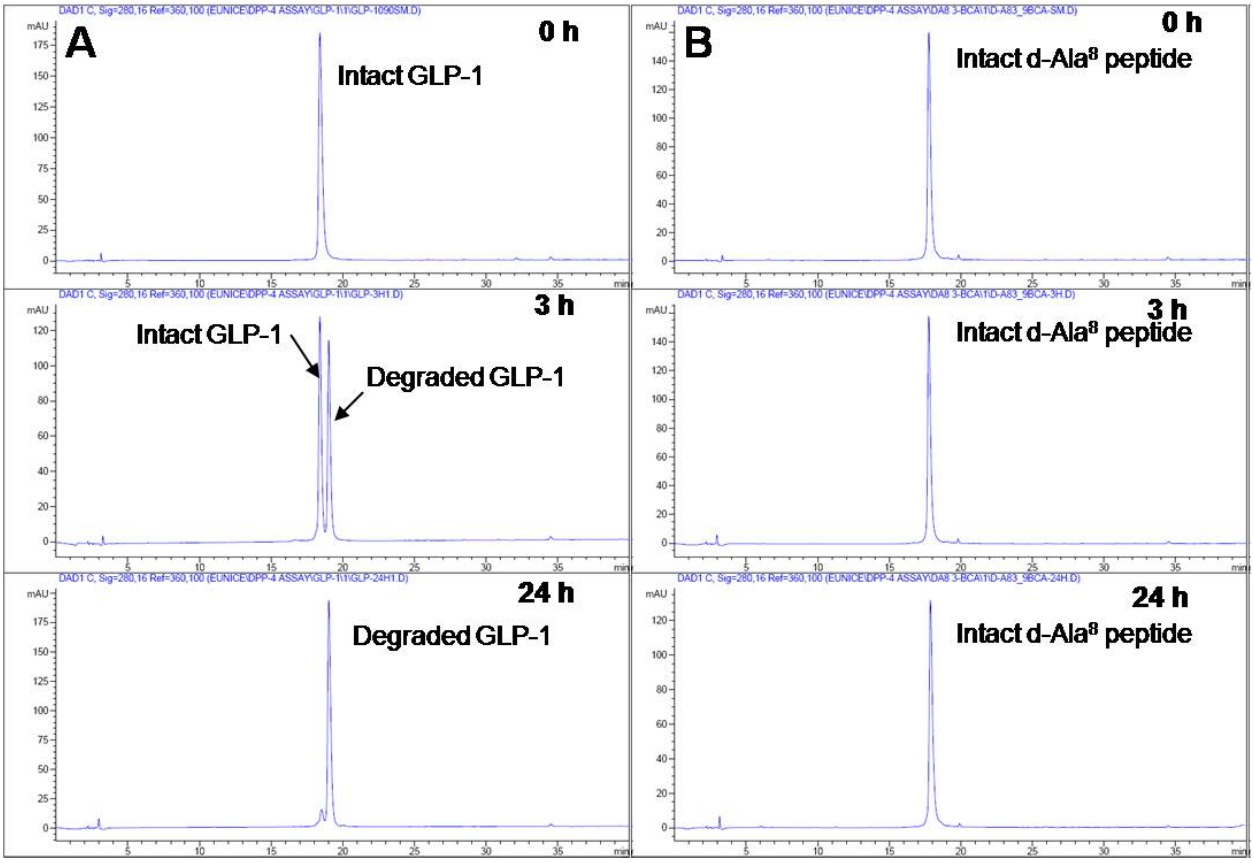

Figure 4.1 *In vitro* stability of the GLP-1 analogs against DPP-IV enzyme. HPLC chromatograms of (A) GLP-1 and (B) EM2198 after 0, 3, and 24 h incubation with DPP-4. The peptides with a concentration of 100 μM were incubated with 0.2 ng/mL DPP4 at 37 ^{o}C in 25 mM Tris-HCl (pH 8.0), followed by HPLC analysis (courtesy of Dr. Ahn) .

On the other hand, EM2198 remained > 90% intact even after 24 h incubation with NEP 24.11, whereas > 50% of GLP-1 was found to be degraded at 4 h after the incubation (Figure 4.2). This outstanding stability to NEP 24.11 is likely resulted from the shielding effects of the two lactam bridges that block the enzyme recognition.

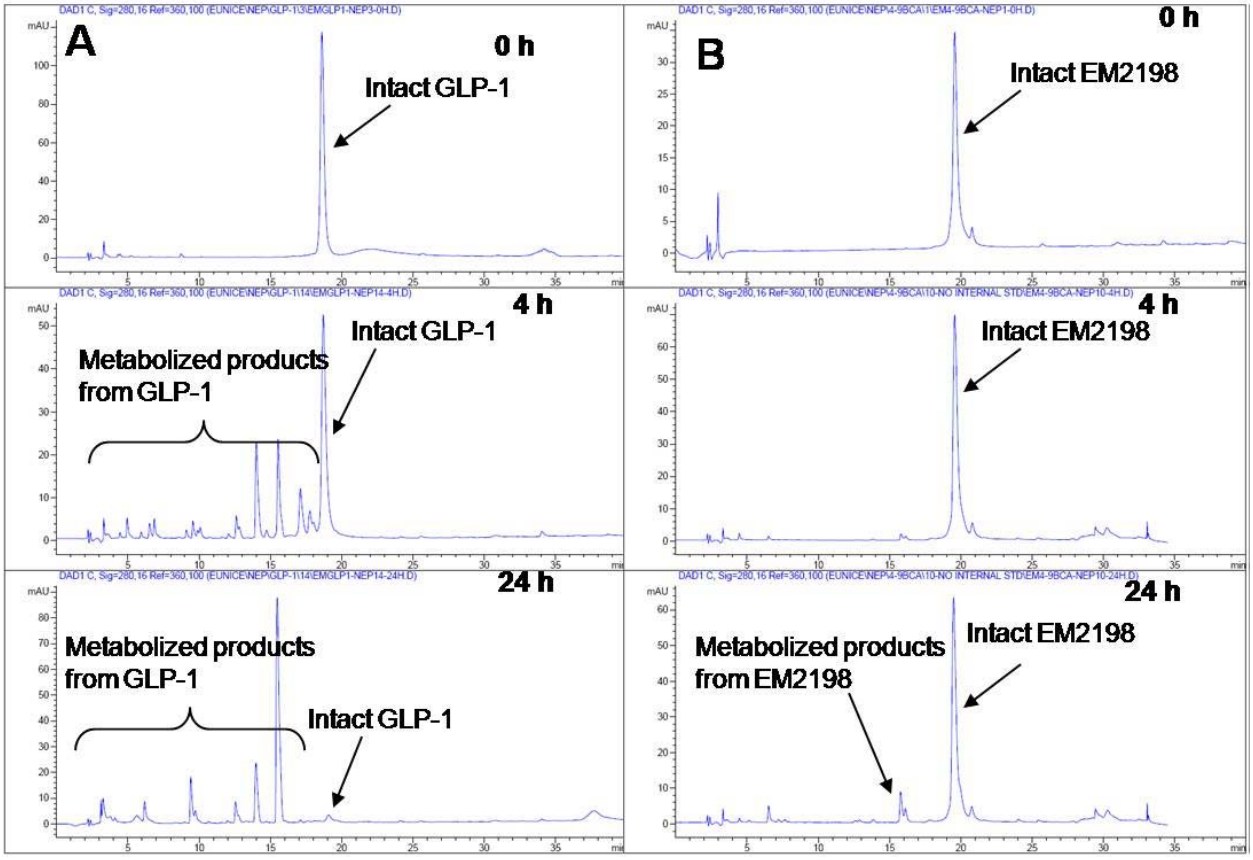

Figure 4.2. *In vitro* stability of the GLP-1 analogs against NEP 24.11 enzyme. HPLC chromatograms of (A) GLP-1 and (B) EM2198 after 0, 4, and 24 h incubation with NEP 24.11. The peptides with a concentration of 100 μM were incubated with 1.0 μg/mL NEP 24.11 at 37 ^{o}C in 50 mM HEPES (pH 7.4) and 50 mM NaCl, followed by HPLC analysis (courtesy of Dr. Ahn).

4.3.2 Preparation of DOTA-Peptide Conjugates and Radiochemistry

DOTA-Peptide conjugates were successfully prepared by coupling a thiol group with a maleimidomono-amide-DOTA. Thiol-reactive agents have been widely used to modify peptides and proteins at specific sites.[235, 236] Because a thiol group is more nucleophilic than amines at physiological pH, site-specific conjugations can be achieved by standard thiol-maleimide reactions. In this experiment, the peptide conjugation reactions were completed within 2 h under mild condition. High chemical yields

(approximately 60%) were obtained after HPLC purification. The DOTA conjugates allowed us to tag peptides with ^{64}Cu.

At the non-carrier-added (n.c.a.) level, all peptide conjugates were successfully labeled with ^{64}Cu in 0.1 M ammonium acetate (pH 6.5). By reacting 10 μg of the peptide conjugate with 1.5-2.3 mCi of ^{64}Cu, more than 50% radiochemical yield was obtained. The recovery rate after purification by a pre-activated C_{18} Sep-Pak cartridge was > 75%. The radiochemical purity of the labeled peptide conjugates post purification by C_{18} Sep-Pak cartridge was > 97% as determined by HPLC. The highest achievable specific activity acquired for each conjugate was 1.0×10^6 MBq/μmol. The reaction conditions that were used to acquire the highest specific activity are shown in Table 4.2.

Table 4.2 Reaction conditions for the ^{64}Cu labeled peptide conjugate

^{64}Cu (μCi)	EM2198-DOTA (μg)	NH_4OAc (pH 6.5)	Labeling efficiency	Radiochemical yield*
83.6	0.001	50 μL	8.03%	0%
198.4	0.2	50 μL	100%	70.56%
204	0.4	50 μL	100%	76.47%
188.7	0.8	50 μL	100%	75.83%
211	1.6	50 μL	100%	87.20%

* The labeled peptide was eluted by a pre-activated C_{18} Sep-Pak cartridge with 80% EtOH.

4.3.3 Receptor Binding Assays

As the DOTA placement may distort the peptide structure and diminish the binding capability of the peptide, the IC_{50} values of the peptide conjugates to GLP-1R were determined by a competitive binding assay with ^{125}I-exendin-4(9-39). INS-1 832/13 cells that overexpress GLP-1 receptors were incubated with ^{125}I-exendin-4(9-39) and the peptide conjugate at the concentration of 0-1000 nM. The IC_{50} values of DOTA conjugated GLP-1, [D-Ala^8]GLP-1, EM2196, EM2198, and exendin-4 were determined

to be 0.28 ± 0.05, 0.36 ± 0.24, 0.14 ± 0.03, 0.13 ± 0.03, and 0.24 ± 0.11nM, respectively. Compared to the IC_{50} values of EM2196 and EM2198 before DOTA conjugation (Table 4.3), no significant difference was observed, suggesting that the DOTA conjugation has negligible effect on the GLP-1 analogs for receptor recognition (Table 4.3). In addition, the lactam bridges in the bicyclic peptides EM2196 and EM2198 resulted in an increase in binding affinity (approximately 2-fold) compared to GLP-1.

Table 4.3 GLP-1R binding affinities of the GLP-1 analogs as measured by IC_{50} values

Peptide	GLP-1	[D-Ala^8]GLP-1	EM2196	EM2198	Exendin-4
IC_{50} (nM)	2.4 ± 1.5[a]	0.15 ± 0.01[a]	0.10 ± 0.06	0.18 ± 0.07	0.65 ± 0.01[b]
Peptide Conjugates	GLP-1-DOTA	[D-Ala^8]GLP-1-DOTA	EM2196-DOTA	EM2198-DOTA	Exendin-4-DOTA
IC_{50} (nM)	0.28 ± 0.05	0.36 ± 0.24	0.14 ± 0.03	0.13 ± 0.03	0.24 ± 0.11

[a]The value was determined by Sarrauste et al.[350]
[b]The value was determined by Wild et al.[134]

4.3.4 *In Vivo* Evaluations

With the encouraging *in vitro* results, the focus of our first attempt was to evaluate if the pancreas area can be imaged by the five ^{64}Cu labeled peptide conjugates. As such, we performed dynamic (0 – 60 min) scans with normal mice.

Among all peptide conjugates, the pancreas area can only be visualized by EM2198 (Figure 4.3A). This observation was directly reflected by the SBI values (Figure 4.3B), which are the index of the pancreas contrast compared to the liver. As the use of ^{111}In-DTPA-Ahx-Lys^{40}-exendin-4 has been reported for imaging mouse pancreas and insulinoma, we expected that the pancreas could be clearly imaged by^{64}Cu labeled exendin-4. However, because exendin-4 showed the highest kidney uptake among all the GLP-1 analogs (Figure 4.3C), the pancreas area was heavily masked by the high kidney uptake and resulted in the overestimated pancreas contrast value of exendin-4.

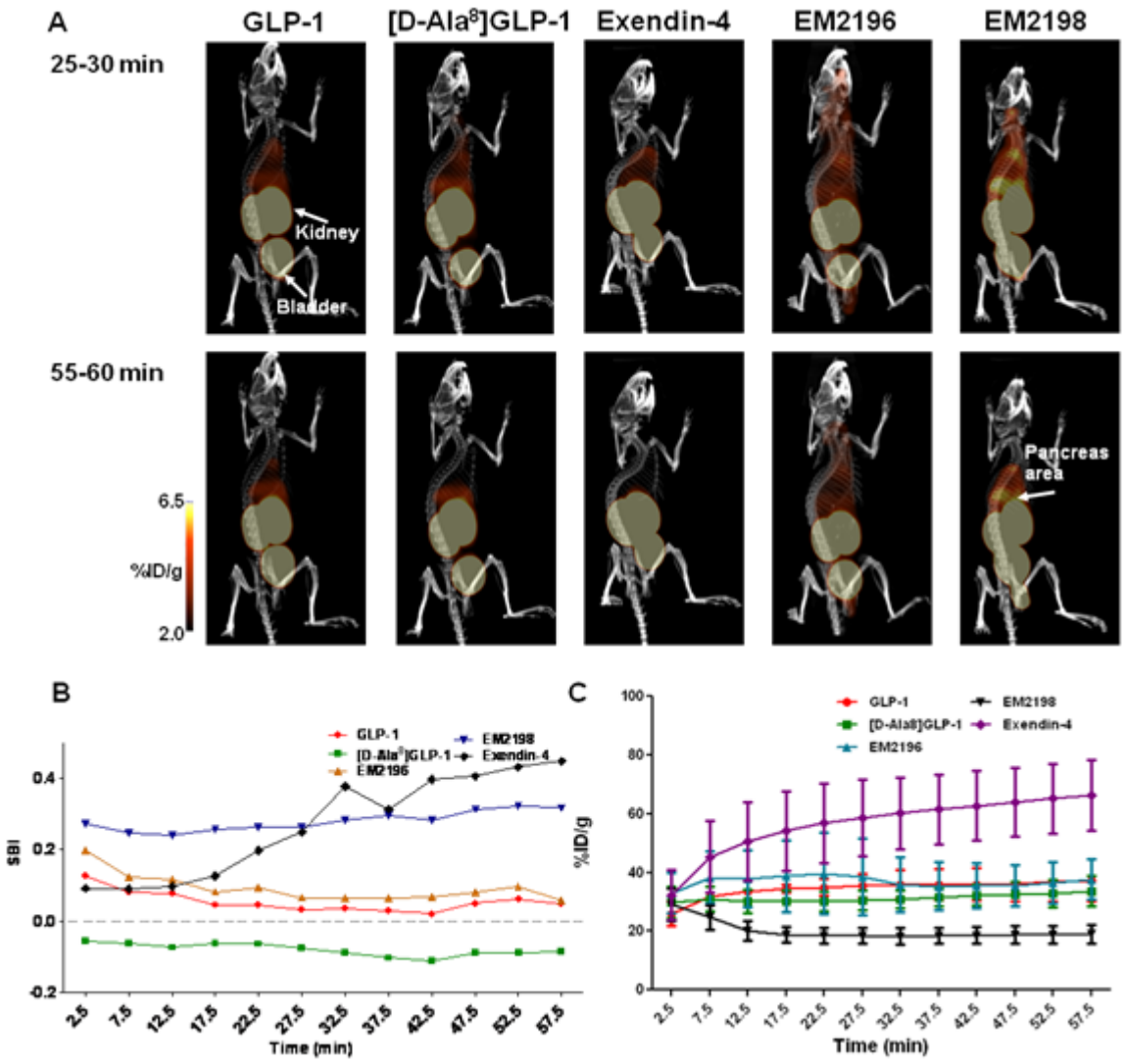

Figure 4.3 Dynamic PET-CT images and data analysis of the ^{64}Cu labeled GLP-1 analogs in normal BALB/c mice. (A) Comparative dynamic microPET/CT images, (B) SBI, and (C) kidney uptake of the five ^{64}Cu labeled DOTA-peptide conjugates in the normal mice (n = 3 per group). The imaging analyses were based on percentage of injected dose per gram tissue (%ID/g). The SBI is defined as SBI = $(C_P - C_L)/C_L$, where C_P represents the signal intensity in the pancreas region, and C_L represents the signal intensity of the liver.

Because mouse pancreas is a soft organ with irregular shape and surrounded by the liver, stomach, spleen, and intestines, it is challenging to define the pancreas accurately by CT alone (Figure 4.4).

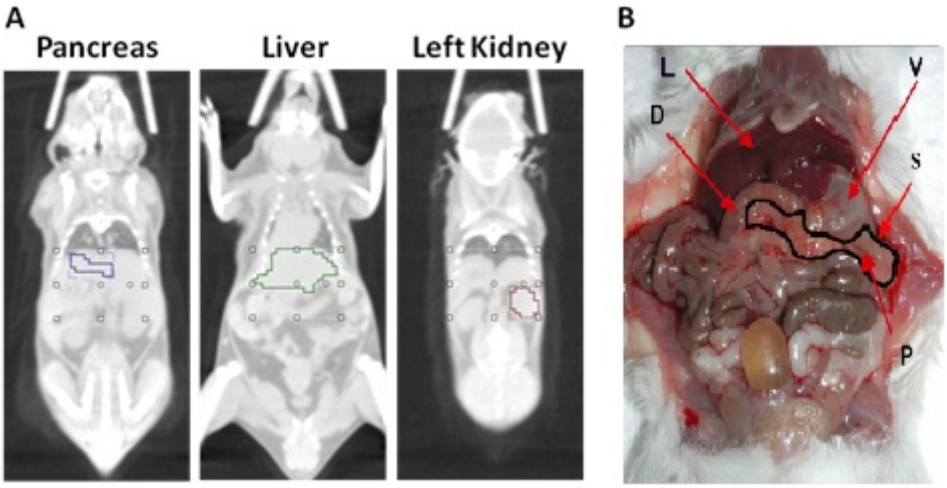

Figure 4.4 (A) CT-aided ROI selection for imaging analysis; (B) The anatomical structures of a mouse (D, duodenum; L, liver; V, stomach; S, spleen; P, pancreas). The mouse anatomical image was made by Medarova et al.[351]

To verify the *in vivo* imaging results, we performed e*x vivo* microPET/CT scans. As shown in Figure 4.5, the pancreas showed significantly higher accumulation of ^{64}Cu labeled EM2198 than other surrounding organs, such as the liver, stomach, spleen, and intestines, which was in agreement with our imaging analyses.

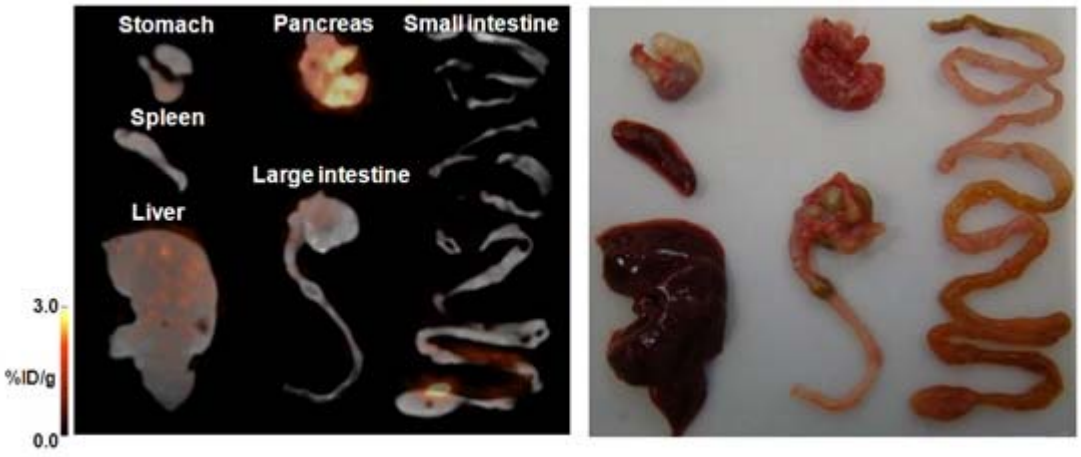

Figure 4.5 *Ex vivo* microPET/CT image of ^{64}Cu-EM2198 in normal mouse at 1 h p.i. The liver, spleen, stomach, intestines, and pancreas were collected and imaged. The imaging signal intensities were indicated by the absolute uptake as presented by percentage of injected dose per gram tissue (%ID/g).

As ^{64}Cu-EM2198 appears to have the most potential to image the mouse pancreas, we performed two experiments to verify whether the imaging was β-cell specific by i) co-injecting with unlabeled exendin-4 and ii) using STZ-induced diabetic mice. As shown in Figure 4.6A, no pancreas activity was observed from the group of mice that received unlabeled exendin-4. Based on the imaging analysis, the SBI value was dramatically reduced from 0.3 to ~0 at 20 min p.i. (Figure 4.6B).

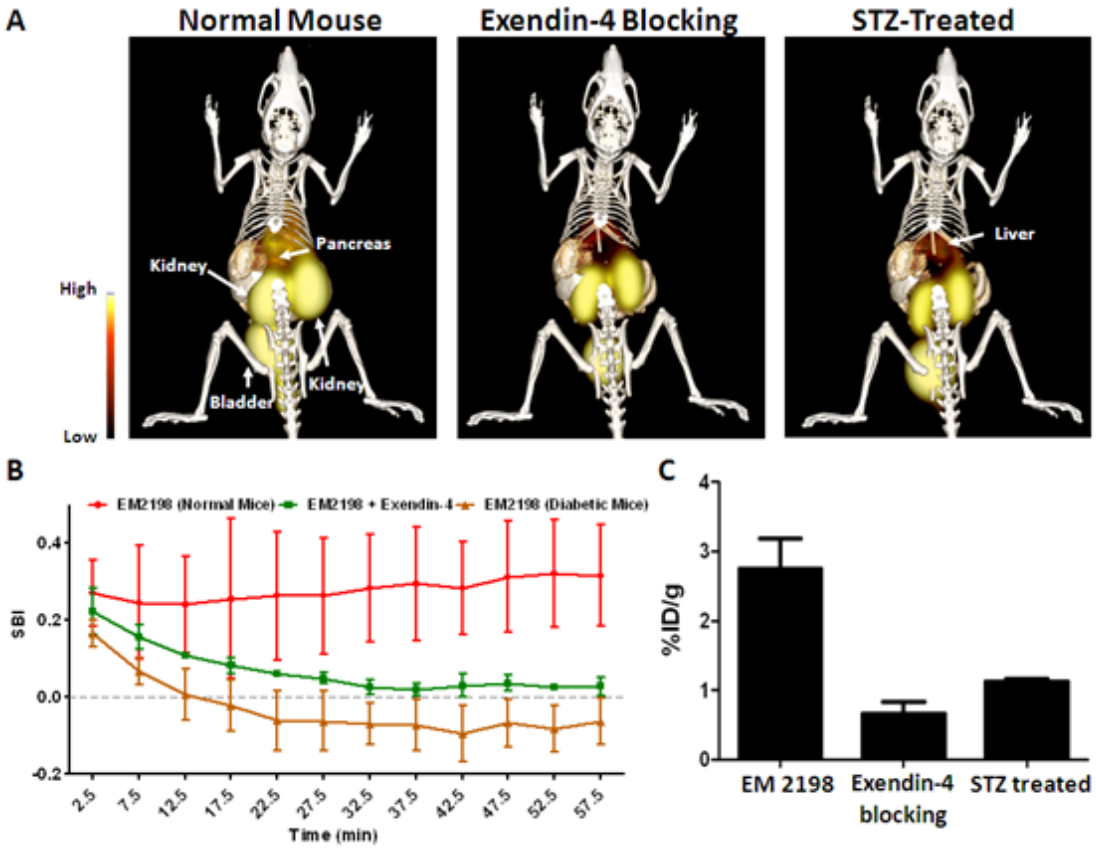

Figure 4.6 MicroPET/CT images and data analysis of ^{64}Cu-EM2198 in the normal, exendin-4 blocking, and STZ-treated mice. (A) Comparative dynamic microPET/CT images are presented at the time frame of 55-60 min (n = 3 per group). The contrast enhanced CT with orally administered $BaSO_4$ was performed to co-register with PET images (signals assigned as indicated by arrows). The central spine is artificially removed to reveal the pancreas area. (B) The SBI and (C) post imaging biodistribution results in the pancreas demonstrated the specific binding of ^{64}Cu-EM2198.

We performed additional imaging studies by using STZ-induced diabetic mice. STZ is a chemical agent that is known to selectively damage the insulin-producing β-cells and has been widely utilized for inducing diabetes in experimental animals.[352-357] The T1D mouse model induced by STZ is well established.[352, 353, 358] After five consecutive daily treatments with STZ, all the normal mice became diabetic. Most animals reached the peak with their blood glucose more than 280 mg/dl by day 14 (Figure 4.7). However, the glycemic numbers of these mice were slightly reduced and became stable after 16 days of the treatment.

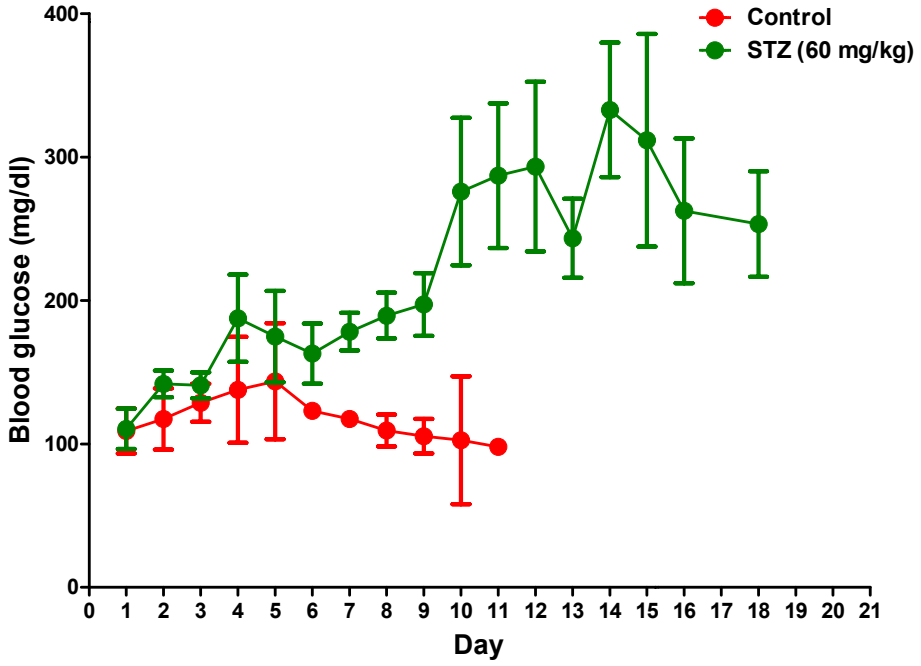

Figure 4.7 The establishment of STZ-induced diabetic mouse model. The blood glucose concentration were measured on the daily base. The mice were i.p. injected with either 10 mM PBS or STZ (60 mg/Kg) (n = 6).

Similar to the imaging results from the normal mice co-injected with unlabled exendin-4, no pancreas contrast was observed in the STZ-induced diabetic mice (Figure 4.6A). Their SBI values were slightly below 0 after 15 min injection (Figure 4.6B). The

imaging findings were further supported by the post imaging biodistribution (Figure 4.6C) and *ex vivo* microPET/CT scans (Figure 4.8). Compared to normal mice, signals from the pancreas of STZ-induced diabetic mice were significantly reduced and close to background level (Figure 4.8). Furthermore, the pancreas uptake of ^{64}Cu-EM2198 in normal mice (2.76 ± 0.43 %ID/g) was significantly higher than that in the STZ-diabetic mice (1.12 ± 0.04 %ID/g; $p = 0.0028$) based on the post imaging biodistribution results.

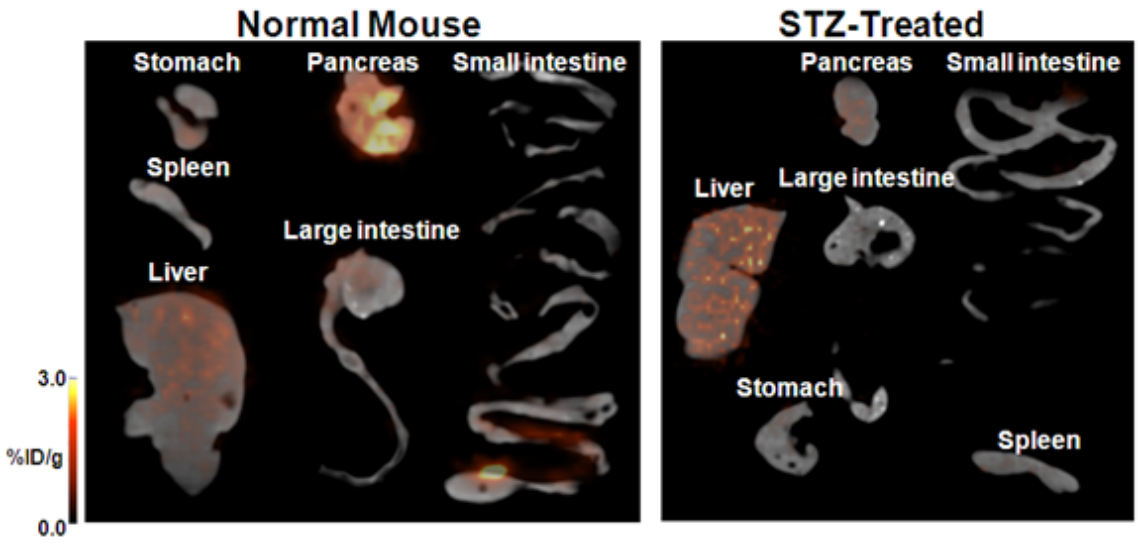

Figure 4.8 Comparative *ex vivo* microPET/CT images of ^{64}Cu-EM2198 in normal and STZ-treated mice at 1 h p.i. The liver, spleen, stomach, intestines, and pancreas were collected and imaged. The imaging signal intensities were indicated by the absolute uptake as presented by percentage of injected dose per gram tissue (%ID/g).

To confirm our imaging findings of ^{64}Cu-EM2198 was relevant to the expressions of GLP-1R on functional β-cells, the pancreas of the normal and STZ-treated diabetic mice used for the imaging studies were harvested, fixed, and sectioned for histological examinations. As shown in Figure 4.9, no significant morphologic changes were observed in the pancreatic tissues from both groups. However, immunostaining of insulin and GLP-1R was readily detectable in the cytoplasm of the normal but not STZ-diabetic

islet cells, suggesting that i) the β-cells were destroyed by STZ and ii) the GLP-1R was specifically expressed on the β-cells. On the contrary, inhomogeneous immunostaining of glucagon was observed in the islet cells of both groups of the tissues. This finding reflects the fact that i) α-cells constitute 15-20% of the islets and ii) further supports the selectivity of STZ in β-cell destruction. No specific staining was found when there was no primary antibody applied.

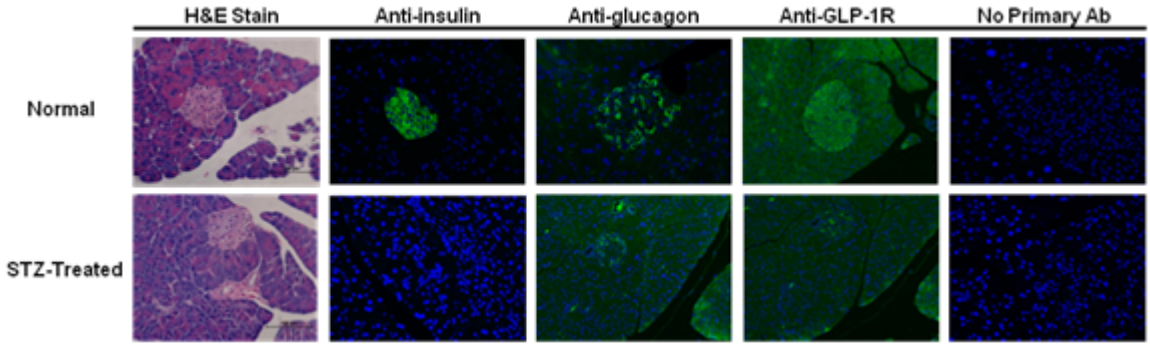

Figure 4.9 Histological analyses of the pancreas tissues from normal and STZ-treated mice. Paraffin-embedded sections from normal and STZ-treated mouse pancreata were stained by H&E or processed for immunohistology with anti-insulin, anti-glucagon, or anti-GLP-1R antibody. Indirect staining of slides was performed with goat anti-rabbit immunoglobulin antibody. The H&E stain and immunohistology sections are at 200× magnification.

Although our results confirmed that the uptake of ^{64}Cu-EM2198 was restricted in the functional pancreatic β-cells, the high renal accumulation may impede its further applications. It has been reported that the high kidney uptake of ^{111}In labeled octreotide and exendin-4 can be alleviated by albumin fragments.[299] As such, the effect of albumin fragments on the renal uptake of ^{64}Cu-EM2198 was analyzed. In this study, a group of normal mice were co-injected with ^{64}Cu-EM2198 and 1 mg of albumin fragments and then dynamically scanned (0-60 min). As shown in Figure 4.10A, there was no pancreas contrast observed by using this method. Although the renal accumulation was

significantly reduced 20-30% at 20 min p.i., it appeared that the targeting property of ^{64}Cu-EM2198 was abolished (Figure 4.10B). This is likely caused by the fragmentation of ^{64}Cu-EM2198, which was resulted from the cleavage of trypsin that might present in the albumin fragment solution.

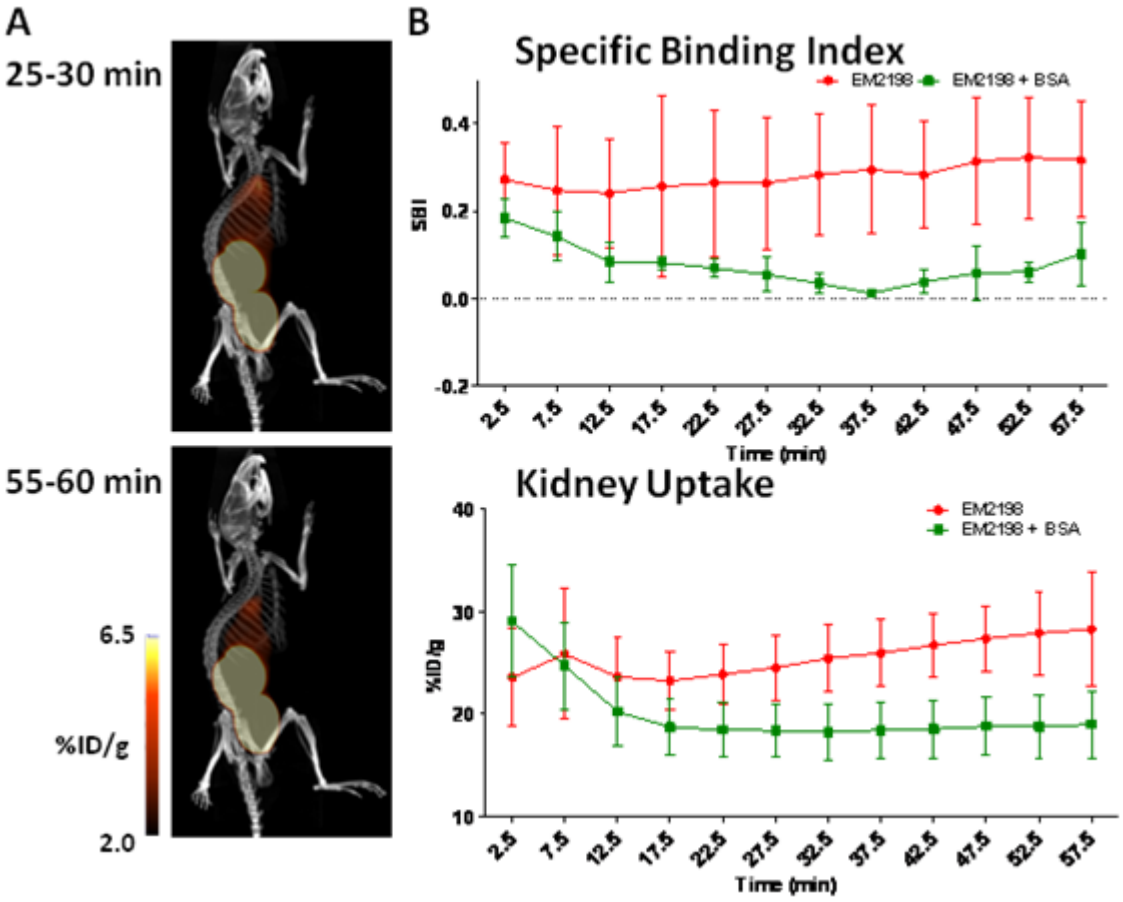

Figure 4.10 (A) microPET/CT images and (B) imaging analysis of the mice co-injected with ^{64}Cu-EM2198 and albumin fragments.

Live animals contain varieties of proteolytic enzymes, which may degrade radiotracers *in vivo*. Given the importance of stability for radiotracer development, the metabolites of ^{64}Cu labeled GLP-1 conjugates were evaluated in the blood and kidneys.

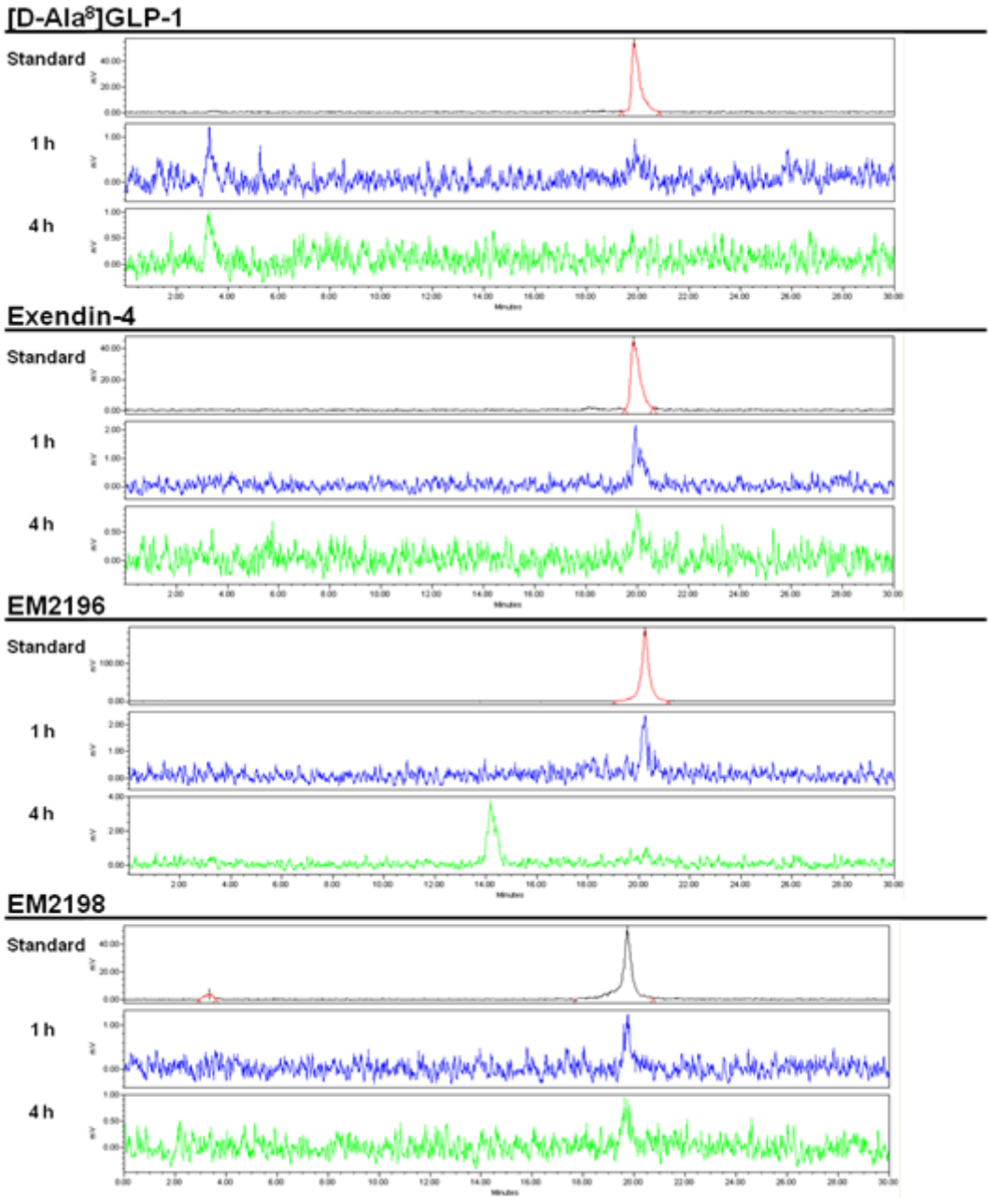

Figure 4.11 HPLC analysis of metabolites in the blood. Comparative HPLC chromatograms of ^{64}Cu labeled [D-Ala^{8}]GLP-1, EM2196, EM2198, and exendin-4 extracts from the mouse blood at 1 and 4 h p.i.

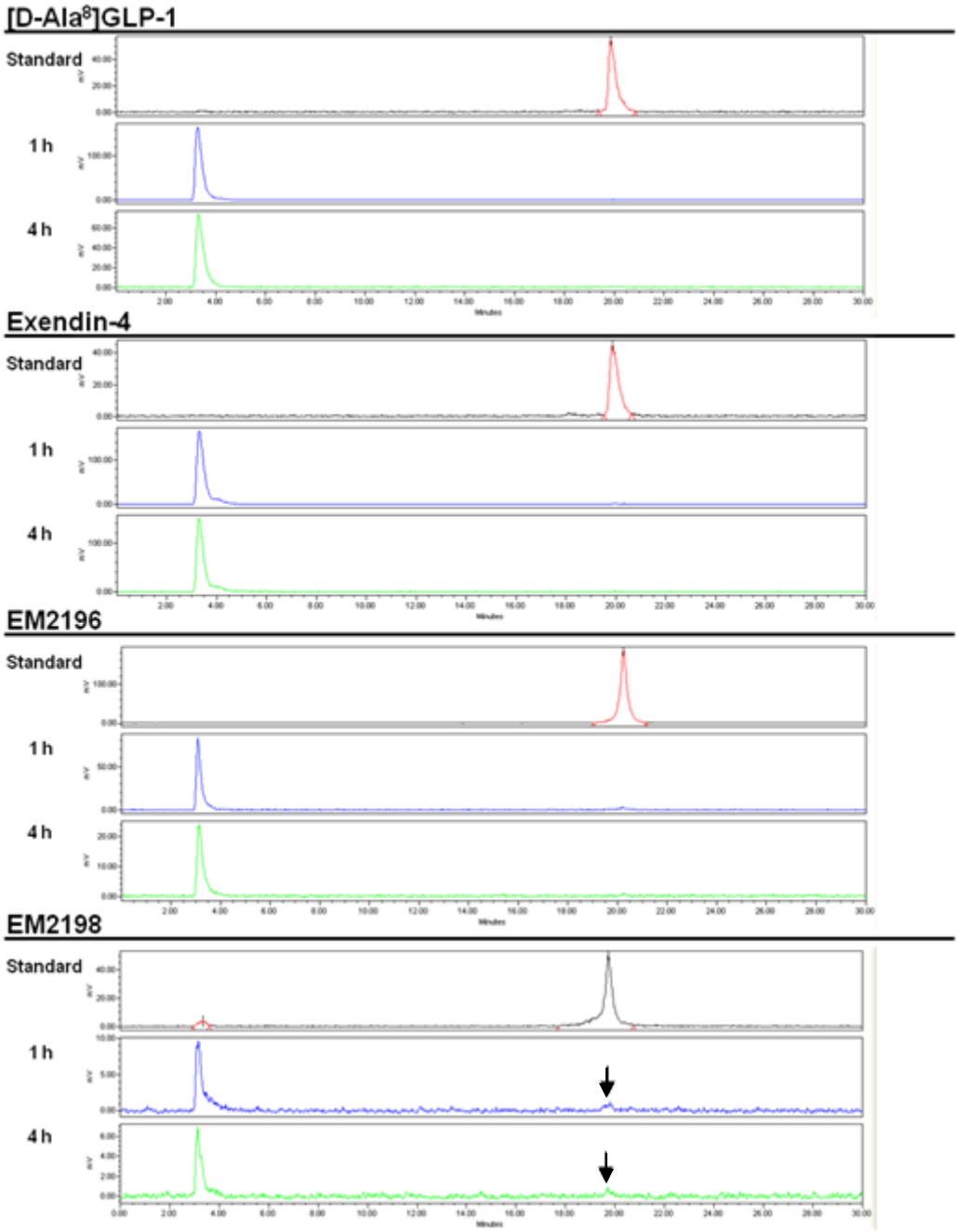

Figure 4.12 HPLC analysis of metabolites in the kidneys. Comparative HPLC chromatograms of ^{64}Cu labeled [D-Ala^{8}]GLP-1, EM2196, EM2198, and exendin-4 extracts from the mouse kidneys at 1 and 4 h p.i.

As shown in Figure 4.11, only EM2198 and exendin-4 remained intact in the blood throughout the studies. Of note, EM2196 stayed intact within 1 h p.i. but was near

completely degraded at 4 h p.i. Because i) EM2196 and EM2198 have identical lactam bridges between residues 30-34 and ii) different retention time was observed from the metabolites of [D-Ala^8]GLP-1 and EM2196, our data implies that the lactam bridges between residues 18-22 and 30-34 are necessary to prevent GLP-1 analogs from enzymatic proteolysis during blood circulation. On the contrary, all of the ^{64}Cu labeled peptide conjugates showed > 90% of degradation in the kidney even within 1 h p.i. (Figure 4.12). Only EM2198 was found to have ~8% and ~6% of intact at 1 and 4 h p.i. The other GLP-1 conjugates were completely degraded within 1 h p.i. These data indicates that EM2198 and exendin-4 were stable during blood circulation.

4.4 Discussion

There are several technical challenges to image the β-cells noninvasively. The small size, low abundance, and scattered distribution of the islets create difficulties in imaging. To date, ^{11}C and ^{18}F labeled DTBZ derivates that specifically bind to VMAT2 demonstrated the most encouraging results. Besides endocrine cells and brain, the expression of VAMT2 has been reported on the pancreatic β and pp cells.[223] Recently, the first clinical practice of (+)-[^{11}C]-DTBZ has been reported with long-standing T1D patients and healthy subjects.[224] To estimate the binding potential (BP_{ND}) and functional binding capacity (the sum of voxel BP_{ND} x voxel volume) of (+)-[^{11}C]-DTBZ on VMAT2, Goland et al. selected renal cortex as the reference tissue for calculation. Although their results suggested that PET can be used to quantify VMAT2 binding in the human pancreas, high nonspecific pancreas binding of (+)-[^{11}C]-DTBZ resulted in

overestimation of BCM. In this part of work, we have used GLP-1 analogs to target GLP-1R in hope to outperform the DTBZ-based imaging techniques for BCM imaging. As GLP-1R is highly related to the insulin release, the approach developed herein would provide further assessment of β-cell function.

In order to evaluate the C-terminal DOTA conjugation of EM2196 and EM2198 on GLP-1R interaction, receptor binding assays were carried out. Exendin-4, GLP-1, and [D-Ala^{8}]GLP-1 have been reported with high binding affinities.[134, 340] In our studies, both bicyclic GLP-1 analogs demonstrated slightly higher receptor affinity suggesting that the introduction of the two lactam bridges may improve the peptide binding capability to GLP-1R. In addition, high binding affinities of all peptide conjugates confirmed that the DOTA conjugation at their C-terminus did not compromise their receptor interaction.

Unlike DTBZ analogs, the excretion of the ^{64}Cu labeled GLP-1 analogs was mainly through the kidneys. Since it is located relatively distant from the pancreas, we would be able to obtain a better contrast in the pancreas area from these GLP-1 analogs. In the imaging studies, we quantified the pancreas uptake of the labeled conjugates by selecting ROIs. The liver was chosen as a reference tissue for comparison due to its anatomical proximity to the pancreas without expression of the GLP-1R. Among all the peptide conjugates, ^{64}Cu-EM2198 showed the pancreas region with the highest contrast on microPET/CT images. We were surprised that ^{64}Cu-exendin-4 did not perform as well as ^{64}Cu-EM2198. This is likely caused by the high kidney uptake of ^{64}Cu-exendin-4, which visually masked the pancreas contrast. Because the pancreas is more of a spread out membrane in mouse than a solid organ and it is surrounded by the liver, stomach,

spleen, and intestines, where high nonspecific accumulations of a PET tracer typically occur, we confirmed our *in vivo* imaging findings by i) *ex vivo* imaging scans, ii) *in vivo* blocking studies, and iii) *in vivo* imaging studies of STZ-treated diabetic mice.

As exendin-4 is a well recognized GLP-1 analog that specifically binds to GLP-1R, the imaging studies of normal mice co-injected with ^{64}Cu-EM2198 and unlabeled exendin-4 were first performed. The pancreas uptake of EM2198 dropped significantly to a level approaching the activity measured in the liver, where no expression of GLP-1R has been reported. The specificity of ^{64}Cu-EM2198 to functional β-cells was revealed by the loss of signal in the STZ-treated diabetic mice. Results from the post-PET biodistribution (Figure 4.6C) and *ex vivo* microPET/CT scans (Figure 4.8) further confirmed our *in vivo* imaging findings (Figure 4.3A).

The relevant between the pancreas uptake of ^{64}Cu-EM2198 and the expression of GLP-1R was further verified by histological analyses. While the H&E staining of the pancreas tissues from normal and STZ-treated mice did not show significant differences in terms of islet areas and numbers of islets, immunostaining with anti-insulin and anti-GLP-1R were dramatically decreased after selective β-cell destruction by STZ. Furthermore, the STZ treatment has no impact on the anti-glucagon antibody staining of islets. Taken together, all of these results unequivocally demonstrated that the uptake of ^{64}Cu-EM2198 is specific to the GLP-1R expressed on the pancreatic β-cells.

As the signals of PET imaging reflect the *in vivo* distribution profiles of both radiotracer and its metabolites, the *in vivo* stability of the GLP-1 conjugates might play an important role in their β-cell targeting properties and other *in vivo* characteristics. As

such, we performed HPLC analysis of their metabolites in blood and kidney homogenates. Based on the HPLC analyses, only ^{64}Cu labeled EM2198 and exendin-4 remained intact at 4 h p.i. in the blood. Previous report indicated that exendin-4 is stable against DPP-IV and NEP 24.11,[359] but native GLP-1 is readily cleaved by both enzymes.[359] Since different metabolites showed as peaks with retention times different from their original conjugates, our results demonstrated the importance of site-specific cyclization to prevent the GLP-1 analog from enzymatic degradation during the blood circulation.

4.5 Conclusion

The GLP-1 analogs have been evaluated for BCM imaging. As expected, the high stability of GLP-1 analogs against DPP-IV can be achieved by replacing L-Ala on the 8th position with D-Ala. By introducing two lactam bridges site-specifically to the GLP-1 analogs, the peptide stability against NEP 24.11 was strongly improved. As Ahx was inserted as a spacer between a peptide construct and DOTA, negligible effects on the targeting properties of these GLP-1 analogs were observed. In this work, imaging studies showed that the pancreas uptake of ^{64}Cu-EM2198 in the normal mice can be visualized and differentiated from the nearby organs. The imaging findings were confirmed by co-injecting the normal mice with unlabeled exendin-4 and using the STZ-treated mice as an animal model. Further histological examination indicates the specific uptake of ^{64}Cu-EM2198 in the functional pancreatic β-cells. Taken together, we have demonstrated the GLP-1R as a potential biomarker for BCM imaging and successfully established a

systematic analysis procedure. The ^{64}Cu-EM2198 developed herein holds the potential to determine BCM noninvasively.

CHAPTER FIVE

OTHER ATTEMPS

5.1 Introduction

Because of i) the capability of absolute imaging quantification, ii) the unique feature to image ^{11}C, ^{13}N, or ^{15}O labeled compounds, and iii) the superior sensitivity, the role of PET has been well-established in the field of molecular imaging that potentiates the development of PET imaging probes. Among the four standard PET nuclides (^{11}C, ^{13}N, ^{15}O, and ^{18}F), ^{18}F is the most popular radioisotope due to its low positron energy ($E_{\beta+max}$: 0.64 MeV) and high positron branching ratio (97%). During the development of ^{18}F labeled radiotracers, it is often substituted with hydroxyl group of the lead compounds based on similar steric and electrostatic properties. As ^{18}F can be produced in the amount of Ci level with the half-life of 110 min, these characteristics allow syntheses of ^{18}F labeled radiotracers and evaluations of their biological properties over hours. In addition, it is also doable to transport [^{18}F]HF water or ^{18}F labeled compounds to facilities and hospitals without onsite cyclotron facility.

On the other hand, interest in using ^{68}Ga for clinical PET comes from its availability from an in house $^{68}Ge/^{68}Ga$ generator without the need of an onsite cyclotron. With a half-life of 68 min, ^{68}Ga decays by 89% positron emission ($E_{\beta+max}$: 1.92 MeV) and 11% electron capture. Because ^{68}Ga can be labeled to biomolecules conjugated with bifunctional chelators, it is feasible for kit production and allows PET centers to benefit for important clinical studies.

As presented in the Chapter 3 and 4, 10PD and EM2198 can serve as lead compounds to develop imaging agents for lung cancer and BCM imaging. In this chapter, I summarize three of the attempts that I have made in order to further develop the lead compounds for lung cancer and BCM imaging. However, limited by time, no conclusive results have been made.

5.2 *Ex Vivo* Imaging Studies of ^{64}Cu-EM2198 in Perfused Normal Mouse

In this study, the normal BALB/c mouse was received 100 μCi of ^{64}Cu-EM2198 intravenously. After the dynamic scan (0-60 min), the mouse was sacrificed and perfused with 40 mL of DPBS. The liver, spleen, stomach, intestines, and pancreas were excised and imaged by 15 min of PET imaging. The imaging reconstruction and quantification methods were the same as 4.2.8.

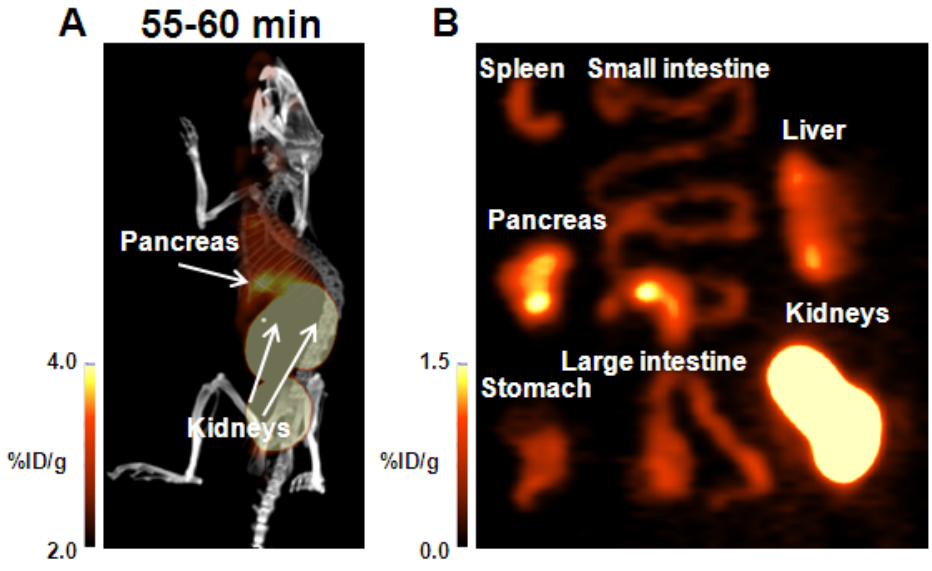

Figure 5.1 (A) Dynamic *in vivo* and (B) e*x vivo* microPET image of ^{64}Cu-EM2198 in normal mouse. The liver, spleen, stomach, intestines, kidneys and pancreas were collected and imaged. The imaging signal intensities were indicated by the absolute uptake as presented by percentage of injected dose per gram tissue (%ID/g).

As shown in Figure 5.1, the pancreas area can be visualized by ^{64}Cu-EM2198 (Figure 5.1A). The pancreas showed significantly higher accumulation than other surrounding organs, such as the liver, stomach, spleen, and intestines. The high kidney uptake was also observed after perfusion.

5.3 Radiolabeling EM2198 with ^{18}F and Preliminary Evaluation of [^{18}F]EM2198

Peptide labeling with ^{18}F can be achieved by using primary amine or thiol as functional groups. Currently, most reported ^{18}F labeled prosthetic groups for biomolecules react with primary amines. As most peptides or proteins contain multiple lysines, the major concern by using this approach is the possibility to abolish the biological activity of the biomolecules of interest when one or more lysines are located at or near the active site.

Several agents have been applied to modify biomolecules site-specifically by coupling with thiol groups.[237-240] All of them bear a maleimide as the functional group. Considering the peptide construct, we conjugated EM2198 with [^{18}F]FBEM (N-[2-(4-[^{18}F]fluorobenzamido)ethyl]maleimide) to yield [^{18}F]EM2198. The other advantage by performing this synthetic route is that the intermediate coumpound, [^{18}F]FBA, can easily be used to couple biomolecules with primary amine groups.

Preparation of FBEM

The cold standard compound, FBEM, was prepared to verify the radiosynthesis of [^{18}F]FBEM. Briefly, FBEM was synthesized according to a published procedure [237] with

modifications. 4-Fluorobenzoic acid (0.071 mmol), N-(2-Aminoethyl)maleimide (0.11 mmol), and 7-Azabenzotriazol-1-yloxy)tripyrrolidinophosphonium hexafluorophosphate (PyAOP, 0.11 mmol) were dissolved in 0.1 mL of DMSO. After adding 50 μL of N,N-diisopropylethylamine (DIPEA), the reaction was allowed to proceed overnight at room temperature. The product was purified by HPLC with a Waters XTerra C_{18} column (5 μm, 4.6 mm × 150 mm). The flow rate was set at 1 mL/min using a gradient system starting from 100% solvent A by a linear ramp to 100% solvent B at 50 min. Solvent A: 0.1% trifluoroacetic acid (TFA) in water (v/v); solvent B: 0.1% TFA in acetonitrile (v/v). The collected fractions were lyophilized and characterized by ^{1}H NMR (acetonitrile-d, 400 MHz): 7.85-7.95 (dd, 2H, phenyl o-H); 7.25-7.35 (t, 2H, phenyl m-H); 6.90 (2H, CH=CH); 3.85-3.95 (t, 2H, CH_2); 3.60-3.70 (dd, 2H, CH_2).

Preparation of [^{18}F]FBEM (Scheme 5.1)

Ethyl 4-trimethylammoniumbenzoate trifluoromethanesulfonate was used as the precursor. The synthesis of [^{18}F]FBA was semi-automatically conducted in TRACERlab FX_{FN} synthesizer with the protocol FBA ver 1.2. Briefly, after the delivery of [^{18}F]HF water to the synthethic module, [^{18}F]fluoride was isolated by a ^{18}F separation cartridge. The cartridge was washed by a solution of K_2CO_3 (5 mg in 500 μL H_2O) and then [^{18}F]fluoride was eluted by a solution of Crypand 222 (25 mg in 1 mL MeCN). After azeotropic evaporation of H_2O (2 × 1 mL MeCN, 110 ^{o}C, flow of N_2), the precursor (3 mg, 0.008 mmol) in anhydrous MeCN (1 mL) was added. The labeling was conducted in a closed vial at 110 ^{o}C for 10 min followed by addition of 2 mL of 2 N NaOH for hydrolysis. The solution was neutralized with 4.5 mL of 1 N HCl and then passed

through a pre-activated C18 Sep-Pak plus cartridge. The [^{18}F]FBA was eluted by 2.0 mL of MeCN.

Scheme 5.1 Radiosynthesis of [^{18}F]EM2198

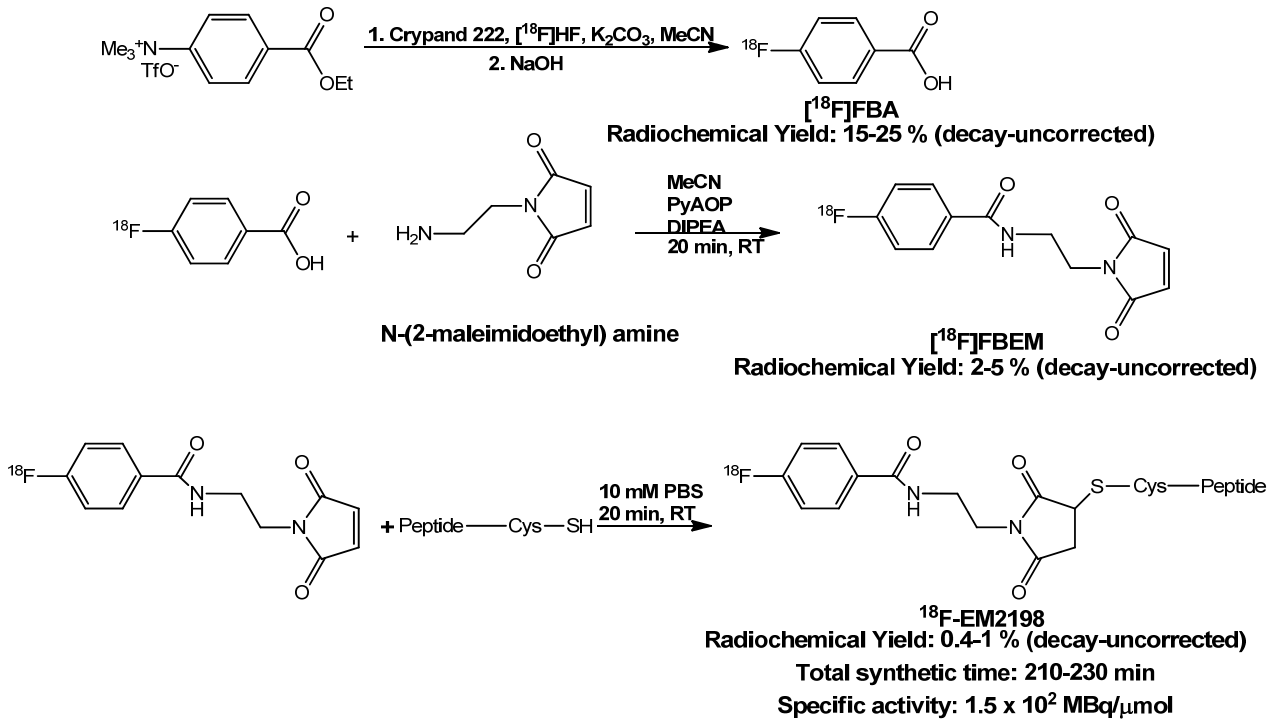

To the [^{18}F]FBA solution, tetrabutylammonium hydroxide (10 μL, 1 M in H_2O) was added to form [^{18}F]FBA salt. The H_2O was co-evaporated with anhydrous MeCN (3 × 2 mL) by a rotary vapor. The residue together with N-(2-aminoethyl)maleimide trifluoroacetate salt (3 mg, 0.012 mmol), PyAOP (6 mg, 0.012 mmol) and DIEPA (10μL), were then redisolved with 2 mL of anhydrous MeCN. The solution was reacted for 20 min at room temperature and purified by HPLC to yield [^{18}F]FBEM. The purified [^{18}F]FBEM was concentrated by a pre-activated C_{18} Sep-Pak plus cartridge.

Radiolabeling EM2198 with [^{18}F]FBEM

EM2198 (1 mg) with a thiol group was dissolved in 0.3 mL of 10 mM PBS (pH 7.4). The mixture was reacted for 20 min at room temperature and then purified by HPLC to obtain the final product. The overall non-decay corrected radiochemical yields of [^{18}F]FBA, [^{18}F]FBEM, and [^{18}F]EM2198 were 20 ± 8% (n = 13) and 5 ± 2% (n = 10), and 0.55 ± 0.15% (n = 3), respectively. The total reaction time was 58 ± 3 min for [^{18}F]FBA, 110 ± 10 min for [^{18}F]FBEM, and 220 ± 10 min for [^{18}F]EM2198 including HPLC purification. Radio-HPLC analysis (Figure 5.2) indicated that the radiochemical purity of [^{18}F]EM2198 was > 99% with the highest specific activity of 1.5 × 10^2 MBq/μmol.

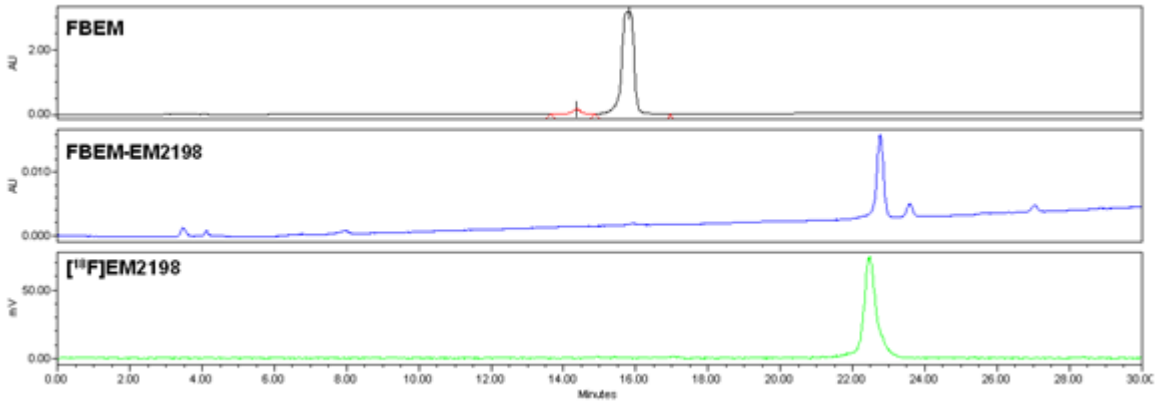

Figure 5.2 HPLC purification and characterization of ^{18}F labeled EM2198 with a Waters XTerra C_{18} prep column (10 μm, 10 mm × 250 mm). The flow rate was set at 4 mL/min using a gradient system starting from 100% solvent A by a linear ramp to 100% solvent B at 50 min. Solvent A: 0.1% trifluoroacetic acid (TFA) in water (v/v); solvent B: 0.1% TFA in acetonitrile (v/v).

The radiosynthesis of [^{18}F]EM2198 was confirmed by the cold standard, FBEM-EM2198, which was prepared by reacting EM2198 (2.8×10^{-4} mmol) and FBEM (0.003 mmol) in 10 mM PBS (0.5 mL, pH 7.4) at room temperature for 2 h followed by HPLC purification. The HPLC system with a Waters XTerra C_{18} column (10 μm, 10 mm × 250 mm) was used to purify and characterize [^{18}F]FBEM, [^{18}F]EM2198, and FBEM-

EM2198. The flow rate was set at 4 mL/min using a gradient system starting from 100% solvent A by a linear ramp to 100% solvent B at 50 min. Solvent A: 0.1% trifluoroacetic acid (TFA) in water (v/v); solvent B: 0.1% TFA in acetonitrile (v/v).

microPET/CT Imaging Studies

The procedure of the microPET/CT imaging studies is the same as described in Chapter 4. To our surprise, no specific pancreas activity was observed during the 0-60 min dynamic scan and most of the PET signal was retained in the liver and kidneys (Figure 5.3A).

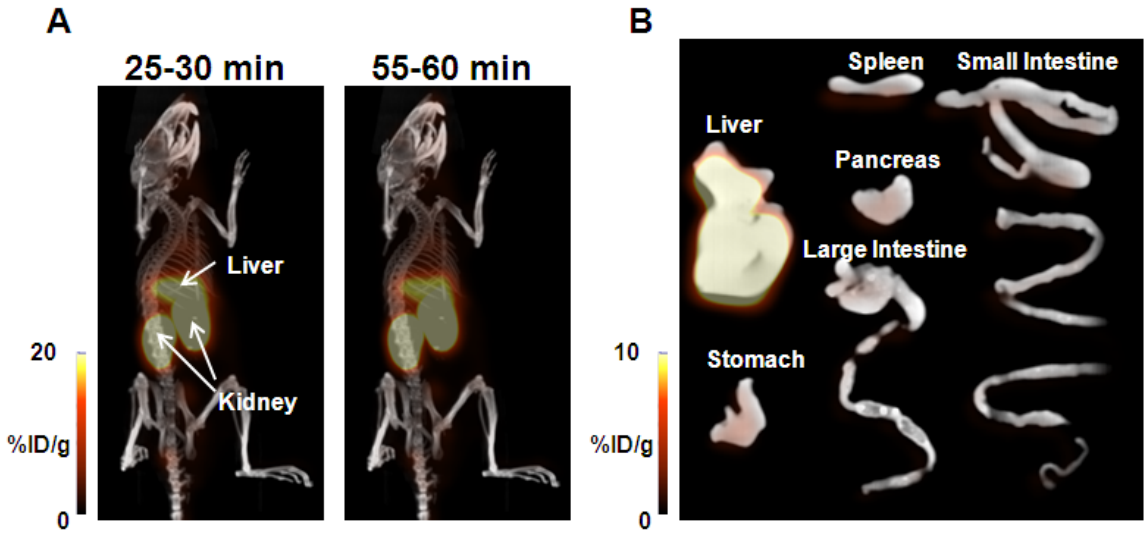

Figure 5.3 (A) Dynamic *in vivo* and (B) *ex vivo* microPET/CT images of [^{18}F]EM2198 in a normal mouse. The imaging signal intensities were indicated by the absolute uptake as presented by percentage of injected dose per gram tissue (%ID/g).

Based on the imaging analysis, the uptake of [^{18}F]EM2198 in the liver and kidneys was above 15%ID/g and 23%ID/g throughout the studies, respectively. The *ex vivo* imaging showed the PET signal in the excised organs was mainly from the liver (Figure 5.3B), which is consistent with the *in vivo* imaging results. It has been reported

that the liver uptake of octreotide and somatostatin analogs can be greatly enhanced by conjugating [^{18}F]FBA, whose introduction leads to a significant increase in lipophilicity and thus elevated hepatobiliary clearance.[112, 360, 361] In the recent studies performed by Cai et al.,[237] high uptake of [^{18}F]FBEM-SRGD in the liver (1h: ~6%ID/g) were also observed (based on the imaging quantification). The introduction of [^{18}F]FBEM seems to lead a significant increase in lipophilicity of the peptide construct and thus elevated hepatobiliary clearance. Further studies are required to determine the lipophilicity and *in vivo* stability of [^{18}F]EM2198.

5.4 Development of 10PD and 10PD Dimer as PET Imaging Probes for Lung Cancer

As a construct that contains two or more receptor ligands is expected to have cooperative receptor-ligand interactions,[362] the homogeneous multimeric ligand system has been applied to improve efficacy and selectivity of the radiolabeled peptides for receptor targeting.[362, 363] Approaches based on nanoparticles or multivalent scaffolds have been performed to exploit for the development of molecular imaging probes.[362-364]

As presented in Chapter 3, 10PD showed the best target-to-background ratios on the $\alpha_v\beta_6$-positive tumor. The dimerization of 10PD (Figure 5.4) was therefore constructed and evaluated as a potential PET imaging probe for lung cancer. To label 10PD or 10PD dimer with ^{68}Ga, 10 μg of the DOTA-peptide conjugate was reacted with the ^{68}Ga eluent (0.5 mL of 0.6 N HCl and 1.0 mL of 1.0 M HEPES) from the ^{68}Ge/^{68}Ga generator. The reaction was allowed to proceed at 80 ^{o}C for 30 min followed by purification via an activated C_{18} Sep-Pak cartridge. The radiochemical purity determined by HPLC was >

99% with the specific activity of 1×10^4 MBq/μmol (135 μCi/μg) and 3.75×10^3 MBq/μmol (20.4 μCi/μg) for 10PD and 10PD dimer, respectively. The lower specific activity of 10PD dimer is likely caused by the lower specific activity of ^{68}Ga in the eluent after long term use of the generator.

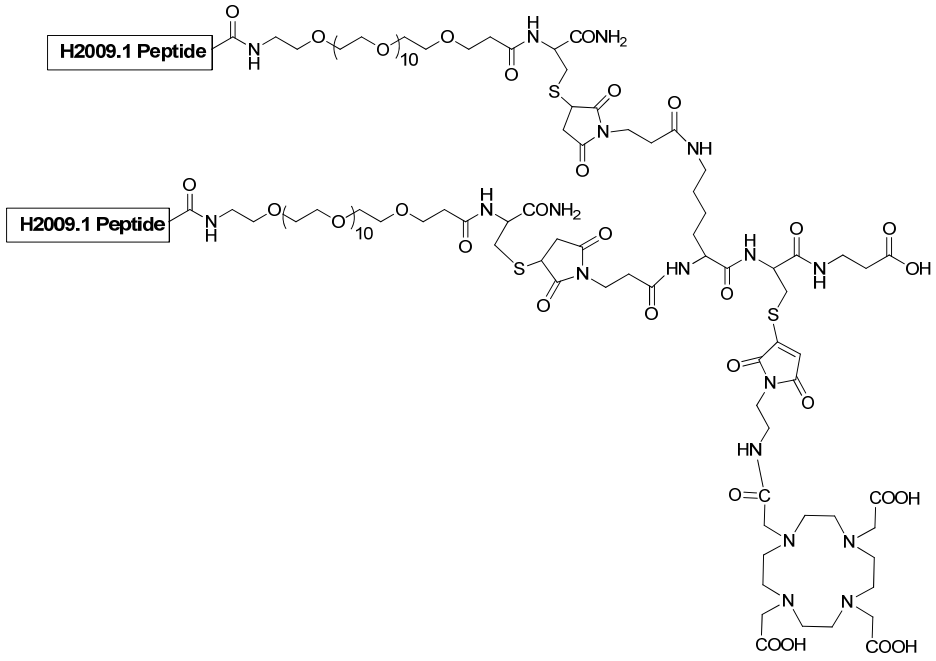

Figure 5.4 The chemical structure of 10PD dimer

The microPET/CT imaging studies of the ^{68}Ga labeled 10PD and H2009.1 10-mer dimer were performed on the SCID mice bearing H2009 ($\alpha_v\beta_6^+$), or H460 ($\alpha_v\beta_6^-$) and H2009 ($\alpha_v\beta_6^+$) tumors. As shown in Figure 5.5, nonspecific activity of both peptide conjugates observed in the lung, heart, and muscle was rapidly cleared. Whereas no tumor was visualized when the mice were received 10PD, the construction of the dimeric 10PD resulted in enhanced tumor uptake and retention.

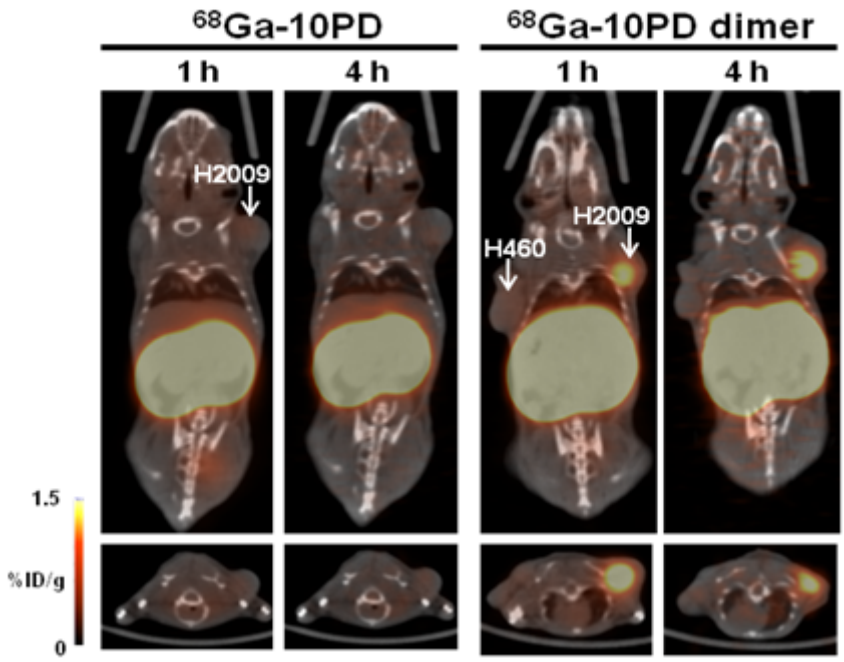

Figure 5.5 Comparative microPET/CT images of ^{68}Ga labeled 10PD and 10PD dimer in the tumor-bearing mice. The imaging signal intensities were indicated by the absolute uptake as presented by percentage of injected dose per gram tissue (%ID/g).

We noticed that even though uptake of 10PD dimer in the kidneys was significantly elevated (Table 5.1), no appreciable activity was excreted to the urinary bladder over time. Because renal accumulation of radiolabeled peptides leads to reduced detection sensitivity in the vicinity of the kidneys and limit the maximum tolerated doses that can be administered without inducing radiation nephrotoxicity, it is important to have low renal accumulation and high tumor uptake with longer retention for both imaging and therapeutic applications. In this regard, appropriate modification of 10PD dimer is needed to reduce renal uptake. By adjusting the length of PEG chain in 10PD, we may be able to modulate the overall hydrophilicity and molecular size, thus possibly improving *in vivo*

pharmacokinetics without compromising the tumor-targeting efficacy of the resulting peptide conjugates.

Table 5.1 PET Imaging quantification of ^{68}Ga labeled 10PD and 10PD dimer in the mice bearing H2009 and H460 tumors at 1 and 4 h p.i. (n = 3). Data are presented as %ID/g ± s.d.

	10PD		10PD dimer	
Tissue	1 h	4 h	1 h	4 h
lung	0.44 ± 0.07	0.42 ± 0.09	0.50 ± 0.06	0.37 ± 0.10
liver	0.60 ± 0.03	0.61 ± 0.07	1.70 ± 0.15	1.40 ± 0.15
kidney	8.60 ± 2.70	9.70 ± 2.10	78.40 ± 8.10	87.00 ± 12.30
muscle	0.17 ± 0.04	0.11 ± 0.06	0.18 ± 0.03	0.17 ± 0.08
heart	0.53 ±0.06	0.47 ± 0.07	0.49 ± 0.07	0.30 ± 0.12
H2009 tumor	0.44 ± 0.04	0.38 ± 0.07	1.70 ± 0.15	1.20 ± 0.30
H2009/muscle	4.94 ± 2.71	4.10 ± 1.86	9.53 ± 0.77	7.35 ± 1.52
H2009/lung	1.01 0.07	0.91 ± 0.03	3.41 ± 0.11	3.19 ± 0.06

PERSPECTIVES

A comprehensive and in-depth investigation of 10PD and EM2198 to monitor the progression of lung cancer and diabetes remains the immediate future direction of the current project. Further examination of the strategy in alternate preclinical models is required prior to the eventual clinical translation of the technology. However, several important issues regarding the development and optimization of the imaging probes based on 10PD and EM2198 must first be addressed and are discussed below.

First, although the high kidney uptake problem of 10PD can be alleviated by altering the modification sites, its *in vivo* targeting properties seemed to be sacrificed. Previous reports suggest that the molecular weight cutoff of glomerular filtration in rabbits, rats, and mice is 70 KDa.[365-368] This number is in agreement with the observation from DeNardo et al. who observed the kidney uptake of their PEGylated peptides were dramatically reduced (from ~40 to 7.9 %ID/g) when the total molecular weight of the molecules was above 70 KDa.[369] As our biodistribution data indicated that PEGylation can enhance the peptide accumulation in the H2009 tumor, comparing the effect of the peptide tagged with different length of PEG chain could be the next step to optimize their tissue distribution profiles.

In a similar fashion, the future applications of ^{64}Cu-EM2198 may also be hampered by the high renal accumulation. As BCM only constitutes less than 3% of the total pancreatic cell mass with sparse distribution and a portion of the pancreas area is closed to the kidneys, high kidney uptake is likely to affect the *in vivo* imaging quantifications on the pancreas region. Because the renal accumulation of ^{64}Cu-EM2198

cannot be reduced by the excess of unlabeled exendin-4, other factors must contribute to this phenomenon. It is believed that megalin and cublin are responsible for the uptake of various peptides.[298, 299, 370-372] As such, the high kidney uptake of ^{64}Cu-EM2198 may have resulted from the same mechanism. Numerous approaches including changing peptide sequence and co-administration of lysine have been investigated to reduce renal accumulation of radiolabeled peptides and antibody fragments.[373, 374] Recent research suggests that reduced renal uptake of radiolabeled peptides can also be achieved by co-injecting particular albumin-derived peptides [298] or changing labeling strategies,[173] which provide us alternatives to address this issue.

Second, as the onset of T1D is directly reflected by the β-cell failure and T2D consists of multiple metabolic abnormalities leading to hyperglycemia, the changes in the expression levels of GLP-1R per β-cell during T1D and T2D progression could be very different. The imaging technique aimed to monitor BCM noninvasively may therefore aid to detect the rate of disease progression and effectiveness of any therapeutic interventions for T1D patients. In T2D patients, such technique could provide the benefits in i) the identification of individuals at risk; ii) the assessment of disease stage; and iii) monitoring the treatments with potential to maintain or even reverse BCM. Future studies focused on longitudinal imaging evaluations in both T1D and T2D mouse models would be very important to connect our imaging findings presented herein with the diabetes research.

Finally, multiple receptors have been reported on the pancreatic β-cells and many cancers concomitantly.[375, 376] By taking advantages of the heterogeneity of receptor

expression on targeting cells and the multivalent scaffold that has been synthesized in this laboratory,[363] a heterogeneous system may further be developed to enhance the accumulation of our radiotracers in the targeting tissues.

ABBREVIATIONS

[^{11}C-methyl]TdR	[^{11}C-methyl]thymidine
[^{18}F]FBA	[^{18}F]fluorobenzoic acid
[^{18}F]FBT	4-[^{18}F]fluorobenzyltrozamicol
[^{18}F]FDG	[^{18}F]fluoro-2-deoxy-D-glucose
[^{18}F]FLT	3'-deoxy-3'-[^{18}F]fluorothymidine
[^{18}F]FMAU	1-(2'-deoxy-2'-[^{18}F]fluoro-1-β-D-arabinofuranosyl)-thymine
[^{18}F]SFB	N-succinimidyl-4-[^{18}F]fluorobenzoate
[^{3}H-methyl]TdR	[^{3}H-methyl]thymidine
[^{11}C]MET	[^{11}C]methyl-methionine
%ID/g	The percentage of injected dose per gram
BBN	Bombesin
BCM	Pancreatic β-cell mass
BFC	Bifunctional chelator
BLI	Bioluminescence Imaging
BSA	Bovine serum albumin
CNS	Central nervous system
CT	Computed Tomography
DCCT	The Diabetes Control and Complications Trial
DCM	Dichloromethane
DIEA	N,N-Diisopropylethylamine
L-DOPA	L-dihydrophenylalanine

DOTA	1,4,7,10-tetraazacyclododecane-1,4,7,10-tetraacetic acid
DMF	Dimethylformamide
DMSO	Dimethyl sulfoxide
DTBZ	Dihydrotetrabenazine
DTPA	Diethylenetriamine pentaacetic acid
DPP-IV	Dipeptidyl peptidase-IV
E.Coli	Escherichia coli
FI	Fluorescence Imaging
FITC	Fluorescein Isothiocyanate
FPGT	Fasting plasma glucose test
GLP-1	Glucagon-like Peptide-1
GLP-1R	Glucagon-like Peptide-1 receptor
GLUT2	Glucose transporter 2
HBTU	2-(1H-benzotriazole-l-yl)-1,1,3,3-tetramethyluronium hexafluorophosphate
HbA1c	Hemoglobin A1c
H&E stain	Hematoxylin and eosin stain
HI	Hyperinsulinism
HOBt	1-Hydroxybenzotriazole
HPLC	High performance liquid chromatography
IC_{50}	50% inhibitory concentration
ICSA	Islet cell surface antibody

Ig	Immunoglobulin
JDS	The Japan Diabetes Association
MRI	Magnetic Resonance Imaging
α-MSH	α-Melanocyte Stimulating Hormone
MMP	Matrix metalloproteinase
n.c.a.	Non-carrier-added
NT	Neurotensin
NK	Neurokinin
NSCLC	Non-small cell lung carcinoma
NMM	N-Methylmorpholine
NIDDK	National Institute of Diabetes and Digestive and Kidney Diseases
NEP	Neutral endopeptidase
NIS	Sodium iodide symporter
OGTT	Oral glucose tolerance test
OSEM	Ordered Subsets Expectation Maximization
PBS	Phosphate buffered saline
PET	Positron Emission Tomography
PyAOP	(7-Azabenzotriazol-1-yloxy)tripyrrolidinophosphonium hexafluorophosphate
RIP-1	Rat islet peptide 1
ROI	Regions of interest
SCA	Single-chain antibody

SCID	Severe combined immunodeficiency
SCLC	Small cell lung carcinoma
SIB	N-succinimidyl-3-iodobenzoate
SPECT	Single Photon Emission Computed Tomography
SPIC	N-succinimidyl-5-iodo-3-pyridinecarboxylate
SST	Somatostatin
STZ	Streptozotocin
SUR1	Sulfonylurea receptor
T1D	Type 1 diabetes
T2D	Type 2 diabetes
TFA	Trifluoroacetic acid
TSTU	*O*-(*N*-Succinimidyl)-*N*,*N*,*N*′,*N*′-tetramethyluronium tetrafluoroborate
UKPDS	The U.K. Prospective Diabetes Study
US	Ultrasound
VEGF	Vascular epithelial growth factor
VEGFR2	Vascular epithelial growth factor receptor 2
VIP	Vasoactive Intestinal Peptide
VMAT2	Vesicular monoamine transporter type 2

BIBLOGRAPHY

1. Wagenaar, D. J.; Weissleder, R.; Hengerer, A., Glossary of molecular imaging terminology. *Acad Radiol* **2001,** 8, (5), 409-20.
2. Weissleder, R.; Mahmood, U., Molecular imaging. *Radiology* **2001,** 219, (2), 316-33.
3. Specht, N. W.; Bauer, F. K.; Adams, R. M., Thyroid carcinoma; visualization of a distant osseous metastasis by scintiscanner; observations during I-131 therapy. *Am J Med* **1953,** 14, (6), 766-9.
4. Pennisi, E., Human genome. Finally, the book of life and instructions for navigating it. *Science (New York, N.Y* **2000,** 288, (5475), 2304-7.
5. Molecular Libraries and Imaging. http://nihroadmap.nih.gov/molecularlibraries/
6. Therasse, P.; Arbuck, S. G.; Eisenhauer, E. A.; Wanders, J.; Kaplan, R. S.; Rubinstein, L.; Verweij, J.; Van Glabbeke, M.; van Oosterom, A. T.; Christian, M. C.; Gwyther, S. G., New guidelines to evaluate the response to treatment in solid tumors. European Organization for Research and Treatment of Cancer, National Cancer Institute of the United States, National Cancer Institute of Canada. *J Natl Cancer Inst* **2000,** 92, (3), 205-16.
7. Birchard, K. R.; Hoang, J. K.; Herndon, J. E., Jr.; Patz, E. F., Jr., Early changes in tumor size in patients treated for advanced stage nonsmall cell lung cancer do not correlate with survival. *Cancer* **2009,** 115, (3), 581-6.
8. Morse, D. L.; Gillies, R. J., Molecular imaging and targeted therapies. *Biochem Pharmacol* **2010,** 80, (5), 731-8.
9. Pantaleo, M. A.; Nannini, M.; Lopci, E.; Castellucci, P.; Maleddu, A.; Lodi, F.; Nanni, C.; Allegri, V.; Astorino, M.; Brandi, G.; Di Battista, M.; Boschi, S.; Fanti, S.; Biasco, G., Molecular imaging and targeted therapies in oncology: new concepts in treatment response assessment. a collection of cases. *International journal of oncology* **2008,** 33, (3), 443-52.
10. Administration, F. a. D., *US Code of Federal Regulations 21 CFR*. Vol. 314.
11. Jager, P. L.; de Korte, M. A.; Lub-de Hooge, M. N.; van Waarde, A.; Koopmans, K. P.; Perik, P. J.; de Vries, E. G., Molecular imaging: what can be used today. *Cancer Imaging* **2005,** 5 Spec No A, S27-32.
12. Rohren, E. M.; Turkington, T. G.; Coleman, R. E., Clinical applications of PET in oncology. *Radiology* **2004,** 231, (2), 305-32.
13. Hunter, D. J.; Conaghan, P. G., Imaging outcomes and their role in determining outcomes in osteoarthritis and rheumatoid arthritis. *Curr Opin Rheumatol* **2006,** 18, (2), 157-62.
14. Lespessailles, E.; Chappard, C.; Bonnet, N.; Benhamou, C. L., Imaging techniques for evaluating bone microarchitecture. *Joint Bone Spine* **2006,** 73, (3), 254-61.
15. Seddon, B. M.; Workman, P., The role of functional and molecular imaging in cancer drug discovery and development. *Br J Radiol* **2003,** 76 Spec No 2, S128-38.

16. Hoit, B. D., New approaches to phenotypic analysis in adult mice. *J Mol Cell Cardiol* **2001,** 33, (1), 27-35.
17. Walrath, J. C.; Hawes, J. J.; Van Dyke, T.; Reilly, K. M., Genetically engineered mouse models in cancer research. *Adv Cancer Res* **2010,** 106, 113-64.
18. Tempany, C. M.; McNeil, B. J., Advances in biomedical imaging. *Jama* **2001,** 285, (5), 562-7.
19. Jaffer, F. A.; Weissleder, R., Seeing within: molecular imaging of the cardiovascular system. *Circ Res* **2004,** 94, (4), 433-45.
20. Blasberg, R. G.; Tjuvajev, J. G., Molecular-genetic imaging: current and future perspectives. *The Journal of clinical investigation* **2003,** 111, (11), 1620-9.
21. Choudhury, R. P.; Fuster, V.; Fayad, Z. A., Molecular, cellular and functional imaging of atherothrombosis. *Nat Rev Drug Discov* **2004,** 3, (11), 913-25.
22. Blankenberg, F. G.; Strauss, H. W., Nuclear medicine applications in molecular imaging: 2007 update. *Q J Nucl Med Mol Imaging* **2007,** 51, (2), 99-110.
23. Blankenberg, F. G.; Strauss, H. W., Nuclear medicine applications in molecular imaging. *J Magn Reson Imaging* **2002,** 16, (4), 352-61.
24. Weissleder, R.; Pittet, M. J., Imaging in the era of molecular oncology. *Nature* **2008,** 452, (7187), 580-9.
25. Jensen, J. A., Medical ultrasound imaging. *Prog Biophys Mol Biol* **2007,** 93, (1-3), 153-65.
26. Garcia, J. P., Jr.; Rosen, R. B., Anterior segment imaging: optical coherence tomography versus ultrasound biomicroscopy. *Ophthalmic Surg Lasers Imaging* **2008,** 39, (6), 476-84.
27. Phoon, C. K., Imaging tools for the developmental biologist: ultrasound biomicroscopy of mouse embryonic development. *Pediatr Res* **2006,** 60, (1), 14-21.
28. Weisbrod, D. J.; Pavlin, C. J.; Xu, W.; Simpson, E. R., Long-term follow-up of 42 patients with small ciliary body tumors with ultrasound biomicroscopy. *Am J Ophthalmol* **2010,** 149, (4), 616-22.
29. Furlow, B., Contrast-enhanced ultrasound. *Radiol Technol* **2009,** 80, (6), 547S-61S.
30. Laurent, S.; Vander Elst, L.; Muller, R. N., Lanthanide complexes for magnetic resonance and optical molecular imaging. *Q J Nucl Med Mol Imaging* **2009,** 53, (6), 586-603.
31. Gossuin, Y.; Gillis, P.; Hocq, A.; Vuong, Q. L.; Roch, A., Magnetic resonance relaxation properties of superparamagnetic particles. *Wiley Interdiscip Rev Nanomed Nanobiotechnol* **2009,** 1, (3), 299-310.
32. Vande Velde, G.; Baekelandt, V.; Dresselaers, T.; Himmelreich, U., Magnetic resonance imaging and spectroscopy methods for molecular imaging. *Q J Nucl Med Mol Imaging* **2009,** 53, (6), 565-85.
33. Glunde, K.; Artemov, D.; Penet, M. F.; Jacobs, M. A.; Bhujwalla, Z. M., Magnetic resonance spectroscopy in metabolic and molecular imaging and diagnosis of cancer. *Chemical reviews* **2010,** 110, (5), 3043-59.

34. Patterson, D. M.; Padhani, A. R.; Collins, D. J., Technology insight: water diffusion MRI--a potential new biomarker of response to cancer therapy. *Nat Clin Pract Oncol* **2008,** 5, (4), 220-33.
35. Harting, I.; Hartmann, M.; Bonsanto, M. M.; Sommer, C.; Sartor, K., Characterization of necrotic meningioma using diffusion MRI, perfusion MRI, and MR spectroscopy: case report and review of the literature. *Neuroradiology* **2004,** 46, (3), 189-93.
36. Kantarci, K., 1H magnetic resonance spectroscopy in dementia. *Br J Radiol* **2007,** 80 Spec No 2, S146-52.
37. Cox, I. J., Development and applications of in vivo clinical magnetic resonance spectroscopy. *Prog Biophys Mol Biol* **1996,** 65, (1-2), 45-81.
38. Herman, T., *Fundamentals of Computerized Tomography*. 2nd ed.; Academic Press: 2010.
39. Schambach, S. J.; Bag, S.; Schilling, L.; Groden, C.; Brockmann, M. A., Application of micro-CT in small animal imaging. *Methods* **2010,** 50, (1), 2-13.
40. Beckmann, N.; Kneuer, R.; Gremlich, H. U.; Karmouty-Quintana, H.; Ble, F. X.; Muller, M., In vivo mouse imaging and spectroscopy in drug discovery. *NMR Biomed* **2007,** 20, (3), 154-85.
41. Speck, U., Contrast agents: X-ray contrast agents and molecular imaging--a contradiction? *Handb Exp Pharmacol* **2008**, (185 Pt 1), 167-75.
42. Li, J.; Chaudhary, A.; Chmura, S. J.; Pelizzari, C.; Rajh, T.; Wietholt, C.; Kurtoglu, M.; Aydogan, B., A novel functional CT contrast agent for molecular imaging of cancer. *Phys Med Biol* **2010,** 55, (15), 4389-97.
43. Hutchins, G. D.; Miller, M. A.; Soon, V. C.; Receveur, T., Small animal PET imaging. *ILAR journal / National Research Council, Institute of Laboratory Animal Resources* **2008,** 49, (1), 54-65.
44. Budinger, T. F.; Derenzo, S. E.; Gullberg, G. T.; Greenberg, W. L.; Huesman, R. H., Emission computer assisted tomography with single-photon and positron annihilation photon emitters. *Journal of computer assisted tomography* **1977,** 1, (1), 131-45.
45. Okudan, B.; Smitherman, T. C., The value and throughput of rest Thallium-201/stress Technetium -99m sestamibi dual-isotope myocardial SPECT. *Anadolu Kardiyol Derg* **2004,** 4, (2), 161-8.
46. Berman, D. S.; Kiat, H.; Van Train, K.; Friedman, J. D.; Wang, F. P.; Germano, G., Dual-isotope myocardial perfusion SPECT with rest thallium-201 and stress Tc-99m sestamibi. *Cardiology clinics* **1994,** 12, (2), 261-70.
47. Spanoudaki, V. C.; Ziegler, S. I., PET & SPECT instrumentation. *Handb Exp Pharmacol* **2008**, (185 Pt 1), 53-74.
48. Shibuya, K.; Yoshida, E.; Nishikido, F.; Suzuki, T.; Tsuda, T.; Inadama, N.; Yamaya, T.; Murayama, H., Annihilation photon acollinearity in PET: volunteer and phantom FDG studies. *Phys Med Biol* **2007,** 52, (17), 5249-61.
49. Hickson, J., In vivo optical imaging: preclinical applications and considerations. *Urol Oncol* **2009,** 27, (3), 295-7.

50. Vooijs, M.; Jonkers, J.; Lyons, S.; Berns, A., Noninvasive imaging of spontaneous retinoblastoma pathway-dependent tumors in mice. *Cancer research* **2002,** 62, (6), 1862-7.
51. Townsend, D. W.; Beyer, T.; Blodgett, T. M., PET/CT scanners: a hardware approach to image fusion. *Seminars in nuclear medicine* **2003,** 33, (3), 193-204.
52. Bonnet, C. S.; Toth, E., Smart MR imaging agents relevant to potential neurologic applications. *AJNR Am J Neuroradiol* **2010,** 31, (3), 401-9.
53. Raymond, S. B.; Skoch, J.; Hills, I. D.; Nesterov, E. E.; Swager, T. M.; Bacskai, B. J., Smart optical probes for near-infrared fluorescence imaging of Alzheimer's disease pathology. *European journal of nuclear medicine and molecular imaging* **2008,** 35 Suppl 1, S93-8.
54. Serganova, I.; Mayer-Kukuck, P.; Huang, R.; Blasberg, R., Molecular imaging: reporter gene imaging. *Handb Exp Pharmacol* **2008**, (185 Pt 2), 167-223.
55. Vander Heiden, M. G.; Cantley, L. C.; Thompson, C. B., Understanding the Warburg effect: the metabolic requirements of cell proliferation. *Science (New York, N.Y* **2009,** 324, (5930), 1029-33.
56. Xiong, Q. F.; Chen, Y., Review: Deoxyglucose compounds labeled with isotopes different from 18-fuoride: is there a future in clinical practice? *Cancer biotherapy & radiopharmaceuticals* **2008,** 23, (3), 376-81.
57. Di Chiro, G., Positron emission tomography using [18F] fluorodeoxyglucose in brain tumors. A powerful diagnostic and prognostic tool. *Investigative radiology* **1987,** 22, (5), 360-71.
58. Kubota, K.; Matsuzawa, T.; Fujiwara, T.; Ito, M.; Hatazawa, J.; Ishiwata, K.; Iwata, R.; Ido, T., Differential diagnosis of lung tumor with positron emission tomography: a prospective study. *J Nucl Med* **1990,** 31, (12), 1927-32.
59. Hoh, C. K.; Hawkins, R. A.; Glaspy, J. A.; Dahlbom, M.; Tse, N. Y.; Hoffman, E. J.; Schiepers, C.; Choi, Y.; Rege, S.; Nitzsche, E.; et al., Cancer detection with whole-body PET using 2-[18F]fluoro-2-deoxy-D-glucose. *Journal of computer assisted tomography* **1993,** 17, (4), 582-9.
60. Smith, T. A., Mammalian hexokinases and their abnormal expression in cancer. *Br J Biomed Sci* **2000,** 57, (2), 170-8.
61. Smith, T. A., FDG uptake, tumour characteristics and response to therapy: a review. *Nuclear medicine communications* **1998,** 19, (2), 97-105.
62. Mac Manus, M. P.; Hicks, R. J., PET scanning in lung cancer: current status and future directions. *Seminars in surgical oncology* **2003,** 21, (3), 149-55.
63. Shreve, P. D.; Anzai, Y.; Wahl, R. L., Pitfalls in oncologic diagnosis with FDG PET imaging: physiologic and benign variants. *Radiographics* **1999,** 19, (1), 61-77; quiz 150-1.
64. Rubini, J. R.; Cronkite, E. P.; Bond, V. P.; Fliedner, T. M., The metabolism and fate of tritiated thymidine in man. *The Journal of clinical investigation* **1960,** 39, 909-18.
65. Christman, D.; Crawford, E. J.; Friedkin, M.; Wolf, A. P., Detection of DNA synthesis in intact organisms with positron-emitting (methyl- 11 C)thymidine.

Proceedings of the National Academy of Sciences of the United States of America **1972,** 69, (4), 988-92.
66. Sherley, J. L.; Kelly, T. J., Regulation of human thymidine kinase during the cell cycle. *J Biol Chem* **1988,** 263, (17), 8350-8.
67. van Waarde, A.; Cobben, D. C.; Suurmeijer, A. J.; Maas, B.; Vaalburg, W.; de Vries, E. F.; Jager, P. L.; Hoekstra, H. J.; Elsinga, P. H., Selectivity of 18F-FLT and 18F-FDG for differentiating tumor from inflammation in a rodent model. *J Nucl Med* **2004,** 45, (4), 695-700.
68. Jager, P. L.; Vaalburg, W.; Pruim, J.; de Vries, E. G.; Langen, K. J.; Piers, D. A., Radiolabeled amino acids: basic aspects and clinical applications in oncology. *J Nucl Med* **2001,** 42, (3), 432-45.
69. Glunde, K.; Ackerstaff, E.; Mori, N.; Jacobs, M. A.; Bhujwalla, Z. M., Choline phospholipid metabolism in cancer: consequences for molecular pharmaceutical interventions. *Mol Pharm* **2006,** 3, (5), 496-506.
70. Bouchelouche, K.; Oehr, P., Recent developments in urologic oncology: positron emission tomography molecular imaging. *Curr Opin Oncol* **2008,** 20, (3), 321-6.
71. Ferrer Albiach, C.; Conde Moreno, A.; Rodriguez Cordon, M.; Morillo Macias, V.; Bouche Babiloni, A.; Beato Tortajada, I.; Sanchez Iglesias, A.; Frances Munoz, A., Contribution of hypoxia-measuring molecular imaging techniques to radiotherapy planning and treatment. *Clin Transl Oncol* **2010,** 12, (1), 22-6.
72. Lee, S. T.; Scott, A. M., Hypoxia positron emission tomography imaging with 18f-fluoromisonidazole. *Seminars in nuclear medicine* **2007,** 37, (6), 451-61.
73. O'Donoghue, J. A.; Zanzonico, P.; Pugachev, A.; Wen, B.; Smith-Jones, P.; Cai, S.; Burnazi, E.; Finn, R. D.; Burgman, P.; Ruan, S.; Lewis, J. S.; Welch, M. J.; Ling, C. C.; Humm, J. L., Assessment of regional tumor hypoxia using 18F-fluoromisonidazole and 64Cu(II)-diacetyl-bis(N4-methylthiosemicarbazone) positron emission tomography: Comparative study featuring microPET imaging, Po2 probe measurement, autoradiography, and fluorescent microscopy in the R3327-AT and FaDu rat tumor models. *Int J Radiat Oncol Biol Phys* **2005,** 61, (5), 1493-502.
74. Matsumoto, K.; Szajek, L.; Krishna, M. C.; Cook, J. A.; Seidel, J.; Grimes, K.; Carson, J.; Sowers, A. L.; English, S.; Green, M. V.; Bacharach, S. L.; Eckelman, W. C.; Mitchell, J. B., The influence of tumor oxygenation on hypoxia imaging in murine squamous cell carcinoma using [64Cu]Cu-ATSM or [18F]Fluoromisonidazole positron emission tomography. *International journal of oncology* **2007,** 30, (4), 873-81.
75. Fujibayashi, Y.; Taniuchi, H.; Yonekura, Y.; Ohtani, H.; Konishi, J.; Yokoyama, A., Copper-62-ATSM: a new hypoxia imaging agent with high membrane permeability and low redox potential. *J Nucl Med* **1997,** 38, (7), 1155-60.
76. Obata, A.; Yoshimi, E.; Waki, A.; Lewis, J. S.; Oyama, N.; Welch, M. J.; Saji, H.; Yonekura, Y.; Fujibayashi, Y., Retention mechanism of hypoxia selective nuclear imaging/radiotherapeutic agent cu-diacetyl-bis(N4-methylthiosemicarbazone) (Cu-ATSM) in tumor cells. *Ann Nucl Med* **2001,** 15, (6), 499-504.

77. Dearling, J. L.; Lewis, J. S.; Mullen, G. E.; Welch, M. J.; Blower, P. J., Copper bis(thiosemicarbazone) complexes as hypoxia imaging agents: structure-activity relationships. *J Biol Inorg Chem* **2002,** 7, (3), 249-59.
78. Maurer, R. I.; Blower, P. J.; Dilworth, J. R.; Reynolds, C. A.; Zheng, Y.; Mullen, G. E., Studies on the mechanism of hypoxic selectivity in copper bis(thiosemicarbazone) radiopharmaceuticals. *Journal of medicinal chemistry* **2002,** 45, (7), 1420-31.
79. Yuan, H.; Schroeder, T.; Bowsher, J. E.; Hedlund, L. W.; Wong, T.; Dewhirst, M. W., Intertumoral differences in hypoxia selectivity of the PET imaging agent 64Cu(II)-diacetyl-bis(N4-methylthiosemicarbazone). *J Nucl Med* **2006,** 47, (6), 989-98.
80. Burgman, P.; O'Donoghue, J. A.; Lewis, J. S.; Welch, M. J.; Humm, J. L.; Ling, C. C., Cell line-dependent differences in uptake and retention of the hypoxia-selective nuclear imaging agent Cu-ATSM. *Nuclear medicine and biology* **2005,** 32, (6), 623-30.
81. Liu, J.; Hajibeigi, A.; Ren, G.; Lin, M.; Siyambalapitiyage, W.; Liu, Z.; Simpson, E.; Parkey, R. W.; Sun, X.; Oz, O. K., Retention of the radiotracers 64Cu-ATSM and 64Cu-PTSM in human and murine tumors is influenced by MDR1 protein expression. *J Nucl Med* **2009,** 50, (8), 1332-9.
82. Waerzeggers, Y.; Monfared, P.; Viel, T.; Winkeler, A.; Voges, J.; Jacobs, A. H., Methods to monitor gene therapy with molecular imaging. *Methods* **2009,** 48, (2), 146-60.
83. Haubner, R.; Avril, N.; Hantzopoulos, P. A.; Gansbacher, B.; Schwaiger, M., In vivo imaging of herpes simplex virus type 1 thymidine kinase gene expression: early kinetics of radiolabelled FIAU. *European journal of nuclear medicine* **2000,** 27, (3), 283-91.
84. Saito, Y.; Price, R. W.; Rottenberg, D. A.; Fox, J. J.; Su, T. L.; Watanabe, K. A.; Philips, F. S., Quantitative autoradiographic mapping of herpes simplex virus encephalitis with a radiolabeled antiviral drug. *Science (New York, N.Y* **1982,** 217, (4565), 1151-3.
85. Saito, Y.; Rubenstein, R.; Price, R. W.; Fox, J. J.; Watanabe, K. A., Diagnostic imaging of herpes simplex virus encephalitis using a radiolabeled antiviral drug: autoradiographic assessment in an animal model. *Ann Neurol* **1984,** 15, (6), 548-58.
86. Chen, I. Y.; Wu, J. C.; Min, J. J.; Sundaresan, G.; Lewis, X.; Liang, Q.; Herschman, H. R.; Gambhir, S. S., Micro-positron emission tomography imaging of cardiac gene expression in rats using bicistronic adenoviral vector-mediated gene delivery. *Circulation* **2004,** 109, (11), 1415-20.
87. Boot, E.; Booij, J.; Zinkstok, J.; de Haan, L.; Linszen, D.; Baas, F.; van Amelsvoort, T., Striatal D2 receptor binding in 22q11 deletion syndrome: an [123I]IBZM SPECT study. *J Psychopharmacol* **2009**.
88. Liang, Q.; Satyamurthy, N.; Barrio, J. R.; Toyokuni, T.; Phelps, M. P.; Gambhir, S. S.; Herschman, H. R., Noninvasive, quantitative imaging in living animals of a

mutant dopamine D2 receptor reporter gene in which ligand binding is uncoupled from signal transduction. *Gene Ther* **2001,** 8, (19), 1490-8.
89. Huang, M.; Batra, R. K.; Kogai, T.; Lin, Y. Q.; Hershman, J. M.; Lichtenstein, A.; Sharma, S.; Zhu, L. X.; Brent, G. A.; Dubinett, S. M., Ectopic expression of the thyroperoxidase gene augments radioiodide uptake and retention mediated by the sodium iodide symporter in non-small cell lung cancer. *Cancer Gene Ther* **2001,** 8, (8), 612-8.
90. Carrasco, N., Iodide transport in the thyroid gland. *Biochim Biophys Acta* **1993,** 1154, (1), 65-82.
91. Okarvi, S. M., Peptide-based radiopharmaceuticals and cytotoxic conjugates: potential tools against cancer. *Cancer treatment reviews* **2008,** 34, (1), 13-26.
92. Okarvi, S. M., Peptide-based radiopharmaceuticals: future tools for diagnostic imaging of cancers and other diseases. *Medicinal research reviews* **2004,** 24, (3), 357-97.
93. Lang, M.; Beck-Sickinger, A. G., Structure-activity relationship studies: methods and ligand design for G-protein coupled peptide receptors. *Curr Protein Pept Sci* **2006,** 7, (4), 335-53.
94. Noti, C.; Seeberger, P. H., Chemical approaches to define the structure-activity relationship of heparin-like glycosaminoglycans. *Chem Biol* **2005,** 12, (7), 731-56.
95. Cowell, S. M.; Balse-Srinivasan, P. M.; Ahn, J. M.; Hruby, V. J., Design and synthesis of peptide antagonists and inverse agonists for G protein-coupled receptors. *Methods Enzymol* **2002,** 343, 49-72.
96. Brazeau, P.; Vale, W.; Burgus, R.; Ling, N.; Butcher, M.; Rivier, J.; Guillemin, R., Hypothalamic polypeptide that inhibits the secretion of immunoreactive pituitary growth hormone. *Science (New York, N.Y* **1973,** 179, (68), 77-9.
97. Reichlin, S., Somatostatin. *The New England journal of medicine* **1983,** 309, (24), 1495-501.
98. Mezi, S.; Primi, F.; Orsi, E.; Capoccetti, F.; Scopinaro, F.; Schillaci, O., Somatostatin receptor scintigraphy in metastatic breast cancer patients. *Oncology reports* **2005,** 13, (1), 31-5.
99. Van Den Bossche, B.; D'Haeninck, E.; De Vos, F.; Dierckx, R. A.; Van Belle, S.; Bracke, M.; Van de Wiele, C., Oestrogen-mediated regulation of somatostatin receptor expression in human breast cancer cell lines assessed with 99mTc-depreotide. *European journal of nuclear medicine and molecular imaging* **2004,** 31, (7), 1022-30.
100. Baath, M.; Kolbeck, K. G.; Danielsson, R., Somatostatin receptor scintigraphy with 99mTc-Depreotide (NeoSpect) in discriminating between malignant and benign lesions in the diagnosis of lung cancer: a pilot study. *Acta Radiol* **2004,** 45, (8), 833-9.
101. Skanberg, J.; Ahlman, H.; Benjegard, S. A.; Fjalling, M.; Forssell-Aronsson, E. B.; Hashemi, S. H.; Nilsson, O.; Suurkula, M.; Jansson, S., Indium-111-octreotide scintigraphy, intraoperative gamma-detector localisation and somatostatin receptor expression in primary human breast cancer. *Breast cancer research and treatment* **2002,** 74, (2), 101-11.

102. Maini, C. L.; Tofani, A.; Venturo, I.; Pigorini, F.; Sciuto, R.; Semprebene, A.; Boni, S.; Giunta, S.; Lopez, M., Somatostatin receptor imaging in small cell lung cancer using 111In-DTPA-octreotide: a preliminary study. *Nuclear medicine communications* **1993,** 14, (11), 962-8.
103. Li, M.; Wang, X.; Li, W.; Li, F.; Yang, H.; Wang, H.; Brunicardi, F. C.; Chen, C.; Yao, Q.; Fisher, W. E., Somatostatin receptor-1 induces cell cycle arrest and inhibits tumor growth in pancreatic cancer. *Cancer science* **2008,** 99, (11), 2218-23.
104. Li, M.; Becnel, L. S.; Li, W.; Fisher, W. E.; Chen, C.; Yao, Q., Signal transduction in human pancreatic cancer: roles of transforming growth factor beta, somatostatin receptors, and other signal intermediates. *Archivum immunologiae et therapiae experimentalis* **2005,** 53, (5), 381-7.
105. Breeman, W. A.; de Jong, M.; Kwekkeboom, D. J.; Valkema, R.; Bakker, W. H.; Kooij, P. P.; Visser, T. J.; Krenning, E. P., Somatostatin receptor-mediated imaging and therapy: basic science, current knowledge, limitations and future perspectives. *European journal of nuclear medicine* **2001,** 28, (9), 1421-9.
106. Vallabhajosula, S.; Moyer, B. R.; Lister-James, J.; McBride, B. J.; Lipszyc, H.; Lee, H.; Bastidas, D.; Dean, R. T., Preclinical evaluation of technetium-99m-labeled somatostatin receptor-binding peptides. *J Nucl Med* **1996,** 37, (6), 1016-22.
107. Pawlikowski, M.; Melen-Mucha, G., Somatostatin analogs - from new molecules to new applications. *Curr Opin Pharmacol* **2004,** 4, (6), 608-13.
108. Pool, S. E.; Krenning, E. P.; Koning, G. A.; van Eijck, C. H.; Teunissen, J. J.; Kam, B.; Valkema, R.; Kwekkeboom, D. J.; de Jong, M., Preclinical and clinical studies of peptide receptor radionuclide therapy. *Seminars in nuclear medicine* **2010,** 40, (3), 209-18.
109. Maecke, H. R.; Hofmann, M.; Haberkorn, U., (68)Ga-labeled peptides in tumor imaging. *J Nucl Med* **2005,** 46 Suppl 1, 172S-8S.
110. Kwekkeboom, D. J.; Mueller-Brand, J.; Paganelli, G.; Anthony, L. B.; Pauwels, S.; Kvols, L. K.; O'Dorisio T, M.; Valkema, R.; Bodei, L.; Chinol, M.; Maecke, H. R.; Krenning, E. P., Overview of results of peptide receptor radionuclide therapy with 3 radiolabeled somatostatin analogs. *J Nucl Med* **2005,** 46 Suppl 1, 62S-6S.
111. Kwekkeboom, D. J.; Bakker, W. H.; Kooij, P. P.; Konijnenberg, M. W.; Srinivasan, A.; Erion, J. L.; Schmidt, M. A.; Bugaj, J. L.; de Jong, M.; Krenning, E. P., [177Lu-DOTAOTyr3]octreotate: comparison with [111In-DTPAo]octreotide in patients. *European journal of nuclear medicine* **2001,** 28, (9), 1319-25.
112. Wester, H. J.; Schottelius, M.; Scheidhauer, K.; Meisetschlager, G.; Herz, M.; Rau, F. C.; Reubi, J. C.; Schwaiger, M., PET imaging of somatostatin receptors: design, synthesis and preclinical evaluation of a novel 18F-labelled, carbohydrated analogue of octreotide. *European journal of nuclear medicine and molecular imaging* **2003,** 30, (1), 117-22.
113. Schottelius, M.; Poethko, T.; Herz, M.; Reubi, J. C.; Kessler, H.; Schwaiger, M.; Wester, H. J., First (18)F-labeled tracer suitable for routine clinical imaging of sst

receptor-expressing tumors using positron emission tomography. *Clin Cancer Res* **2004,** 10, (11), 3593-606.
114. Schottelius, M.; Reubi, J. C.; Eltschinger, V.; Schwaiger, M.; Wester, H. J., N-terminal sugar conjugation and C-terminal Thr-for-Thr(ol) exchange in radioiodinated Tyr3-octreotide: effect on cellular ligand trafficking in vitro and tumor accumulation in vivo. *Journal of medicinal chemistry* **2005,** 48, (8), 2778-89.
115. Cornelio, D. B.; Roesler, R.; Schwartsmann, G., Gastrin-releasing peptide receptor as a molecular target in experimental anticancer therapy. *Ann Oncol* **2007,** 18, (9), 1457-66.
116. Smith, C. J.; Volkert, W. A.; Hoffman, T. J., Radiolabeled peptide conjugates for targeting of the bombesin receptor superfamily subtypes. *Nuclear medicine and biology* **2005,** 32, (7), 733-40.
117. Anastasi, A.; Erspamer, V.; Bucci, M., Isolation and structure of bombesin and alytesin, 2 analogous active peptides from the skin of the European amphibians Bombina and Alytes. *Experientia* **1971,** 27, (2), 166-7.
118. Santos-Cuevas, C. L.; Ferro-Flores, G.; Arteaga de Murphy, C.; Pichardo-Romero, P. A., Targeted imaging of gastrin-releasing peptide receptors with 99mTc-EDDA/HYNIC-[Lys3]-bombesin: biokinetics and dosimetry in women. *Nuclear medicine communications* **2008,** 29, (8), 741-7.
119. Garrison, J. C.; Rold, T. L.; Sieckman, G. L.; Naz, F.; Sublett, S. V.; Figueroa, S. D.; Volkert, W. A.; Hoffman, T. J., Evaluation of the pharmacokinetic effects of various linking group using the 111In-DOTA-X-BBN(7-14)NH2 structural paradigm in a prostate cancer model. *Bioconjugate chemistry* **2008,** 19, (9), 1803-12.
120. Chen, X.; Park, R.; Hou, Y.; Tohme, M.; Shahinian, A. H.; Bading, J. R.; Conti, P. S., microPET and autoradiographic imaging of GRP receptor expression with 64Cu-DOTA-[Lys3]bombesin in human prostate adenocarcinoma xenografts. *J Nucl Med* **2004,** 45, (8), 1390-7.
121. Zhang, X.; Cai, W.; Cao, F.; Schreibmann, E.; Wu, Y.; Wu, J. C.; Xing, L.; Chen, X., 18F-labeled bombesin analogs for targeting GRP receptor-expressing prostate cancer. *J Nucl Med* **2006,** 47, (3), 492-501.
122. Yang, Y. S.; Zhang, X.; Xiong, Z.; Chen, X., Comparative in vitro and in vivo evaluation of two 64Cu-labeled bombesin analogs in a mouse model of human prostate adenocarcinoma. *Nuclear medicine and biology* **2006,** 33, (3), 371-80.
123. Breeman, W. A.; de Jong, M.; Erion, J. L.; Bugaj, J. E.; Srinivasan, A.; Bernard, B. F.; Kwekkeboom, D. J.; Visser, T. J.; Krenning, E. P., Preclinical comparison of (111)In-labeled DTPA- or DOTA-bombesin analogs for receptor-targeted scintigraphy and radionuclide therapy. *J Nucl Med* **2002,** 43, (12), 1650-6.
124. De Visser, M.; Van Weerden, W. M.; De Ridder, C. M.; Reneman, S.; Wildeman, N.; Melis, M.; Krenning, E.; De Jong, M., Androgen regulation of GRP receptor-expression in human prostate tumor xenografts. *J Nucl Med* **2005,** 46, 396.

125. Brooks, P. C.; Clark, R. A.; Cheresh, D. A., Requirement of vascular integrin alpha v beta 3 for angiogenesis. *Science (New York, N.Y* **1994,** 264, (5158), 569-71.
126. Eliceiri, B. P.; Cheresh, D. A., The role of alphav integrins during angiogenesis: insights into potential mechanisms of action and clinical development. *The Journal of clinical investigation* **1999,** 103, (9), 1227-30.
127. Cheresh, D. A., Structure, function and biological properties of integrin alpha v beta 3 on human melanoma cells. *Cancer Metastasis Rev* **1991,** 10, (1), 3-10.
128. van Hagen, P. M.; Breeman, W. A.; Bernard, H. F.; Schaar, M.; Mooij, C. M.; Srinivasan, A.; Schmidt, M. A.; Krenning, E. P.; de Jong, M., Evaluation of a radiolabelled cyclic DTPA-RGD analogue for tumour imaging and radionuclide therapy. *International journal of cancer* **2000,** 90, (4), 186-98.
129. Ferl, G. Z.; Dumont, R. A.; Hildebrandt, I. J.; Armijo, A.; Haubner, R.; Reischl, G.; Su, H.; Weber, W. A.; Huang, S. C., Derivation of a compartmental model for quantifying 64Cu-DOTA-RGD kinetics in tumor-bearing mice. *J Nucl Med* **2009,** 50, (2), 250-8.
130. Beer, A. J.; Niemeyer, M.; Carlsen, J.; Sarbia, M.; Nahrig, J.; Watzlowik, P.; Wester, H. J.; Harbeck, N.; Schwaiger, M., Patterns of alphavbeta3 expression in primary and metastatic human breast cancer as shown by 18F-Galacto-RGD PET. *J Nucl Med* **2008,** 49, (2), 255-9.
131. Poethko, T.; Schottelius, M.; Thumshirn, G.; Herz, M.; Haubner, R.; Henriksen, G., Chemoselective pre-conjugate radiohalogenation of unprotected mono- and multimeric peptides via oxime formation. *Radiochimica Acta* **2004,** 92, 317-327.
132. Baggio, L. L.; Drucker, D. J., Biology of incretins: GLP-1 and GIP. *Gastroenterology* **2007,** 132, (6), 2131-57.
133. Tornehave, D.; Kristensen, P.; Romer, J.; Knudsen, L. B.; Heller, R. S., Expression of the GLP-1 receptor in mouse, rat, and human pancreas. *J Histochem Cytochem* **2008,** 56, (9), 841-51.
134. Wild, D.; Behe, M.; Wicki, A.; Storch, D.; Waser, B.; Gotthardt, M.; Keil, B.; Christofori, G.; Reubi, J. C.; Macke, H. R., [Lys40(Ahx-DTPA-111In)NH2]exendin-4, a very promising ligand for glucagon-like peptide-1 (GLP-1) receptor targeting. *J Nucl Med* **2006,** 47, (12), 2025-33.
135. Brom, M.; Oyen, W. J.; Joosten, L.; Gotthardt, M.; Boerman, O. C., (68)Ga-labelled exendin-3, a new agent for the detection of insulinomas with PET. *European journal of nuclear medicine and molecular imaging* **2010**.
136. Wild, D.; Macke, H.; Christ, E.; Gloor, B.; Reubi, J. C., Glucagon-like Peptide 1-Receptor Scans to Localize Occult Insulinomas. *The New England journal of medicine* **2008,** 359, (7), 766-768.
137. Favaro, E.; Amadori, A.; Indraccolo, S., Cellular interactions in the vascular niche: implications in the regulation of tumor dormancy. *Apmis* **2008,** 116, (7-8), 648-59.
138. Al-Hajj, M.; Clarke, M. F., Self-renewal and solid tumor stem cells. *Oncogene* **2004,** 23, (43), 7274-82.

139. Fidler, I. J., Critical determinants of cancer metastasis: rationale for therapy. *Cancer chemotherapy and pharmacology* **1999,** 43 Suppl, S3-10.
140. de Koning, E. J.; Bonner-Weir, S.; Rabelink, T. J., Preservation of beta-cell function by targeting beta-cell mass. *Trends in pharmacological sciences* **2008,** 29, (4), 218-27.
141. Kjems, L. L.; Kirby, B. M.; Welsh, E. M.; Veldhuis, J. D.; Straume, M.; McIntyre, S. S.; Yang, D.; Lefebvre, P.; Butler, P. C., Decrease in beta-cell mass leads to impaired pulsatile insulin secretion, reduced postprandial hepatic insulin clearance, and relative hyperglucagonemia in the minipig. *Diabetes* **2001,** 50, (9), 2001-12.
142. Kendall, D. M.; Sutherland, D. E.; Najarian, J. S.; Goetz, F. C.; Robertson, R. P., Effects of hemipancreatectomy on insulin secretion and glucose tolerance in healthy humans. *The New England journal of medicine* **1990,** 322, (13), 898-903.
143. Goodner, C. J.; Koerker, D. J.; Weigle, D. S.; McCulloch, D. K., Decreased insulin- and glucagon-pulse amplitude accompanying beta-cell deficiency induced by streptozocin in baboons. *Diabetes* **1989,** 38, (7), 925-31.
144. Jemal, A.; Siegel, R.; Ward, E.; Hao, Y.; Xu, J.; Thun, M. J., Cancer statistics, 2009. *CA: a cancer journal for clinicians* **2009,** 59, (4), 225-49.
145. Collins, L. G.; Haines, C.; Perkel, R.; Enck, R. E., Lung cancer: diagnosis and management. *Am Fam Physician* **2007,** 75, (1), 56-63.
146. Nyberg, F.; Pershagen, G., Passive smoking and lung cancer. Accumulated evidence on lung cancer and environmental tobacco smoke. *BMJ* **1998,** 317, (7154), 347-8; author reply 348.
147. Hackshaw, A. K.; Law, M. R.; Wald, N. J., The accumulated evidence on lung cancer and environmental tobacco smoke. *BMJ* **1997,** 315, (7114), 980-8.
148. Catelinois, O.; Rogel, A.; Laurier, D.; Billon, S.; Hemon, D.; Verger, P.; Tirmarche, M., Lung cancer attributable to indoor radon exposure in france: impact of the risk models and uncertainty analysis. *Environ Health Perspect* **2006,** 114, (9), 1361-6.
149. O'Reilly, K. M.; McLaughlin, A. M.; Beckett, W. S.; Sime, P. J., Asbestos-related lung disease. *Am Fam Physician* **2007,** 75, (5), 683-8.
150. Coyle, Y. M.; Minahjuddin, A. T.; Hynan, L. S.; Minna, J. D., An ecological study of the association of metal air pollutants with lung cancer incidence in Texas. *J Thorac Oncol* **2006,** 1, (7), 654-61.
151. Gledhill, A.; Bates, C.; Henderson, D.; DaCosta, P.; Thomas, G., Sputum cytology: a limited role. *J Clin Pathol* **1997,** 50, (7), 566-8.
152. Truong, L. D.; Underwood, R. D.; Greenberg, S. D.; McLarty, J. W., Diagnosis and typing of lung carcinomas by cytopathologic methods. A review of 108 cases. *Acta Cytol* **1985,** 29, (3), 379-84.
153. Tanaka, T.; Yamamoto, M.; Tamura, T.; Moritani, Y.; Miyai, M.; Hiraki, S.; Ohnoshi, T.; Kimura, I., Cytologic and histologic correlation in primary lung cancer. A study of 154 cases with resectable tumors. *Acta Cytol* **1985,** 29, (1), 49-56.

154. Erozan, Y. S.; Frost, J. K., Cytopathologic diagnosis of cancer in pulmonary material: a critical histopathologic correlation. *Acta Cytol* **1970,** 14, (9), 560-5.
155. Arroliga, A. C.; Matthay, R. A., The role of bronchoscopy in lung cancer. *Clinics in chest medicine* **1993,** 14, (1), 87-98.
156. Mazzone, P.; Jain, P.; Arroliga, A. C.; Matthay, R. A., Bronchoscopy and needle biopsy techniques for diagnosis and staging of lung cancer. *Clinics in chest medicine* **2002,** 23, (1), 137-58, ix.
157. Silvestri, G. A.; Gould, M. K.; Margolis, M. L.; Tanoue, L. T.; McCrory, D.; Toloza, E.; Detterbeck, F., Noninvasive staging of non-small cell lung cancer: ACCP evidenced-based clinical practice guidelines (2nd edition). *Chest* **2007,** 132, (3 Suppl), 178S-201S.
158. McLoud, T. C.; Westcott, J.; Davis, S. D.; Fleishon, H.; Gefter, W. B.; Henschke, C. I.; Pugatch, R. D.; Sostman, H. D.; Tocino, I.; White, C. S.; Yankelevitz, D.; Bode, F. R., Staging of bronchogenic carcinoma, non-small cell lung carcinoma. American College of Radiology. ACR Appropriateness Criteria. *Radiology* **2000,** 215 Suppl, 611-9.
159. Bach, P. B.; Jett, J. R.; Pastorino, U.; Tockman, M. S.; Swensen, S. J.; Begg, C. B., Computed tomography screening and lung cancer outcomes. *Jama* **2007,** 297, (9), 953-61.
160. Swensen, S. J.; Jett, J. R.; Hartman, T. E.; Midthun, D. E.; Mandrekar, S. J.; Hillman, S. L.; Sykes, A. M.; Aughenbaugh, G. L.; Bungum, A. O.; Allen, K. L., CT screening for lung cancer: five-year prospective experience. *Radiology* **2005,** 235, (1), 259-65.
161. Wiemker, R.; Rogalla, P.; Blaffert, T.; Sifri, D.; Hay, O.; Shah, E.; Truyen, R.; Fleiter, T., Aspects of computer-aided detection (CAD) and volumetry of pulmonary nodules using multislice CT. *Br J Radiol* **2005,** 78 Spec No 1, S46-56.
162. Marchiano, A.; Calabro, E.; Civelli, E.; Di Tolla, G.; Frigerio, L. F.; Morosi, C.; Tafaro, F.; Ferri, E.; Sverzellati, N.; Camerini, T.; Mariani, L.; Lo Vullo, S.; Pastorino, U., Pulmonary nodules: volume repeatability at multidetector CT lung cancer screening. *Radiology* **2009,** 251, (3), 919-25.
163. Wright, C. D.; Mathisen, D. J., Superior sulcus tumors. *Curr Treat Options Oncol* **2001,** 2, (1), 43-9.
164. Urbach, H., MRI of long-term epilepsy-associated tumors. *Seminars in ultrasound, CT, and MR* **2008,** 29, (1), 40-6.
165. Godelman, A.; Haramati, L. B., MR imaging in diagnosis and staging of pulmonary carcinoma. *Magn Reson Imaging Clin N Am* **2008,** 16, (2), 309-17, ix.
166. D'Addario, G.; Felip, E., Non-small-cell lung cancer: ESMO clinical recommendations for diagnosis, treatment and follow-up. *Ann Oncol* **2009,** 20 Suppl 4, 68-70.
167. Nomori, H.; Watanabe, K.; Ohtsuka, T.; Naruke, T.; Suemasu, K.; Uno, K., Evaluation of F-18 fluorodeoxyglucose (FDG) PET scanning for pulmonary nodules less than 3 cm in diameter, with special reference to the CT images. *Lung Cancer* **2004,** 45, (1), 19-27.

168. Port, J. L.; Andrade, R. S.; Levin, M. A.; Korst, R. J.; Lee, P. C.; Becker, D. E.; Altorki, N. K., Positron emission tomographic scanning in the diagnosis and staging of non-small cell lung cancer 2 cm in size or less. *J Thorac Cardiovasc Surg* **2005,** 130, (6), 1611-5.
169. Yi, C. A.; Lee, K. S.; Kim, B. T.; Shim, S. S.; Chung, M. J.; Sung, Y. M.; Jeong, S. Y., Efficacy of helical dynamic CT versus integrated PET/CT for detection of mediastinal nodal metastasis in non-small cell lung cancer. *Ajr* **2007,** 188, (2), 318-25.
170. Devaraj, A.; Cook, G. J.; Hansell, D. M., PET/CT in non-small cell lung cancer staging-promises and problems. *Clinical radiology* **2007,** 62, (2), 97-108.
171. Bruzzi, J. F.; Munden, R. F., PET/CT imaging of lung cancer. *Journal of thoracic imaging* **2006,** 21, (2), 123-36.
172. Martin, S. M.; O'Donnell, R. T.; Kukis, D. L.; Abbey, C. K.; McKnight, H.; Sutcliffe, J. L.; Tuscano, J. M., Imaging and pharmacokinetics of (64)Cu-DOTA-HB22.7 administered by intravenous, intraperitoneal, or subcutaneous injection to mice bearing non-Hodgkin's lymphoma xenografts. *Mol Imaging Biol* **2009,** 11, (2), 79-87.
173. Hausner, S. H.; Kukis, D. L.; Gagnon, M. K.; Stanecki, C. E.; Ferdani, R.; Marshall, J. F.; Anderson, C. J.; Sutcliffe, J. L., Evaluation of [64Cu]Cu-DOTA and [64Cu]Cu-CB-TE2A chelates for targeted positron emission tomography with an alphavbeta6-specific peptide. *Mol Imaging* **2009,** 8, (2), 111-21.
174. Hausner, S. H.; Abbey, C. K.; Bold, R. J.; Gagnon, M. K.; Marik, J.; Marshall, J. F.; Stanecki, C. E.; Sutcliffe, J. L., Targeted in vivo imaging of integrin alphavbeta6 with an improved radiotracer and its relevance in a pancreatic tumor model. *Cancer Res* **2009,** 69, (14), 5843-50.
175. Hausner, S. H.; DiCara, D.; Marik, J.; Marshall, J. F.; Sutcliffe, J. L., Use of a peptide derived from foot-and-mouth disease virus for the noninvasive imaging of human cancer: generation and evaluation of 4-[18F]fluorobenzoyl A20FMDV2 for in vivo imaging of integrin alphavbeta6 expression with positron emission tomography. *Cancer Res* **2007,** 67, (16), 7833-40.
176. Elayadi, A. N.; Samli, K. N.; Prudkin, L.; Liu, Y. H.; Bian, A.; Xie, X. J.; Wistuba, II; Roth, J. A.; McGuire, M. J.; Brown, K. C., A peptide selected by biopanning identifies the integrin alphavbeta6 as a prognostic biomarker for nonsmall cell lung cancer. *Cancer research* **2007,** 67, (12), 5889-95.
177. Bates, R. C.; Bellovin, D. I.; Brown, C.; Maynard, E.; Wu, B.; Kawakatsu, H.; Sheppard, D.; Oettgen, P.; Mercurio, A. M., Transcriptional activation of integrin β6 during the epithelial-mesenchymal transition defines a novel prognostic indicator of aggressive colon cancer. *J. Clin. Invest.* **2005,** 115, 339-347.
178. Ahmed, N.; Riley, C.; Rice, G. E.; Quinn, M. A.; Baker, M. S., $\alpha_v\beta_6$ Integrin- A marker for the malignant potential of epithelial ovarian cancer. *J. Histochem.Cytochem.* **2002,** 50, (10), 1371-1379.
179. Ahmed, N.; Pansino, F.; Clyde, R.; Murthi, P.; Quinn, M. A.; Rice, G. E.; Agrez, M.; Mok, S.; Baker, M. S., Overexpression of αvβ6 integrin in serous epithelial

ovarian cancer regulates extracellular matrix degradtion via plasminogen activation cascade. *Carcinogenesis* **2002,** 23, 237-244.
180. Thomas, G. J.; Poomsawat, S.; Lewis, M. P.; Hart, I. R.; Speight, P. M.; Marshall, J. F., $\alpha_v\beta_6$ Integrin upregulates matrix metalloproteinase 9 and promotes migration of normal oral keratinocytes. *J. Invest. Derm.* **2001,** 116, 898-904.
181. Thomas, G. J.; Lewis, M. P.; Whawell, S. A.; Russell, A.; Sheppard, D.; Hart, I. R.; Speight, P. M.; Marshall, J. F., Expression of the $\alpha_v\beta_6$ integrin promotes migration and invasion in squamous carcinoma cells. *J. Invest. Derm.* **2001,** 117, (1), 67-73.
182. Thomas, G. J.; Lewis, M. P.; Hart, I. R.; Marshall, J. F.; Speight, P. M., $\alpha_v\beta_6$ integrin promotes invasion of squamous carcinoma cells through up-regulation of matrix metalloproteinase-9. *Int. J. Cancer* **2001,** 92, 641-650.
183. Agrez, M.; Gu, X.; Turton, J.; Meldrum, C.; Niu, J.; Antalis, T.; Howard, E. W., The $\alpha_v\beta_6$ integrin induces gelatinase secretion in colon cancer cells. *Int. J. Cancer* **1999,** 81, 90-97.
184. Breuss, J. M.; Gillett, N.; Lu, L.; Sheppard, D.; Pytela, R., Restricted distribution of integrin ß6 mRNA in primate epithelial tissues. *J Histochem Cytochem* **1993,** 41, (10), 1521-1527.
185. Hazelbag, S.; Kenter, G. G.; Gorter, A.; Dreef, E. J.; Koopman, L. A.; Violette, S. M.; Weinreb, P. H.; Fleuren, G. J., Overexpression of the alpha v beta 6 integrin in cervical squamous cell carcinoma is a prognostic factor for decreased survival. *The Journal of pathology* **2007,** 212, (3), 316-24.
186. Oyama, T.; Sykes, K. F.; Samli, K. N.; Minna, J. D.; Johnston, S. A.; Brown, K. C., Isolation of lung tumor specific peptides from a random peptide library: generation of diagnostic and cell-targeting reagents. *Cancer Lett.* **2003,** 202, 219-230.
187. Li, S.; McGuire, M. J.; Lin, M.; Liu, Y. H.; Oyama, T.; Sun, X.; Brown, K. C., Synthesis and characterization of a high-affinity {alpha}v{beta}6-specific ligand for in vitro and in vivo applications. *Molecular cancer therapeutics* **2009**.
188. Gallagher, S. E., *Beta Cells: Functions, Pathology and Research*. 4th ed.; NOVA publisher: 2010.
189. Kim, M. S.; Polychronakos, C., Immunogenetics of type 1 diabetes. *Hormone research* **2005,** 64, (4), 180-8.
190. Steele, C.; Hagopian, W. A.; Gitelman, S.; Masharani, U.; Cavaghan, M.; Rother, K. I.; Donaldson, D.; Harlan, D. M.; Bluestone, J.; Herold, K. C., Insulin secretion in type 1 diabetes. *Diabetes* **2004,** 53, (2), 426-33.
191. Rolandsson, O.; Hagg, E.; Hampe, C.; Sullivan, E. P., Jr.; Nilsson, M.; Jansson, G.; Hallmans, G.; Lernmark, A., Glutamate decarboxylase (GAD65) and tyrosine phosphatase-like protein (IA-2) autoantibodies index in a regional population is related to glucose intolerance and body mass index. *Diabetologia* **1999,** 42, (5), 555-9.
192. Ko, I. Y.; Ihm, S. H.; Yoon, J. W., Studies on autoimmunity for initiation of beta-cell destruction. VIII. Pancreatic beta-cell dependent autoantibody to a 38

kilodalton protein precedes the clinical onset of diabetes in BB rats. *Diabetologia* **1991,** 34, (8), 548-54.
193. Horn, G. T.; Bugawan, T. L.; Long, C. M.; Erlich, H. A., Allelic sequence variation of the HLA-DQ loci: relationship to serology and to insulin-dependent diabetes susceptibility. *Proceedings of the National Academy of Sciences of the United States of America* **1988,** 85, (16), 6012-6.
194. Todd, J. A.; Bain, S. C., A practical approach to identification of susceptibility genes for IDDM. *Diabetes* **1992,** 41, (9), 1029-34.
195. Segall, M., HLA and genetics of IDDM. Holism vs. reductionism? *Diabetes* **1988,** 37, (8), 1005-8.
196. Sheehy, M. J.; Scharf, S. J.; Rowe, J. R.; Neme de Gimenez, M. H.; Meske, L. M.; Erlich, H. A.; Nepom, B. S., A diabetes-susceptible HLA haplotype is best defined by a combination of HLA-DR and -DQ alleles. *The Journal of clinical investigation* **1989,** 83, (3), 830-5.
197. Barnett, A. H.; Eff, C.; Leslie, R. D.; Pyke, D. A., Diabetes in identical twins. A study of 200 pairs. *Diabetologia* **1981,** 20, (2), 87-93.
198. Jun, H. S.; Yoon, J. W., A new look at viruses in type 1 diabetes. *Diabetes/metabolism research and reviews* **2003,** 19, (1), 8-31.
199. Bergman, R. N.; Phillips, L. S.; Cobelli, C., Physiologic evaluation of factors controlling glucose tolerance in man: measurement of insulin sensitivity and beta-cell glucose sensitivity from the response to intravenous glucose. *The Journal of clinical investigation* **1981,** 68, (6), 1456-67.
200. Qiao, Q.; Nyamdorj, R., Is the association of type II diabetes with waist circumference or waist-to-hip ratio stronger than that with body mass index? *Eur J Clin Nutr* **2009**.
201. Ogonowski, J.; Miazgowski, T.; Kuczynska, M.; Krzyzanowska-Swiniarska, B.; Celewicz, Z., Pregravid body mass index as a predictor of gestational diabetes mellitus. *Diabet Med* **2009,** 26, (4), 334-8.
202. Maskarinec, G.; Grandinetti, A.; Matsuura, G.; Sharma, S.; Mau, M.; Henderson, B. E.; Kolonel, L. N., Diabetes prevalence and body mass index differ by ethnicity: the Multiethnic Cohort. *Ethn Dis* **2009,** 19, (1), 49-55.
203. DeFronzo, R. A., Lilly lecture 1987. The triumvirate: beta-cell, muscle, liver. A collusion responsible for NIDDM. *Diabetes* **1988,** 37, (6), 667-87.
204. Freidenberg, G. R.; Henry, R. R.; Klein, H. H.; Reichart, D. R.; Olefsky, J. M., Decreased kinase activity of insulin receptors from adipocytes of non-insulin-dependent diabetic subjects. *The Journal of clinical investigation* **1987,** 79, (1), 240-50.
205. Golay, A.; Felber, J. P.; Jequier, E.; DeFronzo, R. A.; Ferrannini, E., Metabolic basis of obesity and noninsulin-dependent diabetes mellitus. *Diabetes/metabolism reviews* **1988,** 4, (8), 727-47.
206. Taylor, S. I., Lilly Lecture: molecular mechanisms of insulin resistance. Lessons from patients with mutations in the insulin-receptor gene. *Diabetes* **1992,** 41, (11), 1473-90.

207. Weir, G. C.; Bonner-Weir, S., Five stages of evolving beta-cell dysfunction during progression to diabetes. *Diabetes* **2004,** 53 Suppl 3, S16-21.
208. American Diabetes Association http://www.diabetes.org/about-diabetes.jsp
209. Diabetes Prevention Program http://diabetes.niddk.nih.gov/dm/pubs/preventionprogram/
210. Diagnosis and classification of diabetes mellitus. *Diabetes care* **2007,** 30 Suppl 1, S42-7.
211. Intensive blood-glucose control with sulphonylureas or insulin compared with conventional treatment and risk of complications in patients with type 2 diabetes (UKPDS 33). UK Prospective Diabetes Study (UKPDS) Group. *Lancet* **1998,** 352, (9131), 837-53.
212. Tucholski, K.; Deja, G.; Skala-Zamorowska, E.; Jarosz-Chobot, P., Evaluation of daily glycemic profiles in well controlled children with type 1 diabetes mellitus using a continuous glucose monitoring system. *Pediatr Endocrinol Diabetes Metab* **2009,** 15, (1), 29-33.
213. Mancuso, M.; Ingegnosi, C.; Caruso-Nicoletti, M., Self monitoring blood glucose and quality of care. *Acta Biomed* **2005,** 76 Suppl 3, 56-8.
214. Palmer, J. P.; Fleming, G. A.; Greenbaum, C. J.; Herold, K. C.; Jansa, L. D.; Kolb, H.; Lachin, J. M.; Polonsky, K. S.; Pozzilli, P.; Skyler, J. S.; Steffes, M. W., C-peptide is the appropriate outcome measure for type 1 diabetes clinical trials to preserve beta-cell function: report of an ADA workshop, 21-22 October 2001. *Diabetes* **2004,** 53, (1), 250-64.
215. Souza, F.; Freeby, M.; Hultman, K.; Simpson, N.; Herron, A.; Witkowsky, P.; Liu, E.; Maffei, A.; Harris, P. E., Current progress in non-invasive imaging of beta cell mass of the endocrine pancreas. *Current medicinal chemistry* **2006,** 13, (23), 2761-73.
216. Ueberberg, S.; Meier, J. J.; Waengler, C.; Schechinger, W.; Dietrich, J. W.; Tannapfel, A.; Schmitz, I.; Schirrmacher, R.; Koller, M.; Klein, H. H.; Schneider, S., Generation of novel single-chain antibodies by phage-display technology to direct imaging agents highly selective to pancreatic beta- or alpha-cells in vivo. *Diabetes* **2009,** 58, (10), 2324-34.
217. Harris, P. E.; Ferrara, C.; Barba, P.; Polito, T.; Freeby, M.; Maffei, A., VMAT2 gene expression and function as it applies to imaging beta-cell mass. *Journal of molecular medicine (Berlin, Germany)* **2008,** 86, (1), 5-16.
218. Souza, F.; Simpson, N.; Raffo, A.; Saxena, C.; Maffei, A.; Hardy, M.; Kilbourn, M.; Goland, R.; Leibel, R.; Mann, J. J.; Van Heertum, R.; Harris, P. E., Longitudinal noninvasive PET-based beta cell mass estimates in a spontaneous diabetes rat model. *The Journal of clinical investigation* **2006,** 116, (6), 1506-13.
219. Kung, M. P.; Hou, C.; Lieberman, B. P.; Oya, S.; Ponde, D. E.; Blankemeyer, E.; Skovronsky, D.; Kilbourn, M. R.; Kung, H. F., In vivo imaging of beta-cell mass in rats using 18F-FP-(+)-DTBZ: a potential PET ligand for studying diabetes mellitus. *J Nucl Med* **2008,** 49, (7), 1171-6.
220. Kung, H. F.; Lieberman, B. P.; Zhuang, Z. P.; Oya, S.; Kung, M. P.; Choi, S. R.; Poessl, K.; Blankemeyer, E.; Hou, C.; Skovronsky, D.; Kilbourn, M., In vivo

imaging of vesicular monoamine transporter 2 in pancreas using an (18)F epoxide derivative of tetrabenazine. *Nuclear medicine and biology* **2008,** 35, (8), 825-37.
221. Kung, M. P.; Hou, C.; Goswami, R.; Ponde, D. E.; Kilbourn, M. R.; Kung, H. F., Characterization of optically resolved 9-fluoropropyl-dihydrotetrabenazine as a potential PET imaging agent targeting vesicular monoamine transporters. *Nuclear medicine and biology* **2007,** 34, (3), 239-46.
222. Ichise, M.; Harris, P. E., Imaging of beta-Cell Mass and Function. *Journal of Nuclear Medicine* **2010,** 51, (7), 1001-1004.
223. Saisho, Y.; Harris, P. E.; Butler, A. E.; Galasso, R.; Gurlo, T.; Rizza, R. A.; Butler, P. C., Relationship between pancreatic vesicular monoamine transporter 2 (VMAT2) and insulin expression in human pancreas. *J Mol Histol* **2008,** 39, (5), 543-51.
224. Goland, R.; Freeby, M.; Parsey, R.; Saisho, Y.; Kumar, D.; Simpson, N.; Hirsch, J.; Prince, M.; Maffei, A.; Mann, J. J.; Butler, P. C.; Van Heertum, R.; Leibel, R. L.; Ichise, M.; Harris, P. E., 11C-dihydrotetrabenazine PET of the pancreas in subjects with long-standing type 1 diabetes and in healthy controls. *J Nucl Med* **2009,** 50, (3), 382-9.
225. Gotthardt, M.; Lalyko, G.; van Eerd-Vismale, J.; Keil, B.; Schurrat, T.; Hower, M.; Laverman, P.; Behr, T. M.; Boerman, O. C.; Goke, B.; Behe, M., A new technique for in vivo imaging of specific GLP-1 binding sites: first results in small rodents. *Regulatory peptides* **2006,** 137, (3), 162-7.
226. Deacon, C. F., Incretin-based treatment of type 2 diabetes: glucagon-like peptide-1 receptor agonists and dipeptidyl peptidase-4 inhibitors. *Diabetes Obesity & Metabolism* **2007,** 9, 23-31.
227. Guhlke, S.; Wester, H. J.; Bruns, C.; Stocklin, G., (2-[18F]fluoropropionyl-(D)phe1)-octreotide, a potential radiopharmaceutical for quantitative somatostatin receptor imaging with PET: synthesis, radiolabeling, in vitro validation and biodistribution in mice. *Nuclear medicine and biology* **1994,** 21, (6), 819-25.
228. Wester, H. J.; Hamacher, K.; Stocklin, G., A comparative study of N.C.A. fluorine-18 labeling of proteins via acylation and photochemical conjugation. *Nuclear medicine and biology* **1996,** 23, (3), 365-72.
229. Marik, J.; Sutcliffe, J. L., Fully automated preparation of n.c.a. 4-[18F]fluorobenzoic acid and N-succinimidyl 4-[18F]fluorobenzoate using a Siemens/CTI chemistry process control unit (CPCU). *Appl Radiat Isot* **2007,** 65, (2), 199-203.
230. Vaidyanathan, G.; Zalutsky, M. R., Synthesis of N-succinimidyl 4-[18F]fluorobenzoate, an agent for labeling proteins and peptides with 18F. *Nature protocols* **2006,** 1, (4), 1655-61.
231. Wust, F.; Hultsch, C.; Bergmann, R.; Johannsen, B.; Henle, T., Radiolabelling of isopeptide N epsilon-(gamma-glutamyl)-L-lysine by conjugation with N-succinimidyl-4-[18F]fluorobenzoate. *Appl Radiat Isot* **2003,** 59, (1), 43-8.
232. Maschauer, S.; Prante, O., A series of 2-O-trifluoromethylsulfonyl-D-mannopyranosides as precursors for concomitant 18F-labeling and glycosylation by click chemistry. *Carbohydr Res* **2009,** 344, (6), 753-61.

233. Hausner, S. H.; Marik, J.; Gagnon, M. K.; Sutcliffe, J. L., In vivo positron emission tomography (PET) imaging with an alphavbeta6 specific peptide radiolabeled using 18F-"click" chemistry: evaluation and comparison with the corresponding 4-[18F]fluorobenzoyl- and 2-[18F]fluoropropionyl-peptides. *Journal of medicinal chemistry* **2008,** 51, (19), 5901-4.
234. McBride, W. J.; D'Souza, C. A.; Sharkey, R. M.; Karacay, H.; Rossi, E. A.; Chang, C. H.; Goldenberg, D. M., Improved 18F labeling of peptides with a fluoride-aluminum-chelate complex. *Bioconjugate chemistry* **2010,** 21, (7), 1331-40.
235. Brinkley, M., A brief survey of methods for preparing protein conjugates with dyes, haptens, and cross-linking reagents. *Bioconjugate chemistry* **1992,** 3, (1), 2-13.
236. Wilbur, D. S., Radiohalogenation of proteins: an overview of radionuclides, labeling methods, and reagents for conjugate labeling. *Bioconjugate chemistry* **1992,** 3, (6), 433-70.
237. Cai, W.; Zhang, X.; Wu, Y.; Chen, X., A thiol-reactive 18F-labeling agent, N-[2-(4-18F-fluorobenzamido)ethyl]maleimide, and synthesis of RGD peptide-based tracer for PET imaging of alpha v beta 3 integrin expression. *J Nucl Med* **2006,** 47, (7), 1172-80.
238. Berndt, M.; Pietzsch, J.; Wuest, F., Labeling of low-density lipoproteins using the 18F-labeled thiol-reactive reagent N-[6-(4-[18F]fluorobenzylidene)aminooxyhexyl]maleimide. *Nuclear medicine and biology* **2007,** 34, (1), 5-15.
239. de Bruin, B.; Kuhnast, B.; Hinnen, F.; Yaouancq, L.; Amessou, M.; Johannes, L.; Samson, A.; Boisgard, R.; Tavitian, B.; Dolle, F., 1-[3-(2-[18F]fluoropyridin-3-yloxy)propyl]pyrrole-2,5-dione: design, synthesis, and radiosynthesis of a new [18F]fluoropyridine-based maleimide reagent for the labeling of peptides and proteins. *Bioconjugate chemistry* **2005,** 16, (2), 406-20.
240. Toyokuni, T.; Walsh, J. C.; Dominguez, A.; Phelps, M. E.; Barrio, J. R.; Gambhir, S. S.; Satyamurthy, N., Synthesis of a new heterobifunctional linker, N-[4-(aminooxy)butyl]maleimide, for facile access to a thiol-reactive 18F-labeling agent. *Bioconjugate chemistry* **2003,** 14, (6), 1253-9.
241. Thakur, M. L., Radiolabelled peptides: now and the future. *Nuclear medicine communications* **1995,** 16, (9), 724-32.
242. Weiner, R. E.; Thakur, M. L., Radiolabeled peptides in diagnosis and therapy. *Seminars in nuclear medicine* **2001,** 31, (4), 296-311.
243. Bakker, W. H.; Krenning, E. P.; Breeman, W. A.; Koper, J. W.; Kooij, P. P.; Reubi, J. C.; Klijn, J. G.; Visser, T. J.; Docter, R.; Lamberts, S. W., Receptor scintigraphy with a radioiodinated somatostatin analogue: radiolabeling, purification, biologic activity, and in vivo application in animals. *J Nucl Med* **1990,** 31, (9), 1501-9.
244. M. Matloobi; H. Rafii; D. Beigi; A. Khalaj; Kamali-Dehghan, M., Synthesis of radioiodinated labeled peptides. *J Radioanal Nucl Chem* **2003,** 257, 71-73.

245. Gandomkar, M.; Najafi, R.; Sadat Ebrahimi, S. E.; Shafiee, A.; Babaei, M. H.; Rabbani, M.; Shabani, G. A., Direct labelling of octreotide with 99mTc: effect of different concentration of reducing agents and amount of sodium pertechnetate on radiolabelling efficiency. *Appl Radiat Isot* **2003,** 58, (3), 361-4.
246. Pervez, S.; Mushtaq, A. M.; Arif, M., Technetium-99m direct radiolabeling of lanreotide: a somatostatin analog. *Appl Radiat Isot* **2001,** 55, (5), 647-51.
247. Zamora, P. O.; Gulhke, S.; Bender, H.; Diekmann, D.; Rhodes, B. A.; Biersack, H. J.; Knapp, F. F., Jr., Experimental radiotherapy of receptor-positive human prostate adenocarcinoma with 188Re-RC-160, a directly-radiolabeled somatostatin analogue. *International journal of cancer* **1996,** 65, (2), 214-20.
248. Liu, S., Bifunctional coupling agents for radiolabeling of biomolecules and target-specific delivery of metallic radionuclides. *Adv Drug Deliv Rev* **2008,** 60, (12), 1347-70.
249. Shannon, R., Revised effective ionic radii and systematic studies of interatomic distances in halides and chalcogenides. *Acta Crystallographica Section A* **1976,** 32, (5), 751-767.
250. Delgado, R.; da Silva, J. J., Metal complexes of cyclic tetra-azatetra-acetic acids. *Talanta* **1982,** 29, (10), 815-22.
251. Meares, C. F., Chelating agents for the binding of metal ions to antibodies. *International journal of radiation applications and instrumentation* **1986,** 13, (4), 311-8.
252. Sun, X.; Anderson, C. J., Production and applications of copper-64 radiopharmaceuticals. *Methods Enzymol* **2004,** 386, 237-61.
253. Di Bartolo, N.; Sargeson, A. M.; Smith, S. V., New 64Cu PET imaging agents for personalised medicine and drug development using the hexa-aza cage, SarAr. *Organic & biomolecular chemistry* **2006,** 4, (17), 3350-7.
254. Liu, S.; Edwards, D. S., 99mTc-Labeled Small Peptides as Diagnostic Radiopharmaceuticals. *Chemical reviews* **1999,** 99, (9), 2235-68.
255. Wadas, T. J.; Wong, E. H.; Weisman, G. R.; Anderson, C. J., Coordinating radiometals of copper, gallium, indium, yttrium, and zirconium for PET and SPECT imaging of disease. *Chemical reviews* **2010,** 110, (5), 2858-902.
256. von Guggenberg, E.; Dietrich, H.; Skvortsova, I.; Gabriel, M.; Virgolini, I. J.; Decristoforo, C., 99mTc-labelled HYNIC-minigastrin with reduced kidney uptake for targeting of CCK-2 receptor-positive tumours. *European journal of nuclear medicine and molecular imaging* **2007,** 34, (8), 1209-18.
257. Harris, A. G., Somatostatin and somatostatin analogues: pharmacokinetics and pharmacodynamic effects. *Gut* **1994,** 35, (3 Suppl), S1-4.
258. Haubner, R.; Kuhnast, B.; Mang, C.; Weber, W. A.; Kessler, H.; Wester, H. J.; Schwaiger, M., [18F]Galacto-RGD: synthesis, radiolabeling, metabolic stability, and radiation dose estimates. *Bioconjugate chemistry* **2004,** 15, (1), 61-9.
259. Nicholson, S. A.; Beasley, M. B.; Brambilla, E.; Hasleton, P. S.; Colby, T. V.; Sheppard, M. N.; Falk, R.; Travis, W. D., Small cell lung carcinoma (SCLC): a clinicopathologic study of 100 cases with surgical specimens. *Am J Surg Pathol* **2002,** 26, (9), 1184-97.

260. Sorensen, J. B.; Hirsch, F. R.; Gazdar, A.; Olsen, J. E., Interobserver variability in histopathologic subtyping and grading of pulmonary adenocarcinoma. *Cancer* **1993,** 71, (10), 2971-6.
261. Duffy, M. J., Biochemical markers in breast cancer: which ones are clinically useful? *Clin Biochem* **2001,** 34, (5), 347-52.
262. Skirnisdottir, I.; Sorbe, B.; Seidal, T., The growth factor receptors HER-2/neu and EGFR, their relationship, and their effects on the prognosis in early stage (FIGO I-II) epithelial ovarian carcinoma. *Int J Gynecol Cancer* **2001,** 11, (2), 119-29.
263. Hynes, R. O., Integrins: bidirectional, allosteric signaling machines. *Cell* **2002,** 110, (6), 673-87.
264. Wagner, D. D.; Ivatt, R.; Destree, A. T.; Hynes, R. O., Similarities and differences between the fibronectins of normal and transformed hamster cells. *J Biol Chem* **1981,** 256, (22), 11708-15.
265. Plantefaber, L. C.; Hynes, R. O., Changes in integrin receptors on oncogenically transformed cells. *Cell* **1989,** 56, (2), 281-90.
266. Ria, R.; Reale, A.; Castrovilli, A.; Mangialardi, G.; Dammacco, F.; Ribatti, D.; Vacca, A., Angiogenesis and progression in human melanoma. *Dermatol Res Pract* **2010,** 2010, 185687.
267. Zutter, M. M.; Santoro, S. A.; Staatz, W. D.; Tsung, Y. L., Re-expression of the alpha 2 beta 1 integrin abrogates the malignant phenotype of breast carcinoma cells. *Proceedings of the National Academy of Sciences of the United States of America* **1995,** 92, (16), 7411-5.
268. Albelda, S. M.; Mette, S. A.; Elder, D. E.; Stewart, R.; Damjanovich, L.; Herlyn, M.; Buck, C. A., Integrin distribution in malignant melanoma: association of the beta 3 subunit with tumor progression. *Cancer research* **1990,** 50, (20), 6757-64.
269. Danen, E. H.; Jansen, K. F.; Van Kraats, A. A.; Cornelissen, I. M.; Ruiter, D. J.; Van Muijen, G. N., Alpha v-integrins in human melanoma: gain of alpha v beta 3 and loss of alpha v beta 5 are related to tumor progression in situ but not to metastatic capacity of cell lines in nude mice. *International journal of cancer* **1995,** 61, (4), 491-6.
270. Teti, A.; Migliaccio, S.; Baron, R., The role of the alphaVbeta3 integrin in the development of osteolytic bone metastases: a pharmacological target for alternative therapy? *Calcif Tissue Int* **2002,** 71, (4), 293-9.
271. Varner, J. A.; Cheresh, D. A., Integrins and cancer. *Current opinion in cell biology* **1996,** 8, (5), 724-30.
272. Byzova, T. V.; Goldman, C. K.; Pampori, N.; Thomas, K. A.; Bett, A.; Shattil, S. J.; Plow, E. F., A mechanism for modulation of cellular responses to VEGF: activation of the integrins. *Mol Cell* **2000,** 6, (4), 851-60.
273. Nikolopoulos, S. N.; Blaikie, P.; Yoshioka, T.; Guo, W.; Giancotti, F. G., Integrin beta4 signaling promotes tumor angiogenesis. *Cancer Cell* **2004,** 6, (5), 471-83.
274. Senger, D. R.; Claffey, K. P.; Benes, J. E.; Perruzzi, C. A.; Sergiou, A. P.; Detmar, M., Angiogenesis promoted by vascular endothelial growth factor: regulation through alpha1beta1 and alpha2beta1 integrins. *Proceedings of the National Academy of Sciences of the United States of America* **1997,** 94, (25), 13612-7.

275. Francis, S. E.; Goh, K. L.; Hodivala-Dilke, K.; Bader, B. L.; Stark, M.; Davidson, D.; Hynes, R. O., Central roles of alpha5beta1 integrin and fibronectin in vascular development in mouse embryos and embryoid bodies. *Arterioscler Thromb Vasc Biol* **2002,** 22, (6), 927-33.
276. Arihiro, K.; Kaneko, M.; Fujii, S.; Inai, K.; Yokosaki, Y., Significance of $alpha_9$ $beta_1$ and $alpha_v$ $beta_6$ integrin expression in breast carcinoma. *Breast Cancer* **2000,** 7, 19-26.
277. Jones, J.; Watt, F. M.; Speight, P. M., Changes in expression of $alpha_v$ integrins in oral squamous cell carcinomas. *J. Oral Pathol. Med.* **1997,** 26, 63-68.
278. Haapasalmi, K.; Zhang, K.; Tonnesen, M.; Olerud, J.; Sheppard, D.; Salo, T.; Kramer, R.; Clark, R. A.; Uitto, V. J.; Larjava, H., Keratinocytes in human wounds express alpha v beta 6 integrin. *J Invest Dermatol* **1996,** 106, (1), 42-8.
279. Agrez, M.; Chen, A.; Cone, R. I.; Pytela, R.; Sheppard, D., The alpha v beta 6 integrin promotes proliferation of colon carcinoma cells through a unique region of the beta 6 cytoplasmic domain. *J Cell Biol* **1994,** 127, (2), 547-56.
280. Hamidi, S.; Salo, T.; Kainulainen, T.; Epstein, J.; Lerner, K.; Larjava, H., Expression of alpha(v)beta6 integrin in oral leukoplakia. *Br J Cancer* **2000,** 82, (8), 1433-40.
281. Sidhu, S. S., Engineering M13 for phage display. *Biomol Eng* **2001,** 18, (2), 57-63.
282. Sosabowski, J. K.; Mather, S. J., Conjugation of DOTA-like chelating agents to peptides and radiolabeling with trivalent metallic isotopes. *Nature protocols* **2006,** 1, (2), 972-6.
283. Oyama, T.; Rombel, I. T.; Samli, K. N.; Zhou, X.; Brown, K. C., Isolation of multiple cell-binding ligands from different phage displayed-peptide libraries. *Biosensors Bioelect.* **2006,** 21, 1867-1875.
284. Tomayko, M. M.; Reynolds, C. P., Determination of subcutaneous tumor size in athymic (nude) mice. *Cancer chemotherapy and pharmacology* **1989,** 24, (3), 148-54.
285. Bernard, B. F.; Krenning, E. P.; Breeman, W. A.; Rolleman, E. J.; Bakker, W. H.; Visser, T. J.; Macke, H.; de Jong, M., D-lysine reduction of indium-111 octreotide and yttrium-90 octreotide renal uptake. *J Nucl Med* **1997,** 38, (12), 1929-33.
286. de Jong, M.; Rolleman, E. J.; Bernard, B. F.; Visser, T. J.; Bakker, W. H.; Breeman, W. A.; Krenning, E. P., Inhibition of renal uptake of indium-111-DTPA-octreotide in vivo. *J Nucl Med* **1996,** 37, (8), 1388-92.
287. Kim, I. S.; Yoo, T. M.; Kobayashi, H.; Kim, M. K.; Le, N.; Wang, Q. C.; Pastan, I.; Carrasquillo, J. A.; Paik, C. H., Chemical modification to reduce renal uptake of disulfide-bonded variable region fragment of anti-Tac monoclonal antibody labeled with 99mTc. *Bioconjugate chemistry* **1999,** 10, (3), 447-53.
288. Kobayashi, H.; Le, N.; Kim, I. S.; Kim, M. K.; Pie, J. E.; Drumm, D.; Paik, D. S.; Waldmann, T. A.; Paik, C. H.; Carrasquillo, J. A., The pharmacokinetic characteristics of glycolated humanized anti-Tac Fabs are determined by their isoelectric points. *Cancer research* **1999,** 59, (2), 422-30.
289. Kobayashi, H.; Kim, I. S.; Drumm, D.; Kim, M. K.; Paik, D. S.; Le, N.; Waldmann, T. A.; Carrasquillo, J. A.; Paik, C. H., Favorable effects of glycolate

conjugation on the biodistribution of humanized antiTac Fab fragment. *J Nucl Med* **1999,** 40, (5), 837-45.
290. Nestor, J. J., Jr., The medicinal chemistry of peptides. *Current medicinal chemistry* **2009,** 16, (33), 4399-418.
291. Ginsberg, M. H.; Partridge, A.; Shattil, S. J., Integrin regulation. *Current opinion in cell biology* **2005,** 17, (5), 509-16.
292. Delgado, C.; Francis, G. E.; Fisher, D., The uses and properties of PEG-linked proteins. *Crit Rev Ther Drug Carrier Syst* **1992,** 9, (3-4), 249-304.
293. Francis, G. E.; Delgado, C.; Fisher, D.; Malik, F.; Agrawal, A. K., Polyethylene glycol modification: relevance of improved methodology to tumour targeting. *J Drug Target* **1996,** 3, (5), 321-40.
294. Tsutsumi, Y.; Onda, M.; Nagata, S.; Lee, B.; Kreitman, R. J.; Pastan, I., Site-specific chemical modification with polyethylene glycol of recombinant immunotoxin anti-Tac(Fv)-PE38 (LMB-2) improves antitumor activity and reduces animal toxicity and immunogenicity. *Proceedings of the National Academy of Sciences of the United States of America* **2000,** 97, (15), 8548-53.
295. Molineux, G., Pegylation: engineering improved pharmaceuticals for enhanced therapy. *Cancer treatment reviews* **2002,** 28 Suppl A, 13-6.
296. Silbernagl, S., The renal handling of amino acids and oligopeptides. *Physiological reviews* **1988,** 68, (3), 911-1007.
297. Christensen, E. I.; Gburek, J., Protein reabsorption in renal proximal tubule-function and dysfunction in kidney pathophysiology. *Pediatric nephrology (Berlin, Germany)* **2004,** 19, (7), 714-21.
298. Vegt, E.; Eek, A.; Oyen, W. J.; de Jong, M.; Gotthardt, M.; Boerman, O. C., Albumin-derived peptides efficiently reduce renal uptake of radiolabelled peptides. *European journal of nuclear medicine and molecular imaging* **2009**.
299. Vegt, E.; van Eerd, J. E.; Eek, A.; Oyen, W. J.; Wetzels, J. F.; de Jong, M.; Russel, F. G.; Masereeuw, R.; Gotthardt, M.; Boerman, O. C., Reducing renal uptake of radiolabeled peptides using albumin fragments. *J Nucl Med* **2008,** 49, (9), 1506-11.
300. Saudek, F.; Brogren, C. H.; Manohar, S., Imaging the Beta-cell mass: why and how. *Rev Diabet Stud* **2008,** 5, (1), 6-12.
301. Moore, A.; Bonner-Weir, S.; Weissleder, R., Noninvasive in vivo measurement of beta-cell mass in mouse model of diabetes. *Diabetes* **2001,** 50, (10), 2231-6.
302. Hampe, C. S.; Wallen, A. R.; Schlosser, M.; Ziegler, M.; Sweet, I. R., Quantitative evaluation of a monoclonal antibody and its fragment as potential markers for pancreatic beta cell mass. *Exp Clin Endocrinol Diabetes* **2005,** 113, (7), 381-7.
303. Halle, J. P.; Bourassa, S.; Leblond, F. A.; Chevalier, S.; Beaudry, M.; Chapdelaine, A.; Cousineau, S.; Saintonge, J.; Yale, J. F., Protection of islets of Langerhans from antibodies by microencapsulation with alginate-poly-L-lysine membranes. *Transplantation* **1993,** 55, (2), 350-4.
304. Alejandro, R.; Shienvold, F. L.; Hajek, S. A.; Pierce, M.; Paul, R.; Mintz, D. H., A ganglioside antigen on the rat pancreatic B cell surface identified by

monoclonal antibody R2D6. *The Journal of clinical investigation* **1984,** 74, (1), 25-38.
305. Muramatsu, T.; Arakawa, S.; Fukazawa, K.; Fujiwara, Y.; Yoshida, T.; Sasaki, R.; Masuda, S.; Park, H. M., In vivo gene electroporation in skeletal muscle with special reference to the duration of gene expression. *International journal of molecular medicine* **2001,** 7, (1), 37-42.
306. Malaisse, W. J., On the track to the beta-cell. *Diabetologia* **2001,** 44, (4), 393-406.
307. Malaisse, W. J.; Doherty, M.; Kadiata, M. M.; Ladriere, L.; Malaisse-Lagae, F., Pancreatic fate of D-[3H] mannoheptulose. *Cell Biochem Funct* **2001,** 19, (3), 171-9.
308. Malaisse, W. J.; Doherty, M.; Ladriere, L.; Malaisse-Lagae, F., Pancreatic uptake of [2-(14)C]alloxan. *International journal of molecular medicine* **2001,** 7, (3), 311-5.
309. Malaisse, W. J.; Ladriere, L., Assessment of B-cell mass in isolated islets exposed to D-[3H]mannoheptulose. *International journal of molecular medicine* **2001,** 7, (4), 405-6.
310. Ramirez, R.; Rasschaert, J.; Laghmich, A.; Louchami, K.; Nadi, A. B.; Jijakli, H.; Kadiata, M. M.; Sener, A.; Malaisse, W. J., Uptake of D-mannoheptulose by normal and tumoral pancreatic islet cells. *International journal of molecular medicine* **2001,** 7, (6), 631-8.
311. Rasschaert, J.; Kadiata, M. M.; Malaisse, W. J., Effects of D-mannoheptulose upon D-glucose metabolism in tumoral pancreatic islet cells. *Mol Cell Biochem* **2001,** 226, (1-2), 77-81.
312. Ramirez, R.; Jijakli, H.; Zhang, H. X.; Nadi, A. B.; Sener, A.; Malaisse, W. J., Effects of D-mannoheptulose upon D-glucose metabolism in pancreatic B and non-B islet cells. *International journal of molecular medicine* **2002,** 9, (2), 159-63.
313. Sener, A.; Ladriere, L.; Benito, C.; Gomis, R.; Malaisse-Lagae, F.; Malaisse, W. J., D-mannoheptulose uptake and its metabolic and secretory effects in human pancreatic islets. *International journal of molecular medicine* **2000,** 6, (6), 617-20.
314. Schneider, S.; Feilen, P. J.; Schreckenberger, M.; Schwanstecher, M.; Schwanstecher, C.; Buchholz, H. G.; Thews, O.; Oberholzer, K.; Korobeynikov, A.; Bauman, A.; Comagic, S.; Piel, M.; Schirrmacher, E.; Shiue, C. Y.; Alavi, A. A.; Bartenstein, P.; Rosch, F.; Weber, M. M.; Klein, H. H.; Schirrmacher, R., In vitro and in vivo evaluation of novel glibenclamide derivatives as imaging agents for the non-invasive assessment of the pancreatic islet cell mass in animals and humans. *Exp Clin Endocrinol Diabetes* **2005,** 113, (7), 388-95.
315. Kostic, B. A.; Olsen, K. M.; Kearns, G. L.; Kemp, S. F., Effect of glycated albumin on phenytoin binding in elderly patients with type II diabetes mellitus. *Pharmacotherapy* **1990,** 10, (5), 362-5.
316. Olsen, K. M.; Kearns, G. L.; Kemp, S. F., Glyburide protein binding and the effect of albumin glycation in children, young adults, and older adults with diabetes. *J Clin Pharmacol* **1995,** 35, (7), 739-45.
317. Wangler, B.; Beck, C.; Shiue, C. Y.; Schneider, S.; Schwanstecher, C.; Schwanstecher, M.; Feilen, P. J.; Alavi, A.; Rosch, F.; Schirrmacher, R.,

Synthesis and in vitro evaluation of (S)-2-([11C]methoxy)-4-[3-methyl-1-(2-piperidine-1-yl-phenyl)-butyl-carbam oyl]-benzoic acid ([11C]methoxy-repaglinide): a potential beta-cell imaging agent. *Bioorganic & medicinal chemistry letters* **2004,** 14, (20), 5205-9.

318. Wangler, B.; Schneider, S.; Thews, O.; Schirrmacher, E.; Comagic, S.; Feilen, P.; Schwanstecher, C.; Schwanstecher, M.; Shiue, C. Y.; Alavi, A.; Hohnemann, S.; Piel, M.; Rosch, F.; Schirrmacher, R., Synthesis and evaluation of (S)-2-(2-[18F]fluoroethoxy)-4-([3-methyl-1-(2-piperidin-1-yl-phenyl)-butyl -carbamoyl]-methyl)-benzoic acid ([18F]repaglinide): a promising radioligand for quantification of pancreatic beta-cell mass with positron emission tomography (PET). *Nuclear medicine and biology* **2004,** 31, (5), 639-47.
319. Bernal-Mizrachi, E.; Cras-Meneur, C.; Ohsugi, M.; Permutt, M. A., Gene expression profiling in islet biology and diabetes research. *Diabetes/metabolism research and reviews* **2003,** 19, (1), 32-42.
320. Abderrahmani, A.; Niederhauser, G.; Plaisance, V.; Haefliger, J. A.; Regazzi, R.; Waeber, G., Neuronal traits are required for glucose-induced insulin secretion. *FEBS letters* **2004,** 565, (1-3), 133-8.
321. Clark, P. B.; Gage, H. D.; Brown-Proctor, C.; Buchheimer, N.; Calles-Escandon, J.; Mach, R. H.; Morton, K. A., Neurofunctional imaging of the pancreas utilizing the cholinergic PET radioligand [18F]4-fluorobenzyltrozamicol. *European journal of nuclear medicine and molecular imaging* **2004,** 31, (2), 258-60.
322. Urner, F.; Herrmann, W. L.; Baulieu, E. E.; Schorderet-Slatkine, S., Inhibition of denuded mouse oocyte meiotic maturation by forskolin, an activator of adenylate cyclase. *Endocrinology* **1983,** 113, (3), 1170-2.
323. Lindstrom, P., Aromatic-L-amino-acid decarboxylase activity in mouse pancreatic islets. *Biochim Biophys Acta* **1986,** 884, (2), 276-81.
324. Borelli, M. I.; Villar, M. J.; Orezzoli, A.; Gagliardino, J. J., Presence of DOPA decarboxylase and its localisation in adult rat pancreatic islet cells. *Diabetes Metab* **1997,** 23, (2), 161-3.
325. Anlauf, M.; Eissele, R.; Schafer, M. K.; Eiden, L. E.; Arnold, R.; Pauser, U.; Kloppel, G.; Weihe, E., Expression of the two isoforms of the vesicular monoamine transporter (VMAT1 and VMAT2) in the endocrine pancreas and pancreatic endocrine tumors. *J Histochem Cytochem* **2003,** 51, (8), 1027-40.
326. Lin, M.; Lubag, A.; McGuire, M. J.; Seliounine, S. Y.; Tsyganov, E. N.; Antich, P. P.; Sherry, A. D.; Brown, K. C.; Sun, X., Advances in molecular imaging of pancreatic beta cells. *Front Biosci* **2008,** 13, 4558-75.
327. Weir, G. C.; Mojsov, S.; Hendrick, G. K.; Habener, J. F., Glucagonlike peptide I (7-37) actions on endocrine pancreas. *Diabetes* **1989,** 38, (3), 338-42.
328. Thorens, B., Expression cloning of the pancreatic beta cell receptor for the gluco-incretin hormone glucagon-like peptide 1. *Proceedings of the National Academy of Sciences of the United States of America* **1992,** 89, (18), 8641-5.
329. Heller, R. S.; Kieffer, T. J.; Habener, J. F., Insulinotropic glucagon-like peptide I receptor expression in glucagon-producing alpha-cells of the rat endocrine pancreas. *Diabetes* **1997,** 46, (5), 785-91.

330. Bullock, B. P.; Heller, R. S.; Habener, J. F., Tissue distribution of messenger ribonucleic acid encoding the rat glucagon-like peptide-1 receptor. *Endocrinology* **1996,** 137, (7), 2968-78.
331. Widmann, C.; Dolci, W.; Thorens, B., Heterologous desensitization of the glucagon-like peptide-1 receptor by phorbol esters requires phosphorylation of the cytoplasmic tail at four different sites. *J Biol Chem* **1996,** 271, (33), 19957-63.
332. Widmann, C.; Dolci, W.; Thorens, B., Internalization and homologous desensitization of the GLP-1 receptor depend on phosphorylation of the receptor carboxyl tail at the same three sites. *Mol Endocrinol* **1997,** 11, (8), 1094-102.
333. Eng, J.; Kleinman, W. A.; Singh, L.; Singh, G.; Raufman, J. P., Isolation and characterization of exendin-4, an exendin-3 analogue, from Heloderma suspectum venom. Further evidence for an exendin receptor on dispersed acini from guinea pig pancreas. *J Biol Chem* **1992,** 267, (11), 7402-5.
334. Wicki, A.; Wild, D.; Storch, D.; Seemayer, C.; Gotthardt, M.; Behe, M.; Kneifel, S.; Mihatsch, M. J.; Reubi, J. C.; Macke, H. R.; Christofori, G., [Lys40(Ahx-DTPA-111In)NH2]-Exendin-4 is a highly efficient radiotherapeutic for glucagon-like peptide-1 receptor-targeted therapy for insulinoma. *Clin Cancer Res* **2007,** 13, (12), 3696-705.
335. Christ, E.; Wild, D.; Forrer, F.; Brandle, M.; Sahli, R.; Clerici, T.; Gloor, B.; Martius, F.; Maecke, H.; Reubi, J. C., Glucagon-like peptide-1 receptor imaging for localization of insulinomas. *The Journal of clinical endocrinology and metabolism* **2009,** 94, (11), 4398-405.
336. Deacon, C. F., Circulation and degradation of GIP and GLP-1. *Horm Metab Res* **2004,** 36, (11-12), 761-5.
337. Barnett, A., DPP-4 inhibitors and their potential role in the management of type 2 diabetes. *Int J Clin Pract* **2006,** 60, (11), 1454-70.
338. Beinborn, M.; Worrall, C. I.; McBride, E. W.; Kopin, A. S., A human glucagon-like peptide-1 receptor polymorphism results in reduced agonist responsiveness. *Regulatory peptides* **2005,** 130, (1-2), 1-6.
339. Hupe-Sodmann, K.; Goke, R.; Goke, B.; Thole, H. H.; Zimmermann, B.; Voigt, K.; McGregor, G. P., Endoproteolysis of glucagon-like peptide (GLP)-1 (7-36) amide by ectopeptidases in RINm5F cells. *Peptides* **1997,** 18, (5), 625-32.
340. Murage, E. N.; Schroeder, J. C.; Beinborn, M.; Ahn, J. M., Search for alpha-helical propensity in the receptor-bound conformation of glucagon-like peptide-1. *Bioorganic & medicinal chemistry* **2008,** 16, (23), 10106-12.
341. Thornton, K.; Gorenstein, D. G., Structure of glucagon-like peptide (7-36) amide in a dodecylphosphocholine micelle as determined by 2D NMR. *Biochemistry* **1994,** 33, (12), 3532-9.
342. Ahn, J. M.; Gitu, P. M.; Medeiros, M.; Swift, J. R.; Trivedi, D.; Hruby, V. J., A new approach to search for the bioactive conformation of glucagon: positional cyclization scanning. *Journal of medicinal chemistry* **2001,** 44, (19), 3109-16.
343. Rink, H., Solid-phase synthesis of protected peptide fragments using a trialkoxy-diphenyl-methylester resin. *Tetrahedron Letters* **1987,** 28, (33), 3787-3790.

344. Kaiser, E.; Colescott, R. L.; Bossinger, C. D.; Cook, P. I., Color test for detection of free terminal amino groups in the solid-phase synthesis of peptides. *Anal Biochem* **1970,** 34, (2), 595-8.
345. Hancock, W. S.; Battersby, J. E., A new micro-test for the detection of incomplete coupling reactions in solid-phase peptide synthesis using 2,4,6-trinitrobenzenesulphonic acid. *Anal Biochem* **1976,** 71, (1), 260-4.
346. Mentlein, R.; Dahms, P.; Grandt, D.; Kruger, R., Proteolytic processing of neuropeptide Y and peptide YY by dipeptidyl peptidase IV. *Regulatory peptides* **1993,** 49, (2), 133-44.
347. Ueda, T.; Tomita, K.; Notsu, Y.; Ito, T.; Fumoto, M.; Takakura, T.; Nagatome, H.; Takimoto, A.; Mihara, S.; Togame, H.; Kawamoto, K.; Iwasaki, T.; Asakura, K.; Oshima, T.; Hanasaki, K.; Nishimura, S.; Kondo, H., Chemoenzymatic synthesis of glycosylated glucagon-like peptide 1: effect of glycosylation on proteolytic resistance and in vivo blood glucose-lowering activity. *J Am Chem Soc* **2009,** 131, (17), 6237-45.
348. Tesch, G. H.; Allen, T. J., Rodent models of streptozotocin-induced diabetic nephropathy. *Nephrology (Carlton, Vic* **2007,** 12, (3), 261-6.
349. Iwak, T.; Hayakawa, T., *A Color Atlas of Sectional Anatomy of the Mouse*. 2001.
350. Sarrauste de Menthiere, C.; Chavanieu, A.; Grassy, G.; Dalle, S.; Salazar, G.; Kervran, A.; Pfeiffer, B.; Renard, P.; Delagrange, P.; Manechez, D.; Bakes, D.; Ktorza, A.; Calas, B., Structural requirements of the N-terminal region of GLP-1-[7-37]-NH2 for receptor interaction and cAMP production. *Eur J Med Chem* **2004,** 39, (6), 473-80.
351. Medarova, Z.; Moore, A., Imaging of pancreatic cancer: a promise for early diagnosis through targeted strategies. *Cancer Ther* **2004,** 2, 329-344.
352. Ito, M.; Kondo, Y.; Nakatani, A.; Hayashi, K.; Naruse, A., Characterization of low dose streptozotocin-induced progressive diabetes in mice. *Environmental toxicology and pharmacology* **2001,** 9, (3), 71-78.
353. Ito, M.; Kondo, Y.; Nakatani, A.; Naruse, A., New model of progressive non-insulin-dependent diabetes mellitus in mice induced by streptozotocin. *Biological & pharmaceutical bulletin* **1999,** 22, (9), 988-9.
354. Wilson, G. L.; Leiter, E. H., Streptozotocin interactions with pancreatic beta cells and the induction of insulin-dependent diabetes. *Current topics in microbiology and immunology* **1990,** 156, 27-54.
355. McEvoy, R. C.; Andersson, J.; Sandler, S.; Hellerstrom, C., Multiple low-dose streptozotocin-induced diabetes in the mouse. Evidence for stimulation of a cytotoxic cellular immune response against an insulin-producing beta cell line. *The Journal of clinical investigation* **1984,** 74, (3), 715-22.
356. Le Marchand-Brustel, Y.; Freychet, P., Effect of fasting and streptozotocin diabetes on insulin binding and action in the isolated mouse soleus muscle. *The Journal of clinical investigation* **1979,** 64, (5), 1505-15.
357. Brosky, G.; Logothetopoulos, J., Streptozotocin diabetes in the mouse and guinea pig. *Diabetes* **1969,** 18, (9), 606-11.

358. Malaisse, W. J.; Damhaut, P.; Ladriere, L.; Goldman, S., Fate of 2-deoxy-2-[18F]fluoro-D-glucose in hyperglycemic rats. *International journal of molecular medicine* **2000,** 6, (5), 549-52.
359. Hupe-Sodmann, K.; McGregor, G. P.; Bridenbaugh, R.; Goke, R.; Goke, B.; Thole, H.; Zimmermann, B.; Voigt, K., Characterisation of the processing by human neutral endopeptidase 24.11 of GLP-1(7-36) amide and comparison of the substrate specificity of the enzyme for other glucagon-like peptides. *Regulatory peptides* **1995,** 58, (3), 149-56.
360. Hostetler, E. D.; Edwards, W. B.; Anderson, C. J.; Welch, M. J., Synthesis of 4-[18F]fluorobenzoyl octreotide and biodistribution in tumor-bearing lewis rats. *J. Labelled Cpd. Radiopharm.* **1999,** 42, (Supp 1), S720-721.
361. Li, W. P.; Meyer, L. A.; Anderson, C. J., Radiopharmaceuticals for Positron Emission Tomography Imaging of Somatostatin Receptor Positive Tumors. *Top Curr Chem* **2005,** 250, 179-192.
362. Haubner, R.; Wester, H. J., Radiolabeled tracers for imaging of tumor angiogenesis and evaluation of anti-angiogenic therapies. *Curr Pharm Des* **2004,** 10, (13), 1439-55.
363. Liu, W.; Hao, G.; Long, M. A.; Anthony, T.; Hsieh, J. T.; Sun, X., Imparting multivalency to a bifunctional chelator: a scaffold design for targeted PET imaging probes. *Angew Chem Int Ed Engl* **2009,** 48, (40), 7346-9.
364. Almutairi, A.; Rossin, R.; Shokeen, M.; Hagooly, A.; Ananth, A.; Capoccia, B.; Guillaudeu, S.; Abendschein, D.; Anderson, C. J.; Welch, M. J.; Frechet, J. M., Biodegradable dendritic positron-emitting nanoprobes for the noninvasive imaging of angiogenesis. *Proceedings of the National Academy of Sciences of the United States of America* **2009,** 106, (3), 685-90.
365. Knauf, M. J.; Bell, D. P.; Hirtzer, P.; Luo, Z. P.; Young, J. D.; Katre, N. V., Relationship of effective molecular size to systemic clearance in rats of recombinant interleukin-2 chemically modified with water-soluble polymers. *J Biol Chem* **1988,** 263, (29), 15064-70.
366. Koumenis, I. L.; Shahrokh, Z.; Leong, S.; Hsei, V.; Deforge, L.; Zapata, G., Modulating pharmacokinetics of an anti-interleukin-8 F(ab')(2) by amine-specific PEGylation with preserved bioactivity. *Int J Pharm* **2000,** 198, (1), 83-95.
367. Hamano, Y.; Grunkemeyer, J. A.; Sudhakar, A.; Zeisberg, M.; Cosgrove, D.; Morello, R.; Lee, B.; Sugimoto, H.; Kalluri, R., Determinants of vascular permeability in the kidney glomerulus. *J Biol Chem* **2002,** 277, (34), 31154-62.
368. Caulfield, J. P.; Farquhar, M. G., The permeability of glomerular capillaries to graded dextrans. Identification of the basement membrane as the primary filtration barrier. *J Cell Biol* **1974,** 63, (3), 883-903.
369. DeNardo, S. J.; Yao, Z.; Lam, K. S.; Song, A.; Burke, P. A.; Mirick, G. R.; Lamborn, K. R.; O'Donnell, R. T.; DeNardo, G. L., Effect of molecular size of pegylated peptide on the pharmacokinetics and tumor targeting in lymphoma-bearing mice. *Clin Cancer Res* **2003,** 9, (10 Pt 2), 3854S-64S.
370. Christensen, E. I.; Birn, H.; Verroust, P.; Moestrup, S. K., Megalin-mediated endocytosis in renal proximal tubule. *Ren Fail* **1998,** 20, (2), 191-9.

371. Mogensen, C. E.; Solling, Studies on renal tubular protein reabsorption: partial and near complete inhibition by certain amino acids. *Scand J Clin Lab Invest* **1977,** 37, (6), 477-86.
372. de Jong, M.; Barone, R.; Krenning, E.; Bernard, B.; Melis, M.; Visser, T.; Gekle, M.; Willnow, T. E.; Walrand, S.; Jamar, F.; Pauwels, S., Megalin is essential for renal proximal tubule reabsorption of (111)In-DTPA-octreotide. *J Nucl Med* **2005,** 46, (10), 1696-700.
373. Behr, T. M.; Goldenberg, D. M.; Becker, W., Reducing the renal uptake of radiolabeled antibody fragments and peptides for diagnosis and therapy: present status, future prospects and limitations. *European journal of nuclear medicine* **1998,** 25, (2), 201-12.
374. Akizawa, H.; Uehara, T.; Arano, Y., Renal uptake and metabolism of radiopharmaceuticals derived from peptides and proteins. *Adv Drug Deliv Rev* **2008,** 60, (12), 1319-28.
375. Kragl, M.; Lammert, E., Basement membrane in pancreatic islet function. *Adv Exp Med Biol* **2010,** 654, 217-34.
376. Reubi, J. C.; Waser, B., Concomitant expression of several peptide receptors in neuroendocrine tumours: molecular basis for in vivo multireceptor tumour targeting. *European journal of nuclear medicine and molecular imaging* **2003,** 30, (5), 781-93.
377. Wester, H. J.; Brockmann, J.; Rosch, F.; Wutz, W.; Herzog, H.; Smith-Jones, P.; Stolz, B.; Bruns, C.; Stocklin, G., PET-pharmacokinetics of 18F-octreotide: a comparison with 67Ga-DFO- and 86Y-DTPA-octreotide. *Nuclear medicine and biology* **1997,** 24, (4), 275-86.